BIODEGRADABLE, LIQUID-FILLED, SPHERICAL CAPSULES WITH PRE-DETERMINED BURST TIMES

A THESIS

SUBMITTED TO THE FACULTY OF THE GRADUATE SCHOOL

OF THE UNIVERSITY OF MINNESOTA

BY

KRUTIKA HARISH JAIN

IN PARTIAL FULFILLMENT OF THE REQUIREMENTS

FOR THE DEGREE OF

MASTER OF SCIENCE

Prof. RONALD A. SIEGEL

JUNE 2017

Acknowledgments

I would first like to thank Professor Ronald A. Siegel for patiently and tirelessly guiding me in all my endeavors and for providing me with personal and financial support. Dr Siegel has always imparted the idea of holistic learning, and that has made my graduate school experience most gratifying.

I would like to express my gratitude to Dr David Wood for serving on my thesis committee and for some of the most useful discussions about my work. I would also like to thank his students, Alexander Peterson and Xinran Lu, for helping with some of my initial work.

I would like to thank Hassaan Khan for volunteering to build the rotor system for our lab. I could leap forward with my work only after a procedure based on this system was developed.

I deeply appreciate Dr Raj Suryanarayanan for whole-heartedly allowing me to conduct several experiments in his lab (and for being way more concerned about my suspended work than his broken instrument). I thank Dr Wei Shen for completely trusting me with her lab for months together, which contributed a significant chunk to my research.

A special thanks to Dr Timothy Wiedmann for accepting to serve on my committee and Dr Calvin Sun for the very many useful discussions about my project. I would like to extend my gratitude to Dr Weislaw Suszynski, Dr Sandy Johnson and Bin Xuu for training me on various protocols and going beyond to help me with my work. I would like to make a special mention of the Medical Devices Center for generously providing a very good infrastructure to conduct various aspects of my work.

I would like to thank Shunjia Zhang who I worked with when this project was still in its infancy stage. Thanks to the very dynamic Siegel Lab group, especially Allison Siehr, Davin Rautiola, Dr Anasuya Sahoo and Nathan Richman for their very useful comments and insights in the final run-up to the project. A special thanks to Kweku for the many discussions.

I would like to thank Sivaramakrishnan S.R. for his valuable programming work to analyze my data and also for being an unwavering source of support and motivation.

Finally, I would like to thank my family for being my pillar of support and strength from 9000 miles away.

Dedication

To Mom, Dad, Dadaji and Dadiji

Abstract

A biodegradable poly(lactic acid-co-glycolic acid) (PLGA) capsule is presented in a spherical geometry, which exploits the principle of osmosis as an internal program to achieve a delayed-burst release of its load. The capsule burst lag-time is accurately predicted by modeling the rate of water uptake by the capsule core as a function of the capsule shell thickness, radius of the capsule, core osmotic pressure and the membrane tensile strength. Elastoplastic and failure characterization of PLGA was conducted as a function of hydration under uniaxial and biaxial stretch and by a novel “beach ball” inflation technique. The presence of small amounts of moisture leads to a decrease in yield stress and a decrease in elongation at break. The above presentation suggests reproducible preparation and evaluation of spherical rupturable osmotic capsules.

Table of Contents

List of Tables

List of Figures

1. Introduction

1.1 Pulsatile Drug Delivery System

When the field of pharmaceutics was in its infancy stage, most drugs were administered using conventional dosage forms, such as tablets, capsules or syrups. This provided immediate release of the drug with little control over the rate at which the drug was being released. Moreover, these delivery systems were not able to maintain plasma drug concentrations above the therapeutic level over extended periods of time, which then required repeated drug administration over a period of 24 hours. This would, more often than not, deter patient compliance. To improve patient compliance as well as exert better control over the drug release kinetics to avoid fluctuations in the plasma drug concentrations, controlled drug delivery systems were developed. This ensured near-constant drug levels, within the targeted therapeutic range over extended time durations. This traditional goal of pharmaceutics, namely the development of drug delivery systems with a continuous and/or constant drug release rate, however, does not apply to all circumstances. A pulsatile drug-release pattern, in which the drug is released completely after a well-defined lag time without drug release (Figure 1.1), is advantageous for the following applications[1,2]:

a. Drugs for which patients develop biological tolerance,
b. Drugs to alleviate disease symptoms that vary with circadian rhythms e.g., bronchial asthma, rheumatic disease, ulcer disease, hypertension etc.,
c. Hormones, since they show distinct rhythms,
d. Vaccines and agents that affect the immune system.

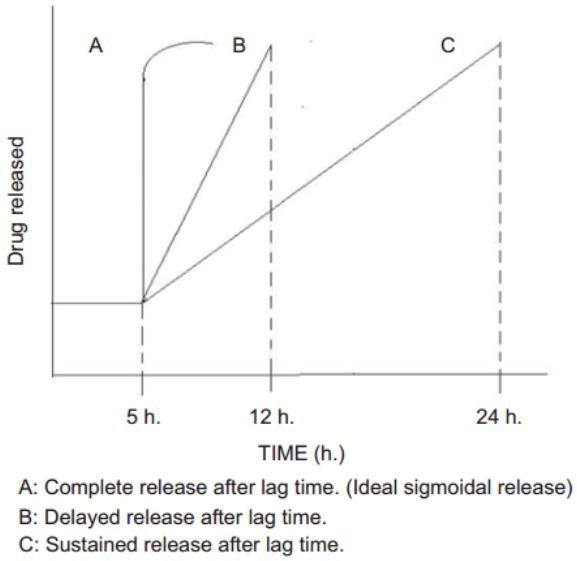

Figure 1.1: Pulsatile Release Profiles[2]

One of the earliest pulsatile release systems was formulated with theophylline for the treatment of asthma. There is a high likelihood of exacerbation of asthma symptoms during the early morning hours, especially near 4 AM.[3] A controlled-release dosage form producing a constant drug release would be non-ideal; a therapeutic scheme that takes into consideration the diurnal/nocturnal variation would be preferred. Such a scheme would be realized if a dosage form taken at bed-time can be programmed to initiate drug release in the early morning hours. In another case, a continuous dose of hormones generally either down-regulates or induces hormone receptors on the target cellular membranes and results in undesirable systemic effects. A pulsatile release of hormones, mimicking the circadian expression of hormones in the body, is essential to regulate its function.[4]

Traditionally, programmable infusion pumps have been used to provide pulsatile drug delivery. However, these delivery systems require clinical intervention and hospital visits, that increases patient non-compliance.[5] Recently, ambulatory pumps have been introduced that can be supported on a piece of clothing. However, these are often bulky (about the size of a pager) and are subject to programming errors by patients and sometimes, by clinicians.[5]

Implantable devices comprise a new approach to pulsatile drug release. These delivery systems can be broadly classified based on their release mechanism. The first type of pulsatile drug delivery systems is the time-controlled system. In this type, the drug release is a function of the drug delivery system itself and independent of external stimuli. By modifying parameters that are integral to its formulation, the lag time, that is, the time after administration at which the pulse release will occur, can be modified. It is essentially a reservoir device enclosed in a barrier coating, which either dissolves, erodes or ruptures after a certain time lag.[6-8]

The second type of pulsatile drug delivery systems is the stimuli-induced system, which releases drug in response to physical or chemical stimuli including pH, body temperature, glucose, enzymes, light and magnetism.[9]

Although elegant, the internal stimuli-responsive drug delivery systems cannot be universally applied; glucose sensitive systems can be applied only to cases where high blood glucose level (e.g. diabetes) can serve as a stimulus, pH sensitive systems can be applicable only when there is a significant difference in microenvironment pH compared to the systemic pH (e.g. cancer, inflammation, etc.), while no internal stimuli are present to trigger subcutaneous release of say, vaccines. On the other hand, the utility of systems

sensitive to external stimuli depends on specialized external devices to apply the suitable trigger.

Therefore drug delivery, which can be programmed by considering solely the formulation aspects of the system, is much simpler and may have broader applicability. A time-controlled explosion capsule, with osmosis as the underlying mechanism of hydrostatic pressure build-up in the core and burst of capsule shell, is one such type of pulsatile release system.

1.2 Osmotic time-controlled system

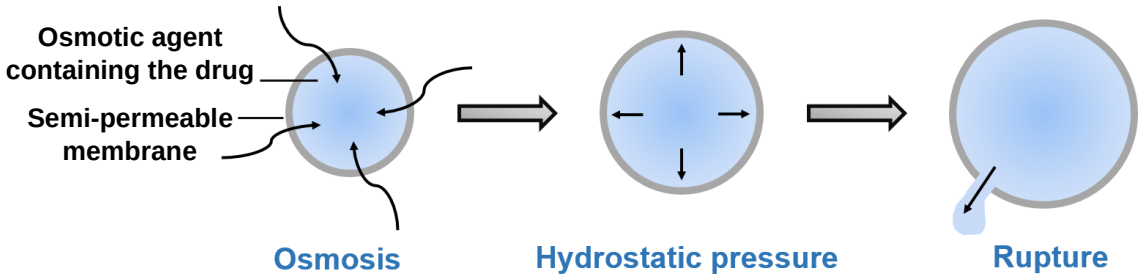

Figure 1.2: Schematic representation of an osmotic bursting device when placed in a biological fluid

An objective of this study was to develop a spherical, biodegradable osmotic capsule. An osmotic capsule consists of a reservoir containing an osmotic agent (osmogent) and the drug, encapsulated by a shell, which is selectively permeable to water. The osmotic pressure generated in the capsule core by the osmotic agent drives the influx of water at a controlled rate until the hydrostatic pressure developed overcomes the tensile strength of

the shell. The ultimate result is rupture and instantaneous release of the payload (Figure 1.2).

The time to rupture is a function of the core osmotic pressure, capsule radius, shell thickness, and tensile properties. Hence, another objective of this study was to mathematically model the entire process described in Figure 1.2 and accurately determine the time lag before capsule rupture occurred. The model takes into consideration the variation in osmotic pressure that occurs with dilution of the osmotic agent solution. Because, majority of polymers display elastoplastic rather than simple elastic behavior, the model also takes into account the imminent non-linearity in hydrostatic pressure exerted against the capsule shell.

1.3 Formulation of the capsule shell

A dip-coating technique was used to formulate a spherical capsule shell. A hydrophobic, selectively water-permeable polymer is a leading candidate for the shell material to prevent leaching of osmogent ions or molecules from the capsule. In addition, the polymer should also be biocompatible and ideally biodegradable. However, the degradation process should commence after burst and release of the payload to prevent variation in polymer properties that are used to predict the precise time of burst. Poly(lactic acid-co-glycolic acid) (PLGA) is one of the most commonly used polymers for drug delivery and tissue engineering applications, that is certified by the US Food and Drug Administration.[13] A polyester-type of polymer, PLGA, is biocompatible and biodegradable through hydrolysis of the internal ester linkages between lactic and

glycolic acid monomers in aqueous systems (Figure 1.3). The byproducts are readily eliminated by natural pathways in the body.[14-15]

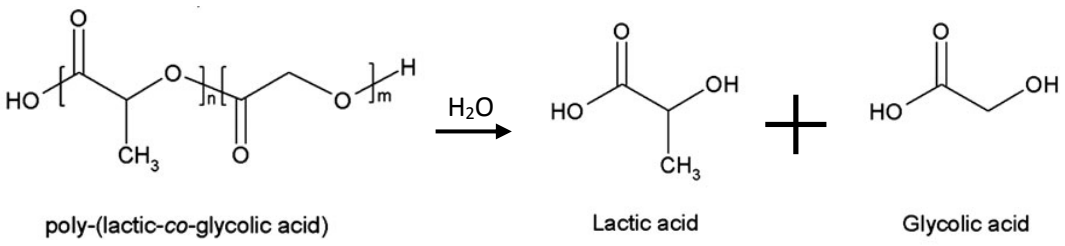

Figure 1.3: PLGA degradation by hydrolysis

In the present study, we use a copolymer of LA and GA in a ratio of 85:15 with a viscosity-average molecular weight of 363 kDa (Inherent viscosity 2.3). Due to the high LA content, this polyester is hydrophobic.

1.4 Structure of Thesis

Predicting the time of rupture of an osmotic capsule requires further characterization of change in mechanical properties of PLGA with hydration, which is an objective of this thesis.

In Chapter 2, hydration and degradation of PLGA with time and its water permeability is determined. In Chapter 3, elastoplastic and failure characterization of PLGA is conducted as a function of hydration under uniaxial stretch, and by a novel "beach ball" inflation technique. In Chapter 4, a method to prepare spherical osmotic capsules is described. A mathematical model to predict the time of rupture of capsules as a function of shell

thickness, radius of the sphere, core osmotic pressure and membrane tensile properties is developed, and the correlation with in-vitro results is demonstrated.

Chapter 5 proposes future work.

2. Physicochemical Properties of Poly(lactic-co-glycolic acid) (PLGA)

2.1 Introduction

Poly(lactic-co-glycolic acid) (PLGA) is one of the most commonly used polymers in pharmaceutical controlled-release systems.[14] A polyester, PLGA is biocompatible and biodegradable, hydrolyzing to lactic and glycolic acid monomers in aqueous systems. These products are eliminated by natural pathways in the body (Figure 2.1).[13,15]

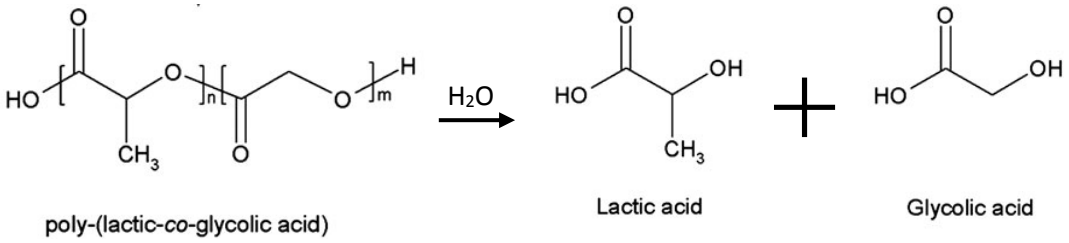

Figure 2.1: PLGA degradation by hydrolysis

In the dry state, PLGA is a hard plastic. When exposed to water, PLGA degrades primarily by the following four steps:

1. Hydration: water penetrates the amorphous region and disrupts hydrogen bonds and van der Waals forces, causing a decrease in the glass transition temperature (T_g)
2. Initial degradation: cleavage of polyester bonds, with a decrease in the molecular weight
3. Autocatalytic degradation: carboxylic end groups autocatalyze the degradation process, and mass loss begins by massive cleavage of the backbone covalent bonds, resulting in loss of integrity
4. Solubilization: fragments are further cleaved to molecules that are water soluble.[13]

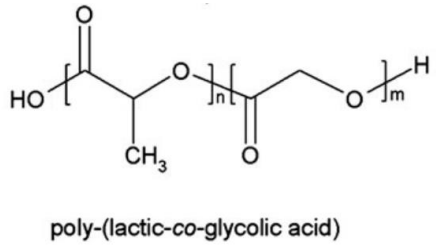

Figure 2.2: Chemical structure of PLGA.

Polyester PLGA is a random copolymer of lactic acid (LA) and glycolic acid (GA) (Figure 2.2). LA contains a methylated asymmetric α-carbon and therefore is more hydrophobic than GA. In the present study, we used a copolymer of LA and GA in a ratio of 85:15 with a viscosity-average molecular weight of 363 kDa (Inherent viscosity 2.3). The lactide-rich copolymer used here is less hydrophilic, absorbs less water and subsequently, degrades more slowly than a glycolide-rich polymer. Hydration and subsequent degradation of PLGA inturn influences the physicochemical and mechanical properties of PLGA such as its crystallinity, glass transition, molecular weight, and tensile strength.[13,15-21]

GA is devoid of methyl side groups and a polymer of GA, poly(glycolic acid) is crystalline.[21] The enantiomeric forms of the optically active LA are D-lactic acid (DLA) and L-lactic acid (LLA). The polymer poly(lactic acid) can be made in either a crystalline form, poly(L-lactic acid) or completely amorphous form, poly(DL-lactic acid).[13] PLGA used here is a copolymer of crystalline LLA and GA. PLGA, consisting of monomers that can potentially render 100% crystallinity to the polymer, is in fact not 100% crystalline, due to the presence of defects such as chain-ends, chain-folds, entanglements and tie-chains which introduce regions of disorder.[16] Also, formation of a crystalline unit

requires alignment of similar monomers, which is difficult in a random copolymer. Thus, this copolymer contains both crystalline and amorphous domains.

Crystallinity of the polymer profoundly affects the degradation kinetics. The characteristically disordered chain sequences and the hydrophilic chain termini in the amorphous regions between the crystalline domains allow rapid water diffusion.[19] Subsequent to hydration, hydrolytic chain scission occurs preferentially in the amorphous regions, reducing the density of tie chains and entanglements while simultaneously increasing the density of the hydrophilic terminal chain ends.[19] The increased density of carboxylic acid end groups in the amorphous domains accelerates the hydration and degradation processes and enhanced mobility of chain sequences enhances crystallite formation.[19] Changes in crystallinity of the polymer and mobility of chain sequences during hydration and degradation can be expected to produce a change in the polymer's mechanical properties, which is explored in the next chapter.

The first step towards degradation of PLGA is hydration. Crystallinity and hydrophobicity of the polymer determine the hydration and degradation kinetics, which in turn influence the physicochemical and mechanical properties.[15-16] Thus, the physicochemical and mechanical characterization of the polymer as a function of hydration is a prerequisite to developing an osmotic capsule with a pre-determined burst time.

Objective

We chose a copolymer with 85:15 ratio of PLA/PGA (85/15 PLGA) to study osmosis during the initial period when degradation was insignificant. The time elapsed until the first evidence of degradation was initially determined. Hydration of PLGA during the initial period was studied, along with its effect on the glass transition temperature. To predict the rate of water influx into PLGA capsules, the water permeability was characterized.

2.2 Materials and methods

2.2.1 Materials

Poly(L-lactide-co-glycolide) (85/15 PLGA, $M_w \sim 363$ kDa) was obtained from Purac, Netherlands. All reagents were analytical grade or better and were used as received. Dichloromethane solvent (DCM), and the salts, sodium chloride (NaCl) and lithium chloride (LiCl), were purchased from Fischer-Scientific (Hampton, NH), Mallinckrodt PLC (St. Louis, MO) and Sigma-Aldrich (St. Louis, MO), respectively. Poly(vinylalcohol) polymer (M_w 85 -124 kDa, 87-89% hydrolyzed) was obtained from Sigma-Aldrich (St. Louis, MO).

2.2.2 PLGA film fabrication

PLGA films were cast from a 7% (w/v) polymer solution in DCM on an aluminum surface (diameter 9.5 cm; VWR) placed on a leveled table in a fume hood. Five different volumes of the polymer solution were cast to obtain five films of distinct thickness,

determined using a micrometer (Table 2.1). The films were dried at room temperature and under atmospheric pressure for the first 48 hours. Complete residual solvent removal was carried out by step-wise increase in drying temperature, from 35 to 55℃ under atmospheric pressure over a period of 4 days. The dried films were stored in a desiccator until use.

Volume of 7% w/w PLGA in dichloromethane (mL)	Average Thickness (µm)
15	37 ± 4.9
20	51 ± 3.4
25	66 ± 2.7
30	88 ± 3.4
35	107 ± 7.9

Table 2.1: Volume of PLGA in DCM solution cast and resulting membrane thickness.

2.2.3 Hydration and degradation characterization of PLGA

Three sets of PLGA films of varying thickness were weighed (W_1). The first set of samples was placed in glass scintillation vials (Fisher), each, containing 20 mL of either 0.2 M phosphate-buffered saline (PBS; pH = 7.0; VWR, Pennsylvania, US) or distilled water, and placed in a 37℃ environment with shaking for 20 days. The pH of the distilled water was monitored to detect the presence of acidic degradation products over the duration of study. Three samples per film thickness were withdrawn every 48 hours from PBS media, patted dry with a tissue paper, and weighed again (W_2). The samples were then completely dried in a vacuum desiccator until a constant mass (W_3) was obtained.

The second set of samples of varying thickness was placed in a vacuum desiccator and the third set was maintained under atmospheric conditions (RH ≈ 70%), through the course of study.

The percentage of water uptake was obtained using the equation

$$\%\, water\ uptake = 100 * \ (W_2 - W_3)/W_3$$

The percentage of PLGA degradation was determined using the equation

$$\%\, PLGA\ degraded = 100 * \ (W_1 - W_3)/W_1$$

Water uptake was also measured using a Coulometric KF Titrator (C20, Mettler Toledo, Columbus, OH). To a portion of film (mass ≈ 10 mg) withdrawn every 48 hours from the PBS media above, 1mL of anhydrous methanol was added, and the samples were occasionally shaken for 1 hour. A small volume (200 μL) of methanol was withdrawn and injected into the titration vessel. Each measurement was performed in triplicate and the water content (w/w) was calculated according to.

$$\%\, water\ uptake = 100 * \ (W_{Water} - W_{Blank})/W_{Initial}$$

where W_{Water} is the mass of water in the sample, W_{Blank} is the mass of water in methanol, and $W_{Initial}$ is the initial mass of the film portion.

The plasticizing effect of water on the polymer was ascertained by determination of the glass transition temperature (T_g). T_g was determined using differential scanning calorimetry (DSC Q2000, TA Instruments, Eden Prairie, MN). Samples of about 0.5–1 mg were weighed in aluminum pans that were hermetically sealed, and subjected to two cooling and heating cycles from −60℃ to 150℃, at rates of 5℃/min. The DSC cell was purged with dry nitrogen at 60 mL/min. The system was calibrated using an indium

standard. Data were treated with Thermal Solutions software (TA Instruments, Eden Prairie, MN), and the results expressed as the mean of three determinations.

The Gordon-Taylor equation relates the $T_{g(mix)}$ of a noninteracting binary system (e.g., polymer, water) to the T_g's of the individual components (T_{g1} and T_{g2}) and their weight fractions, w_1 and w_2.[16,20-21] This equation is often used to describe the plasticizing effect of water in a polymer matrix and is given by the following.

$$T_{g(mix)} = \frac{\left[\left(w_1 T_{g1}\right) + \left(K w_2 T_{g2}\right)\right]}{\left[w_1 + K w_2\right]} \quad (2.1)$$

K is a constant, whose value can be calculated based upon free volume theory[22], using the Simha-Boyer rule.[16]

$$K = \frac{\rho_1 T_{g1}}{\rho_2 T_{g2}}$$

where, ρ_1 is the density of water (1 g/cm^3), and ρ_2 is the density of PLGA (1.24 g/cm^3 *from* Material Datasheet). The T_{g1} of water was estimated to be 135 K[19], and T_{g2} of dry polymer was 333 K (DSC measurement of dry polymer).

2.2.4 Osmotic pressure determination of saturated osmotic agent solutions

Saturated solutions of various osmotic agents, salts and sugars, were prepared at 37℃ and placed undisturbed for 48 hours to reach equilibrium. Water activity was measured at 37℃ using a water activity meter (AquaLab Series 3 TE, Decagon Devices, Inc., Pullman, WA). Water activity was calculated by measuring the vapor pressure of the saturated solutions using a chilled mirror dew-point technique and dividing the measured

vapor pressure by the vapor pressure of pure water.[23] The osmotic pressure, π, was then calculated from the water activity, a_w, using the equation.

$$\pi = -RTln(a_w) \quad (2.2)$$

The water activity meter was calibrated using saturated sodium chloride, potassium chloride and lithium chloride solutions provided by the manufacturer.

2.2.5 Membrane permeability characterization

PLGA membrane permeability coefficient was determined by recording the osmotic pressure-driven rate of water influx across PLGA membranes of fixed area but varying thicknesses. Two 2.5x2.5 cm PLGA films were stacked together with a 2x2 cm aluminum sheet inserted in the reservoir area between the two films. Lips of PLGA surrounded aluminum on three sides. This assembly was thermally bonded at 80℃ under 345 kPa pressure for 5 minutes in the Carver press (Model 4386, Carver, Inc. Wabash, IN). The aluminum sheet was removed from the assembly, and a mixture of saturated osmogent (sodium chloride) and a food dye were loaded into the reservoir area by a syringe (150 µL per bag). Food dye was added to detect leaks. Solid sodium chloride (12 mg) was also added to the bag to maintain a constant osmotic pressure during the study. Then, the open edge of the bag was sealed using a heat sealer (Model FS-305, Sealersales, Inc., Northridge, CA).

The bag was washed with distilled water before placing into PBS at 37℃ (Figure 2.3). The bag was withdrawn every hour for 12 hours, patted dry with a tissue paper and weighed. Triplicate measurements were made for each thickness of the film and the

permeability coefficient, *k*, was determined from the equation for water influx by osmosis.

$$\frac{dV}{dt} = \frac{kA}{h}\Delta\pi \tag{2.3}$$

where, *dV/dt* is the volume flux of water, *A* is the surface area available for osmosis, *h* is the thickness of the membrane and $\Delta\pi$ is the osmotic pressure. During the first 12 hours, the hydrostatic pressure was assumed to be negligible; hence, measurements were limited to this time interval.

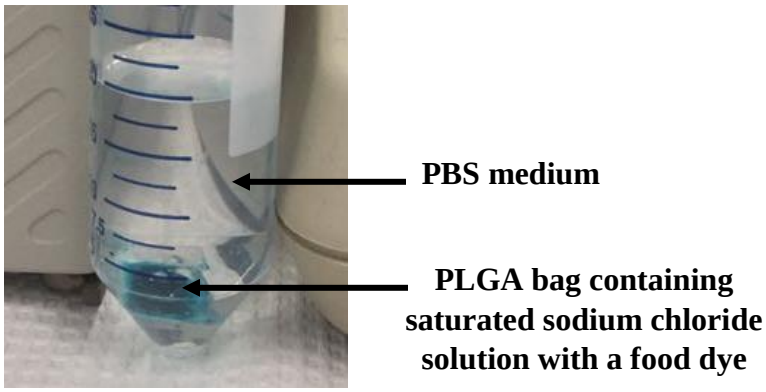

Figure 2.3: Set-up for PLGA membrane permeability coefficient determination.

2.3 Results and Discussion

2.3.1 PLGA film fabrication: Residual solvent determination

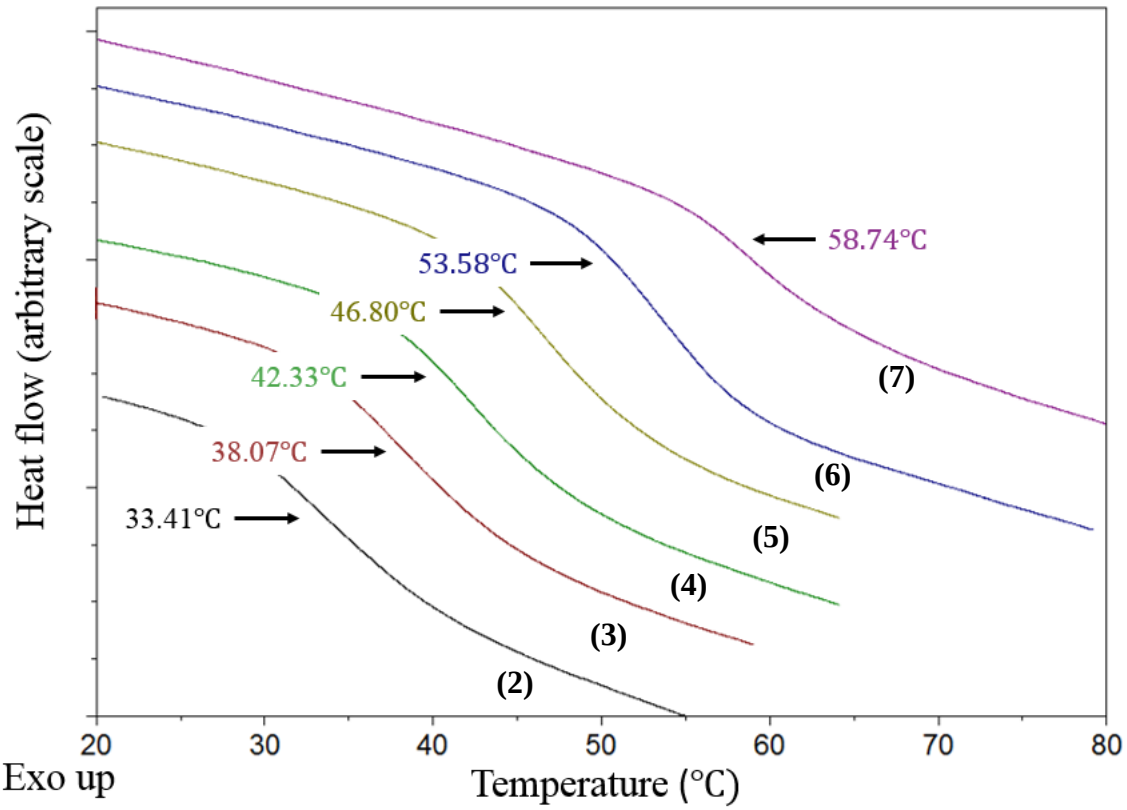

Figure 2.4: Glass transition temperature of PLGA during drying process. (Numbers from (2) to (7) indicate the sequence of steps in the drying regime, shown in Table 2.2)

PLGA films of thickness ranging from 37 to 100 µm were solvent cast using PLGA in DCM solution. The films were dried until complete solvent removal. Presence and absence of residual solvent was determined by measuring the T_g of PLGA. After 48 hours of drying at room temperature, the T_g of PLGA was found to be close to 31°C. The polymer was then dried at a temperature just below its T_g at 30°C over 15-18 hours, which resulted in a T_g to 33°C. This process was repeated until a T_g > 55°C was obtained

(Figure 2.4). A T_g close to 60℃ indicated the near-absence of the solvent. Based on this, the drying regimen adopted for PLGA throughout the study (that is, for PLGA films and capsules prepared in Chapters 3 and 4) is summarized in Table 2.2.

Step number in sequence	**Drying Temperature (℃)**	**Drying Time (hours)**
1	Room temperature	48
2	30	16
3	35	16
4	40	16
5	45	16
6	50	16
7	55	16

Table 2.2: Drying regime of PLGA

2.3.2 Water as a plasticizer

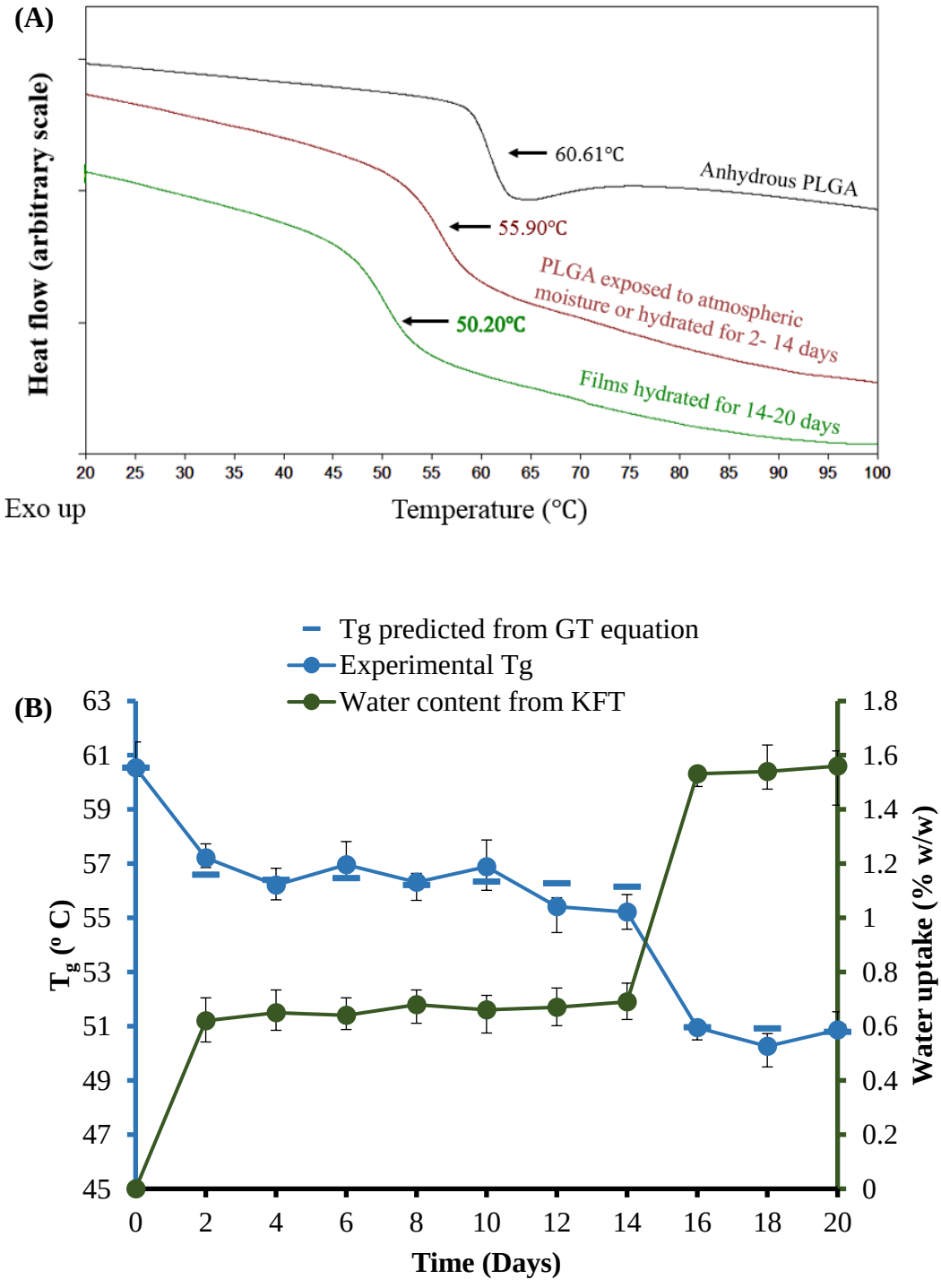

Figure 2.5: Water uptake by PLGA and subsequent reduction in T_g (A) DSC data (B) Summary

The first step towards degradation is the hydration of PLGA (*see* Section 2.1). Mass of water uptake did not show a significant increase due to lack of sensitivity of the weighing balance. Water uptake by PLGA was also determined using KFT. By KFT, it was determined that 0.65% (w/w) water was taken up, when PLGA was exposed to the atmospheric moisture or exposed to water for 2 days. This amount remained fairly stable until Day 14, which marked the onset of degradation, following which water was taken up to an extent of 1.5% w/w. Water was a plasticizer, as demonstrated by a reduction in the glass transition temperature of PLGA presumably due to an increase in chain motility in the glassy or amorphous domains of PLGA. After this initial drop, the T_g values appeared to reach a plateau at ~ 56℃ through 14 days after which a second descent to ~ 50℃ was seen. The reduction in glass transition temperatures predicted using the Gordon-Taylor equation (Eq. 2.1) closely followed that obtained by DSC measurements (Figure 2.5).

2.3.3 PLGA degradation

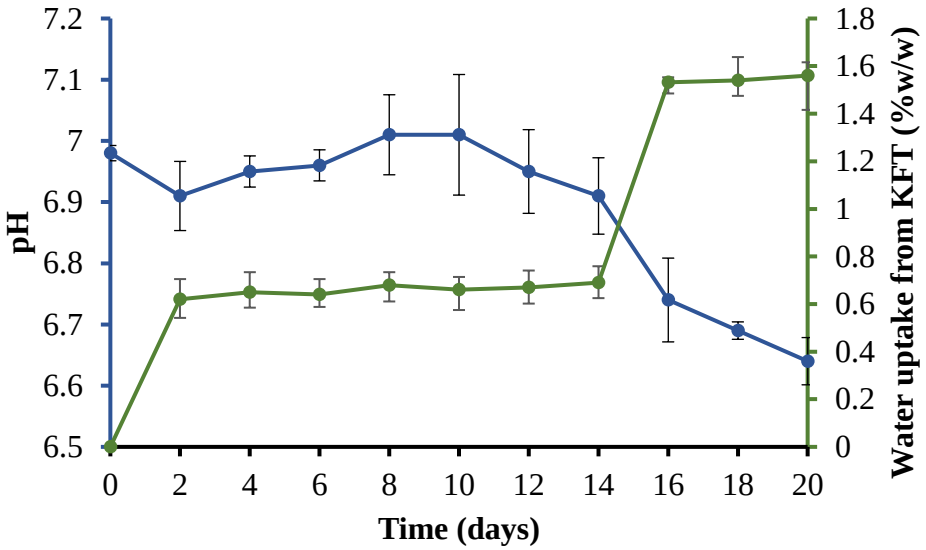

Figure 2.6: pH decreases due to PLGA degradation**.**

The degradation kinetics of 85/15 PLGA was determined by mass loss of PLGA specimen and pH decrease of the hydration medium (DI water). A significant mass loss was not observed due to lack of sensitivity of the weighing balance. On the other hand, a significant decline in the pH of DI water was observed on Day 14, marking the commencement of degradation of PLGA into its acidic products (Figure 2.6). The drop in pH was coincident with an abrupt increase in the water content on Day 2 and 14, respectively, as determined by KFT. The abrupt increase in hydration on Day 2 can be attributed to the preferential hydration of amorphous domains of the polymer. Interaction of water with the polyester bonds produces hydrolytic cleavage of chain sequences, increasing the density of hydrophilic chain ends in the amorphous domains on Day 14. Addition of more hydrophilic chain ends then brings about an abrupt increase in hydration.[7]

2.3.4 Permeability characterization of PLGA

The water activity of saturated solutions of various salts and sugars was measured using the water activity meter. Osmotic pressure was determined from the water activity (Eq. 2.2) and was plotted as a function of its water solubility (Figure 2.7).[24] The salts, sodium chloride and lithium chloride, exerted a high osmotic pressure at a relatively low solubility. These salts were selected for use in osmotic capsules, as the high osmotic pressure would draw water in the capsules relatively rapidly while the low solubility would cause relatively small fluctuations in the osmotic pressure with dilution of the saturated solutions.

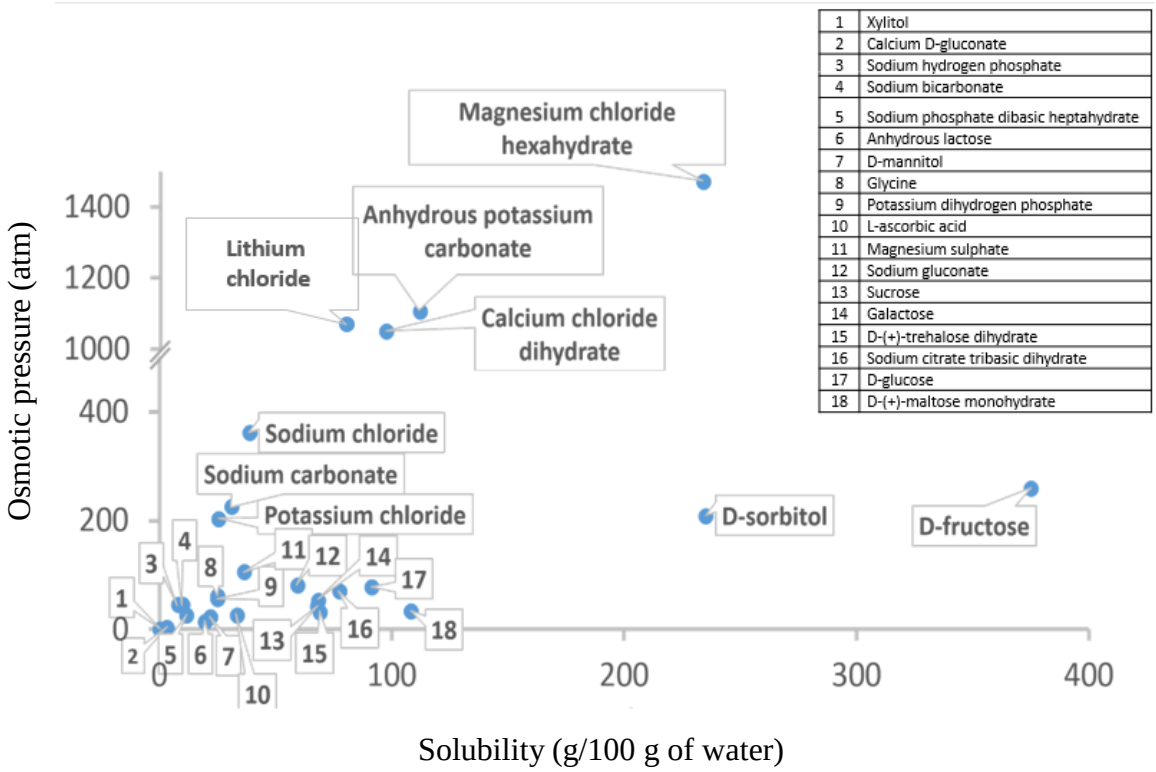

Figure 2.7: Osmotic pressure and solubility of various osmotic agents.

To determine the membranes' permeability, water uptake by PLGA bags of known membrane thickness and surface area available for osmosis, containing saturated sodium chloride solution, was determined (Figure 2.8)

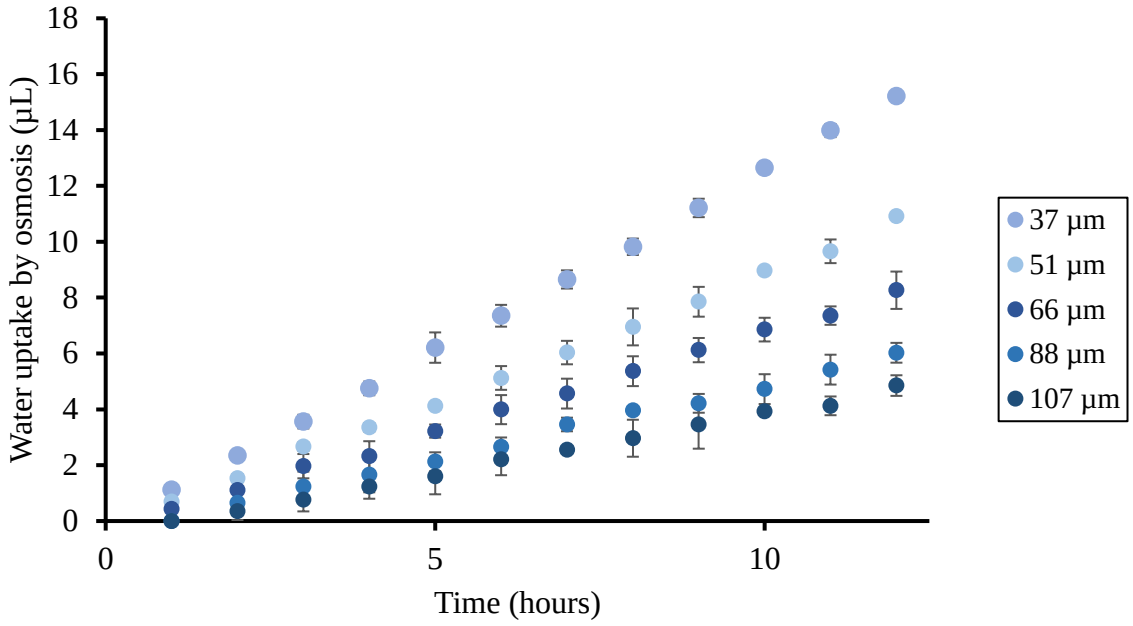

Figure 2.8: Water uptake kinetics (osmosis) by PLGA bags of different membrane thickness.

The rate of water uptake increased with decreasing membrane thickness, given a constant surface area available for osmosis and constant osmotic pressure of the salt solution. There was an initial time lag (T_{lag}) before water uptake occured, which was a function of membrane thickness h and the diffusion coefficient of water in PLGA, D.[25]

$$T_{lag} = \frac{h^2}{6D}$$

By plotting T_{lag} vs h^2 , the diffusion coefficient of PLGA was determined from the slope (Figure 2.9) as 4.75 x 10^{-13} m^2/s

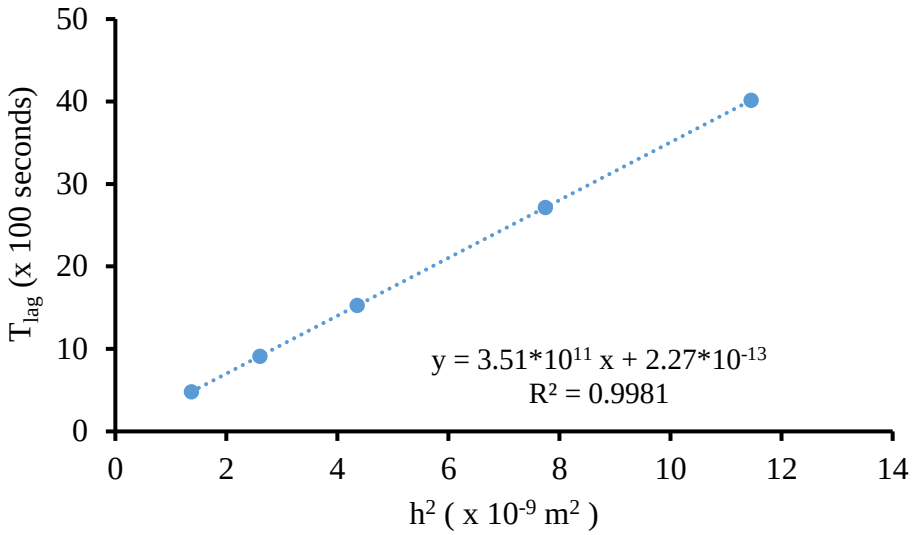

Figure 2.9: Plot of T_{lag} versus d^2 to determine PLGA hydraulic diffusion coefficient.

Furthermore, by plotting volume influx per unit area and time against the inverse of thickness (Eq. 2.3), water permeability coefficient *k* was determined from the slope (Figure 2.10).

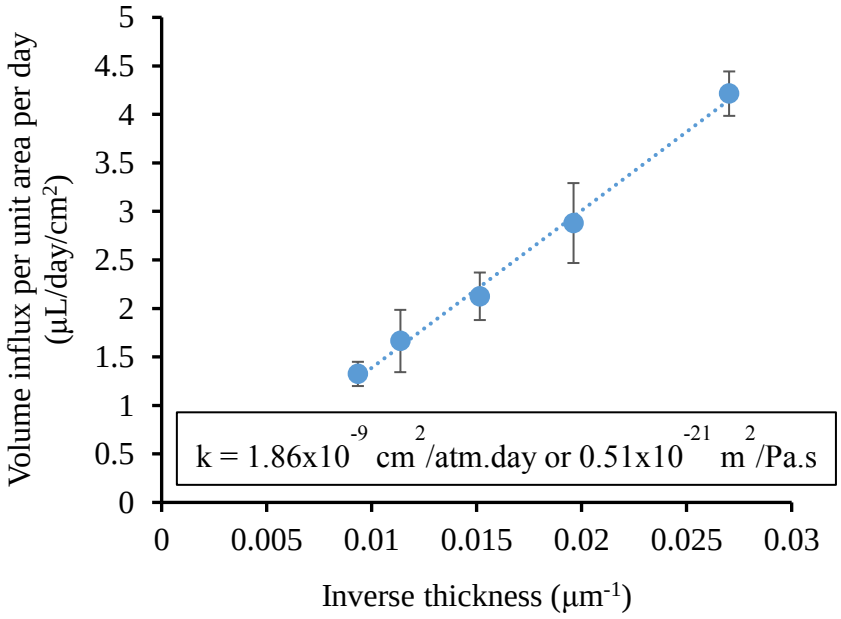

Figure 2.10: Plot of Volume influx per unit area and time against the inverse of thickness to determine PLGA hydraulic permeability coefficient.

2.4 Conclusions

A drying regime was determined to ensure complete elimination of DCM from the solvent-cast PLGA films. When exposed to water at 37℃, degradation of PLGA was shown to commence from Day 14. Thus, all the studies described in the next chapters were restricted to this time point.

The first step to degradation was hydration. The water content of PLGA films exposed to atmospheric moisture or placed in water was found to be 0.65% w/w. This level remained constant for 14 days followed by an increase in hydration which coincided with the commencement of degradation. Hydration of PLGA was accompanied by a decline in its glass transition temperature, reflecting the plasticizing effect of water.

The capsule expansion by osmosis is opposed by hydrostatic pressure developing against the walls of the shell. Capsule rupture occurs, when the hydrostatic pressure exceeds the tensile strength of the material. Since the time to capsule rupture is a function of PLGA's mechanical properties, which in turn may change as a function of PLGA hydration, it becomes necessary to quantify the change in mechanical properties at different degrees of hydration. This will be explored in Chapter 3.

The PLGA permeability coefficient was 1.86×10^{-9} cm^2/atm.day. This value was used in the determination of water uptake by PLGA capsules in the subsequent chapters.

3. Mechanical properties of Poly(lactic acid-co-glycolic acid) (PLGA)

3.1 Introduction

PLGA is a pharmaceutically acceptable polymer[13] that has the potential to be used as a coating material of an osmotic delayed-burst release system owing to its hydrophobicity and selective water permeability (*see* Section 2.3.4). Apart from its physicochemical properties, knowledge of the mechanical properties is important, because these properties determine the polymer behavior before the capsule ruptures when placed in a biological medium. Based on similar studies done earlier, mechanical properties of this polymer were hypothesized to be influenced by the presence of water.[19] This hypothesis is based on the plasticizing effect that water has on the polymer, which is reflected by reduction in the glass transition temperature (T_g) of hydrated samples (*see* Section 2.3.2). Ultimately, physicochemical and mechanical characterization of PLGA helps determine and program the time of rupture of PLGA osmotic capsules when placed in a biological medium.

Objectives:

1. Free films are often used to analyze the effect of hydration on the polymer's mechanical properties by uniaxial and/or biaxial tensile tests or compression/puncture tests.[18,26] The rationale is that the properties of the polymer are easier to study in a free-film form than when coated on a substrate. To this end, we conducted a uniaxial tensile testing study to demonstrate the effect of hydration on the mechanical properties of the free film. Uniaxial tensile testing provided information about the elasticity, plasticity, breaking strength and elongation ability of the PLGA film.

2. Mathematical model for elastoplastic expansion of a sphere was developed to relate the hydrostatic pressure in the capsule to the tangential stress in the shell.
3. The true hydrostatic pressure developed in the capsule was determined by a novel "beach-ball" inflation technique. Elastic, plastic, and failure properties of spherical PLGA shells of two thicknesses, two capsule radii and at two degrees of moisture exposure were evaluated. The experimental results were evaluated with the mathematical model.

3.2 Theory

3.2.1 Theory of Uniaxial Test

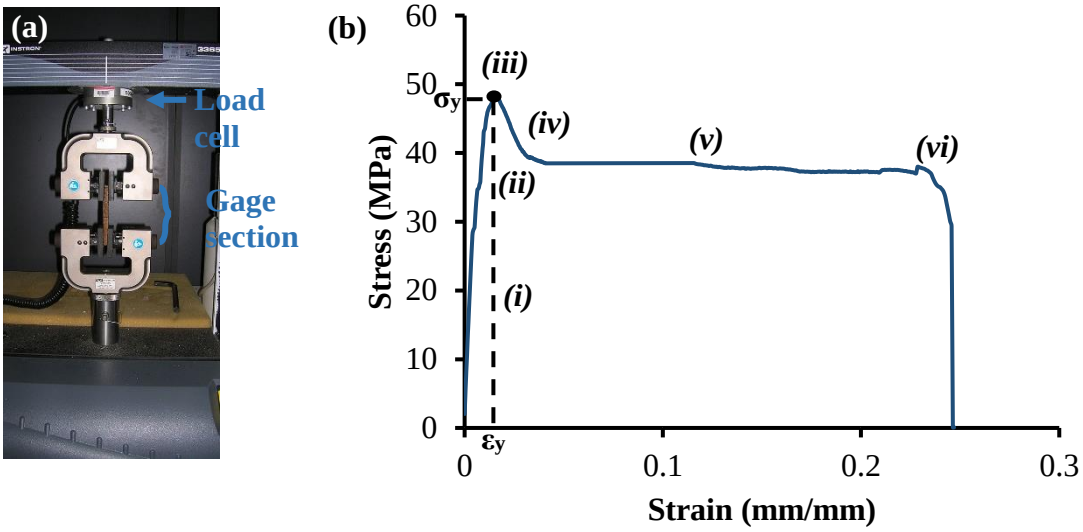

Figure 3.1: (a) A uniaxial tensile tester **(b)** A typical stress-vs-strain curve for 85/15 PLGA

Tensile testing is a fundamental material science test in which a sample is subjected to a controlled tension until failure. A uniaxial tensile test is widely used in characterizing the mechanical properties of a material subjected to a constant deformation rate-procedure. The test involves placing the test specimen in the testing machine and slowly extending until fracture occurs. During this process, the separation of the gage section is recorded against the applied force (Figure 3.1a). The output from a uniaxial tensile tester represents the mean stress, acting over the current cross-sectional area, against a measure of the total strain. If the length of a tensile specimen is increased from l_o to l, the extent of deformation is customarily measured as engineering or conventional strain ε.

$$\varepsilon = \frac{l - l_0}{l_0}$$

The stress σ, in a uniaxial test, is given by,

$$\sigma = \frac{L}{A} = L\left(\frac{l}{A_0 l_0}\right) = \frac{L(1-\varepsilon)}{A_0} \tag{3.1}$$

where, L is the load applied on the specimen, A is the current cross-sectional area and A_0 is the initial cross-sectional area of the specimen.[27]

The stress-strain curve of a PLGA film under uniaxial loading has the shape shown in Figure 3.1b. In the constant deformation rate-procedure of the tensile tests, there were five distinctly identifiable processes:

i. Linear stress growth in the low strain elastic regime
ii. At about 2%, there is an elastic regime where the stress increases more slowly than linearly.
iii. A point of zero slope is reached corresponding to a local stress maximum at the so-called 'yield peak'.
iv. A drop in the stress with strain due to strain softening.
v. Plastic flow regime characterized by a near constant or slightly declining plateau stress
vi. At higher deformation, the material fails.

The course of elastoplastic deformation behavior is strongly dependent upon the underlying microstructure of PLGA, that is, the molecular orientation of PLGA chains and its crystallinity.

The elasto-plastic deformation laws, elaborated in the next section, account for the initial linearity between stress and strain followed by non-linearity.

Elasto-plastic Analysis

At small strains, PLGA deforms elastically and regains its original shape when the deforming force is removed. The linear stress versus strain relationship in the elastic region is governed by Hooke's law of elasticity,

$$\sigma = E\varepsilon \tag{3.2}$$

where, E is the elastic modulus, a measure of an object's resistance to being deformed elastically.[28]

PLGA behaves elastically until the deforming force exceeds the elastic limit, which is known as the yield stress σ_y. The corresponding strain is denoted as ε_y. At this point, the polymer is permanently deformed and fails to return to its original shape when the force is removed. This phenomenon is known as plastic deformation. An empirical formula to fit the stress-strain curve during plastic deformation is the power law given by Holloman as,

$$\sigma = G(\varepsilon)^n H(\varepsilon - \varepsilon_y) \tag{3.3}$$

where, G is the strength index or plastic modulus, n is the strain hardening or softening exponent, and $H(\varepsilon - \varepsilon_y)$ is the Heaviside step function. G and n are arbitrary constants determined by curve fitting.[27]

Stress versus strain curves were obtained by conducting uniaxial tensile test on PLGA films. By curve fitting, the elastic and plastic moduli (E and G, respectively) and the strain softening/hardening component (n) were determined.

3.2.2 Theory of the Beach-ball inflation technique

In this section, we recapitulate the derivation of the equation for expansion of hollow elastic sphere due to luminal pressure.[4] We then show how the results simplify when the elastic material is a thin shell. Before developing a model for the spherical geometry, consider a rectangular strip subjected to uniaxial tensile stress (Figure 3.2).

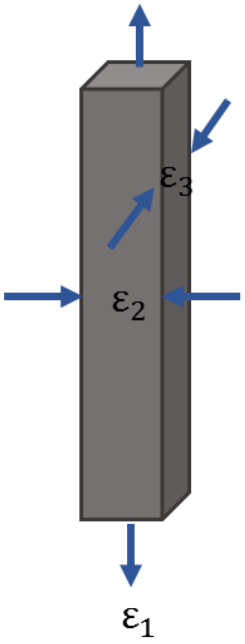

Figure 3.2: A rectangular strip subjected to uniaxial tensile test

The length of the strip increases in the direction of load application, that is along direction 1. Applying Hooke's law to this material undergoing elastic deformation, the strain, ε_1, in the direction of load is given by

$$\varepsilon_1 = \frac{\sigma_1}{E}$$

In the two directions perpendicular to the direction of uniaxial load, the length shrinks such that the strains are given by

$$\varepsilon_2 = -\upsilon\frac{\sigma_1}{E}$$

$$\varepsilon_3 = -\upsilon\frac{\sigma_1}{E}$$

where υ is the Poisson ratio

When the material is strained in directions 2 and 3 instead, we get similar relationships, that is,

$$\varepsilon_1 = -\upsilon\frac{\sigma_2}{E} \qquad \varepsilon_2 = \frac{\sigma_2}{E} \qquad \varepsilon_3 = -\upsilon\frac{\sigma_2}{E} \qquad (Strain\ in\ 2)$$

$$\varepsilon_1 = -\upsilon\frac{\sigma_3}{E} \qquad \varepsilon_2 = -\upsilon\frac{\sigma_3}{E} \qquad \varepsilon_3 = \frac{\sigma_3}{E} \qquad (Strain\ in\ 3)$$

The above relationships can be re-written in the matrix form of what is known as the elastic constitutive relation,

$$\begin{bmatrix}\varepsilon_1\\ \varepsilon_2\\ \varepsilon_3\end{bmatrix} = \begin{bmatrix}\frac{1}{E} & -\frac{\upsilon}{E} & -\frac{\upsilon}{E}\\ -\frac{\upsilon}{E} & \frac{1}{E} & -\frac{\upsilon}{E}\\ -\frac{\upsilon}{E} & -\frac{\upsilon}{E} & \frac{1}{E}\end{bmatrix}\begin{bmatrix}\sigma_1\\ \sigma_2\\ \sigma_3\end{bmatrix} \qquad (3.4)$$

Spherical geometry[27]

Consider now a spherical shell of thickness *h* (Figure 3.3). Let the inner radius of the shell be, *a*, and the outer radius be *b*, so *h = (b – a)*. The core contains an osmotic agent, which exerts a specified osmotic pressure to draw water from the exterior into the core

through the semi-permeable membrane shell by osmosis. Entry of water increases the hydrostatic pressure, *p*, exerted against the inner side of the shell, resulting in expansion.

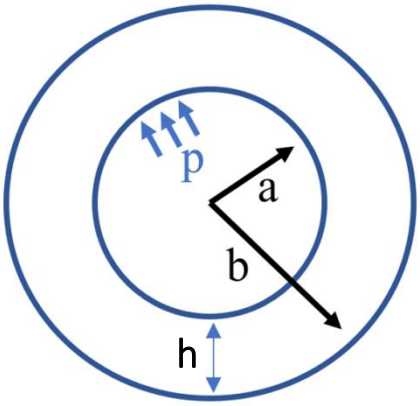

Figure 3.3: A sphere under internal hydrostatic pressure

PLGA polymer (fabricated by solvent casting) was determined to be an isotropic, elastoplastic material until it yields (as will be seen in the results later). To ascertain the hydrostatic pressure at rupture/burst, we developed an elastoplastic analysis model for expansion of the sphere. In this model for a spherical shell, deformations only depend on the radial distance, *r*, from the center. The spherical coordinates are depicted in Figure 3.4.

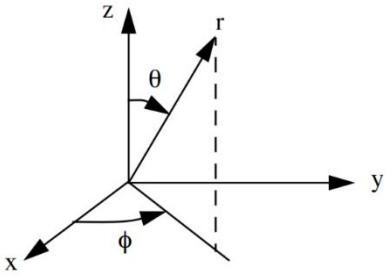

Figure 3.4: Spherical Coordinate System

According to this model,

$$r_{inital} \rightarrow r_{inital} + u(r)$$

At small deformations, distances are distributed according to

$$dr \rightarrow dr\,(1 + u'(r))$$

$$r\,d\theta \rightarrow d\theta\,(r + u(r))$$

r cosθ dθ (projection of azimuthal axis on polar axis) $\rightarrow \big(\mathrm{r} + \mathrm{u(r)}\big)\cos\theta\, d\theta$ etc.

The associated strains are given by,

$$\varepsilon_{rr} = \frac{dr\,\big(1 + u'(r)\big) - dr}{dr} = u'(r) = \frac{du}{dr} \tag{3.5}$$

$$\varepsilon_{\theta\theta} = \frac{d\theta\,(r + u(r)) - r d\theta}{r d\theta} = \frac{u(r)}{r}$$

$$\varepsilon_{\varphi\varphi} = \frac{d\varphi\,\cos\theta\,\big(r + u(r)\big) - r\,\cos\theta\,d\varphi}{r\,\cos\theta\,d\varphi} = \frac{u(r)}{r} = \varepsilon_{\theta\theta} \tag{3.6}$$

Under the condition of spherical symmetry with a homogeneous isotropic material,

$$\left.\begin{aligned} \varepsilon_{\theta\theta} &= \varepsilon_{\varphi\varphi} \\ \sigma_{\theta\theta} &= \sigma_{\varphi\varphi} \\ \sigma_{r\theta} = \sigma_{r\varphi} &= \sigma_{\theta\varphi} = 0 \end{aligned}\right\} \tag{3.7}$$

Further simplifying the notation, we define the radial and tangential components of stress and strain:

$$\sigma_{rr} = \sigma_r\,, \varepsilon_{rr} = \varepsilon_r$$

$$\sigma_t = \sigma_{\theta\theta} = \sigma_{\varphi\varphi}, \varepsilon_t = \varepsilon_{\theta\theta} = \varepsilon_{\varphi\varphi}$$

Since the radial and the two tangential components of stress and strain are in mutually perpendicular directions, the elastic constitutive relationship from Eq. 3.4 becomes,

$$\begin{bmatrix}\varepsilon_t\\ \varepsilon_t\\ \varepsilon_r\end{bmatrix} = \begin{bmatrix} 1/E & -\upsilon/E & -\upsilon/E\\ -\upsilon/E & 1/E & -\upsilon/E\\ -\upsilon/E & -\upsilon/E & 1/E\end{bmatrix}\begin{bmatrix}\sigma_t\\ \sigma_t\\ \sigma_r\end{bmatrix}$$

or

$$\begin{bmatrix}\varepsilon_t\\ \varepsilon_r\end{bmatrix} = \frac{1}{E}\begin{bmatrix}1-\upsilon & -\upsilon\\ -2\upsilon & 1\end{bmatrix}\begin{bmatrix}\sigma_t\\ \sigma_r\end{bmatrix}$$

Inverting,

$$\begin{bmatrix}\sigma_t\\ \sigma_r\end{bmatrix} = \frac{E}{1-\upsilon-2\upsilon^2}\begin{bmatrix}1 & \upsilon\\ 2\upsilon & 1-\upsilon\end{bmatrix}\begin{bmatrix}\varepsilon_t\\ \varepsilon_r\end{bmatrix}$$

$$\begin{bmatrix}\sigma_t\\ \sigma_r\end{bmatrix} = \frac{E}{(1+\upsilon)(1-2\upsilon)}\begin{bmatrix}\varepsilon_t+\upsilon\varepsilon_r\\ 2\upsilon\varepsilon_t+(1-\upsilon)\varepsilon_r\end{bmatrix}$$

or

$$\sigma_t = \frac{E\upsilon}{(1+\upsilon)(1-2\upsilon)}\varepsilon_r + \frac{E}{(1+\upsilon)(1-2\upsilon)}\varepsilon_t \tag{3.8}$$

$$\sigma_r = \frac{E(1-\upsilon)}{(1+\upsilon)(1-2\upsilon)}\varepsilon_r + \frac{2E\upsilon}{(1+\upsilon)(1-2\upsilon)}\varepsilon_t \tag{3.9}$$

Equation of motion

The general equation of motion (Newton's second law) for a deformable solid is

$$\rho\ddot{\bar{u}} = \nabla\bar{\bar{\sigma}} + \bar{f}$$

where $\bar{\bar{\sigma}}$ is the Cauchy stress tensor, $\ddot{\bar{u}}$ is the second derivative of displacement vector with respect to time, $\bar{f}$ is the body force per unit volume and ρ is the mass density.

The equation for motion in the radial direction in spherical coordinates is given by

$$\rho\frac{\partial^2 u_r}{\partial\theta^2} = \frac{\partial\sigma_{rr}}{\partial r} + \frac{1}{r}\frac{\partial\sigma_{r\theta}}{\partial\theta} + \frac{1}{r\sin\theta}\frac{\partial\sigma_{r\varphi}}{\partial\varphi} + \frac{1}{r}\left(2\sigma_{rr} - \sigma_{\theta\theta} - \sigma_{\varphi\varphi} + \sigma_{r\theta}\cot\theta\right) + f_r$$

At equilibrium, which is the condition of interest,

$$\ddot{\bar{u}} = 0$$

Considering spherical symmetry (Eqs. 3.7) at equilibrium and in the absence of body forces, the equation of motion reduces to

$$\frac{d\sigma_r}{dr} + \frac{2}{r}(\sigma_r - \sigma_t) = 0 \qquad (3.10)$$

Taking the external pressure to be zero and the internal pressure to be p, the boundary conditions are:

$\sigma_r(\mathrm{r} = \mathrm{a}) = -\mathrm{p}$

and

$\sigma_r(\mathrm{r} = \mathrm{b}) = 0$ (external pressure is assumed to be negligible)

Substituting Eqs. 3.8-3.9 for σ_t and σ_r along with Eqs. 3.5-3.6 for ε_r and ε_t in the equilibrium Eq. 3.10, we obtain

$$\frac{d^2u}{dr^2} + \frac{2}{r}\frac{du}{dr} - \frac{2u}{r^2} = 0$$

The general solution for this second order differential equation is

$$u = C_1 r + \frac{C_2}{r^2} \tag{3.11}$$

Substituting Eq. 3.11 and its first derivative in Eqs. 3.8-3.9, we get

$$\sigma_t = \frac{E}{(1+\upsilon)(1-2\upsilon)}\left[(1+\upsilon)C_1 + (1-2\upsilon)\frac{C_2}{r^3}\right] \tag{3.12}$$

$$\sigma_r = \frac{E}{(1+\upsilon)(1-2\upsilon)}\left[(1+\upsilon)C_1 - 2(1-2\upsilon)\frac{C_2}{r^3}\right] \tag{3.13}$$

Applying the boundary conditions

$$C_1 = \left(\frac{1-2\upsilon}{E}\right)\left(\frac{a^3}{b^3-a^3}\right)p$$

$$C_2 = \frac{b^3}{2E}\left(\frac{a^3}{b^3-a^3}\right)(1+\upsilon)p$$

Substituting for C_1 and C_2 in Eqs. 3.12-3.13, the radial and tangential stresses during the elastic regime are determined as

$$\boxed{\sigma_r = -\left(\frac{a^3}{b^3-a^3}\right)\left(\frac{b^3}{r^3}-1\right)p} \tag{3.14}$$

$$\boxed{\sigma_t = \left(\frac{a^3}{b^3-a^3}\right)\left(\frac{b^3}{2r^3}+1\right)p} \tag{3.15}$$

The radial displacement is given by

$$\boxed{u(r) = \left(\frac{a^3}{b^3-a^3}\right)\frac{p}{E}\left[(1-2\upsilon)r + \frac{b^3(1+\upsilon)}{r^2}\right]} \tag{3.16}$$

It is convenient to define an equivalent tensile stress or von Mises stress σ_v, which is used to predict yielding of materials under triaxial loading conditions from results obtained with simple uniaxial tensile tests. Thus, we define σ_v for a spherical shell as

$$\sigma_v = \sqrt{\frac{\left(\sigma_\theta - \sigma_\varphi\right)^2 + \left(\sigma_\varphi - \sigma_r\right)^2 + (\sigma_r - \sigma_\theta)^2 + 6\left(\sigma_{r\theta}^2 + \sigma_{\varphi\theta}^2 + \sigma_{r\varphi}^2\right)}{2}}$$

Considering spherical symmetry and the defined notations, the von Mises stress σ_v reduces to

$$\sigma_v = \sigma_t - \sigma_r \tag{3.17}$$

Substituting Equations 3.14-3.15 in Equation 3.17

$$\boxed{\sigma_v = \left(\frac{a^3}{b^3 - a^3}\right)\left(\frac{3b^3}{2r^3}\right)p} \tag{3.18}$$

Thin shell approximation

We now consider the thin shell approximation where, $h = (b - a) < a/20$ (example: spherical capsules of radius 1.5 mm and shell thickness 75 µm).

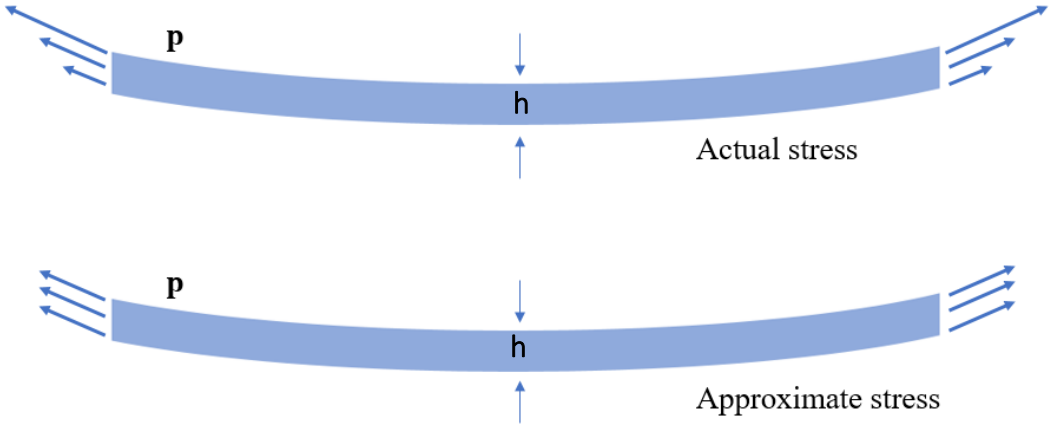

Figure 3.5: Thin shell approximation

First notice that,

$$b^3 - a^3 = (b - a)(a^2 + ab + b^2) \approx 3b^2h$$

Also, notice that,

$$a \lesssim r \lesssim b \qquad (3.19)$$

Substituting for *r*, we obtain to good approximation (substituting Eq. 3.6 in Eq. 3.16),

$$\varepsilon_t = \frac{rp}{3hE}(2 - \upsilon)$$

Since, $\upsilon \approx 0.4$ for PLGA[29-31], thus,

$$\varepsilon_t \approx \frac{rp}{2hE} \qquad (3.20)$$

Elastic regime

From Eqs. 3.14-3.15

$$\sigma_r = -\left(\frac{a^3}{b^3 - a^3}\right)\left(\frac{b^3}{r^3} - 1\right)p \approx -\frac{(b-r)}{h}p$$

$$\sigma_t = \left(\frac{a^3}{b^3 - a^3}\right)\left(\frac{b^3}{2r^3} + 1\right)p \approx \frac{bp}{2h} \tag{3.21}$$

Evidently in the thin film approximation, the tangential stress varies negligibly through the film while the radial stress varies linearly from -*p* to 0.

Per Hooke's law for the elastic regime (Eq. 3.2)

$$\sigma_t = E\varepsilon_t = E\frac{r - r_0}{r_0}$$

Substituting for σ_t in Eq. 3.21

$$\boxed{p_{elastic} = \frac{2hE}{r}\left(\frac{r}{r_0} - 1\right)} \tag{3.22}$$

Plastic regime

From Eq. 3.18,

$$\sigma_v = \left(\frac{a^3}{b^3 - a^3}\right)\left(\frac{3b^3}{2r^3}\right)p \approx \frac{bp}{2h} \tag{3.23}$$

Per Holloman's law, for the plastic regime (Eq. 3.3),

$$\sigma_v = G{\varepsilon_t}^n = G\left(\frac{r - r_0}{r_0}\right)^n$$

Substituting for σ_v in Eq. 3.23

$$\boxed{p_{plastic} = \frac{2hG}{r}\left(\frac{r}{r_0} - 1\right)^n} \qquad (3.24)$$

The hydrostatic pressure, p, so determined during elastic and plastic extension of the spherical capsule from Eqs. 3.22 and 3.24 is subtracted from the osmotic pressure, π, generated in the capsule core to give the net driving force for osmosis $\frac{dV}{dt}$ (Eq. 3.25).

$$\frac{dV}{dt} = \frac{kA}{h}(\pi - p)$$

where, *k* is the permeability coefficient of PLGA, and *A* is the surface area available for osmosis.

3.3 Materials and methods

3.3.1 Uniaxial Tensile Test

A 3x5 factorial design was used to analyze the treatment effects of 3 levels of hydration and 5 of film thicknesses on uniaxial tensile properties (Table 3.1). The films, ranging in thicknesses from 35 -110 µm (prepared as described in Section 2.2.1), were cut into dumbbell-shaped specimens using laser cutting equipment (Universal Laser Systems, Scottsdale, Arizona, USA) (Figure 3.6). Specimens from each of the five thicknesses were subjected to the three levels of hydration treatment (*as described in* Section 2.2.3).

The anhydrous films were vacuum dried for 48 hours after laser cutting and then handled in a nitrogen-dry glove box and stored in moisture–resistant bags. The prepared specimens were tested per ASTM D882 guidelines for tensile testing of thin films.[32] Each specimen was attached to the serrated grips of a Uniaxial Tensile Tester (MTS® Advantage Uniaxial Tensile Tester) (Figure 3.5) with a load capacity of 500 N, and pulled at a rate of 3.5 mm/min (Grip separation: 3.5 cm). The uniaxial tensile test was coupled with polarized light microscopy (Aven 26700-209-PLR Mighty Scope) to detect birefringence during plastic deformation.

Hydration / Thickness	0.1% w/w	0.65% w/w	1.5% w/w
37 +/- 4.9	4 samples	4 samples	4 samples
51 +/- 3.4	4 samples	4 samples	4 samples
66 +/- 2.7	4 samples	4 samples	4 samples
88 +/- 3.4	4 samples	4 samples	4 samples
107 +/- 7.9	4 samples	4 samples	4 samples

Table 3.1: Factorial design (3 x 5) for Uniaxial Tensile Test.

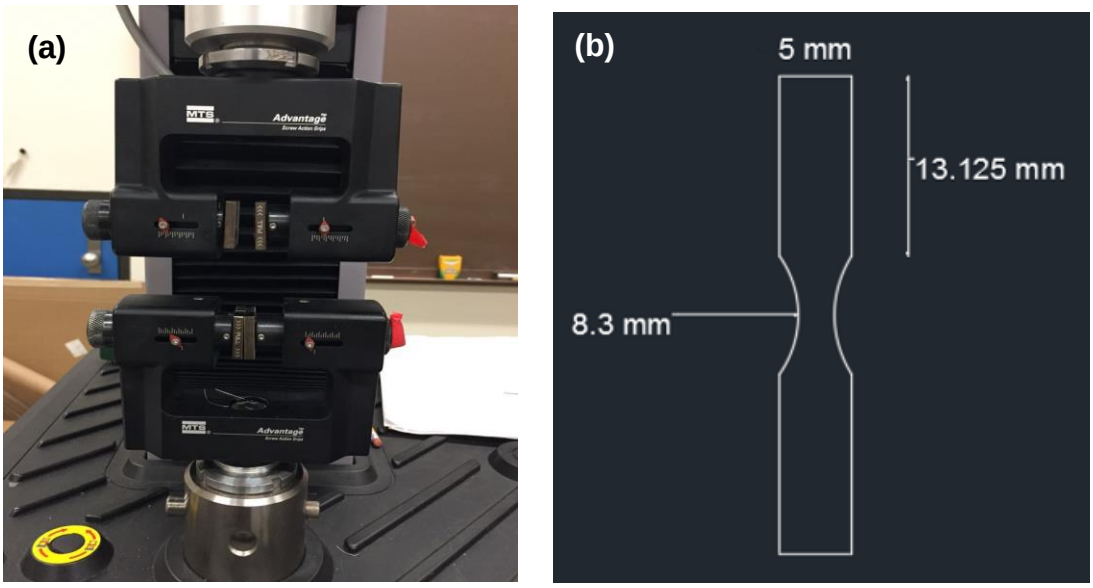

Figure 3.6: (a) Uniaxial tensile tester **(b)** Uniaxial tensile test specimen (AutoCAD 2016®)

3.3.2 Biaxial Tensile Test

Cruciform-shaped specimens were tested on a biaxial tensile test machine (Instron® 8848 MicroTester) (Figure 3.7). Each arm of the specimen was fixed to an aluminum serrated grip that was independently loaded by an electromechanical drive mounted on linear bearings. The load was controlled for each grip using a 500 N load cell. Load as a function of strain profiles were obtained in the two perpendicular directions and processed in the same way as uniaxial data to obtain the true stress versus strain profiles. The test was conducted in triplicate for two levels of thicknesses.

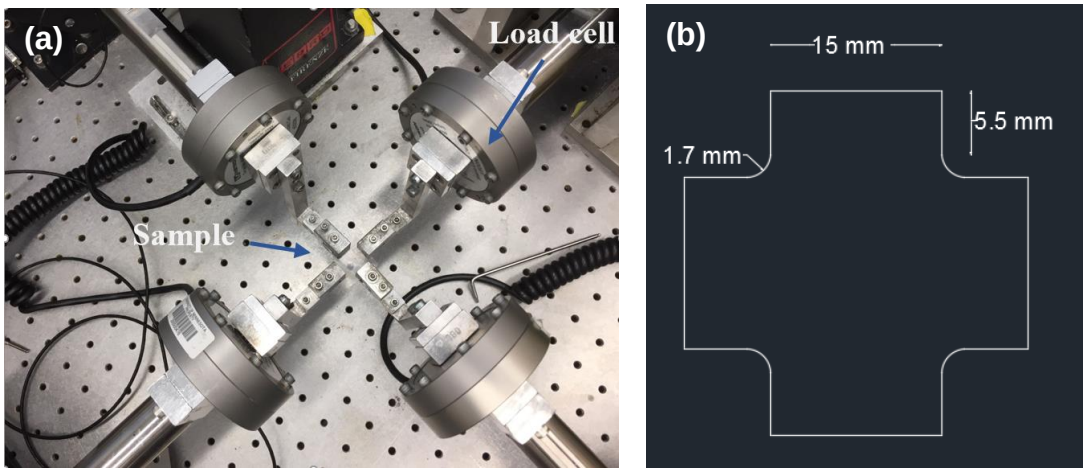

Figure 3.7: (a) Biaxial tensile tester **(b)** Biaxial tensile test specimen (AutoCAD 2016®)

3.3.3 Preparation and Characterization of Spherical PLGA capsules prepared for conducting "beach-ball" inflation test

A spherical PLGA capsule was prepared as per steps outlined below:

a. Preparation of mold with a spherical cavity: A polydimethylsiloxane (PDMS) mold containing a spherical cavity was prepared using the Sylgard® 184 Silicone Elastomer Kit as per the manufacturer's recommendations. Briefly, the pre-polymer base (Part A) and a cross-linking curing agent (Part B) were mixed thoroughly in 10:1 ratio and degassed in a vacuum desiccator for 30 minutes. A stainless-steel sphere (2.2 or 1.5 mm, radius) was placed in the degassed, uncured PDMS. The mixture was cured around the sphere at 125℃ for 20 minutes. The cured PDMS was split to release the sphere and rejoined again around the cavity using additional uncured PDMS. A mold with a spherical cavity was obtained when the PDMS seal was cured at 125℃ for 20 minutes.
b. Preparation of surfactant-containing ice spheres: The cavity was filled with 6 % w/v aqueous poly(vinylalcohol) (PVA) solution along with a food dye before inserting a stainless-steel syringe needle (Stainless-steel type: 304). The solution was gradually frozen to -20℃. PVA surfactant and food dye were added to allow homogeneous spreading of PLGA coating solution around the sacrificial ice spheres and to detect leaks, respectively.
c. Dip-coating in 12% w/w PLGA in DCM: The surfactant-ice sphere-syringe needle assembly was loaded onto a syringe connected to a rotor. The sphere, along with a part of the syringe needle immediately next to the sphere, was

dip-coated over one spin with 12% w/v PLGA in DCM solution. The speed of rotation determined the thickness of the capsule shell (Table 3.2). The shell was found to be complete and transparent in appearance when the coating process was conducted under low relative humidity conditions (< 15%).

d. Drying: DCM solvent was allowed to evaporate from the shell at room conditions, first, over a period of 24 hours while maintaining a constant level of water above the shell to prevent its shrinking when the T_g of PLGA was lowered below room temperature in the presence of DCM, then, over a period of 48 hours in the absence of water. Complete residual solvent removal (DCM and water) was carried out by step-wise increase in drying temperature from 35 to 55℃ under atmospheric pressure over a period of 4 days (as described previously in Section 2.3.1). For the hydrostatic/burst pressure determination test, the capsule attached to the stainless-steel syringe needle was used as formed (Figure 3.8).

Speed of rotation (rpm)	**Thickness of membrane (μm)**
67	50
31	100

Table 3.2: Relationship between speed of spinning during dip coating and thickness of the coat

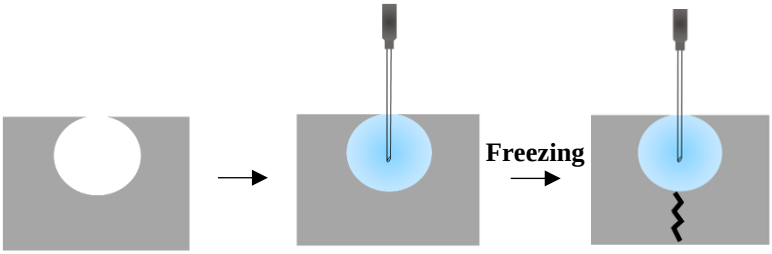

(a) Preparation of mold with a spherical cavity

(b) Preparation of surfactant-containing ice spheres

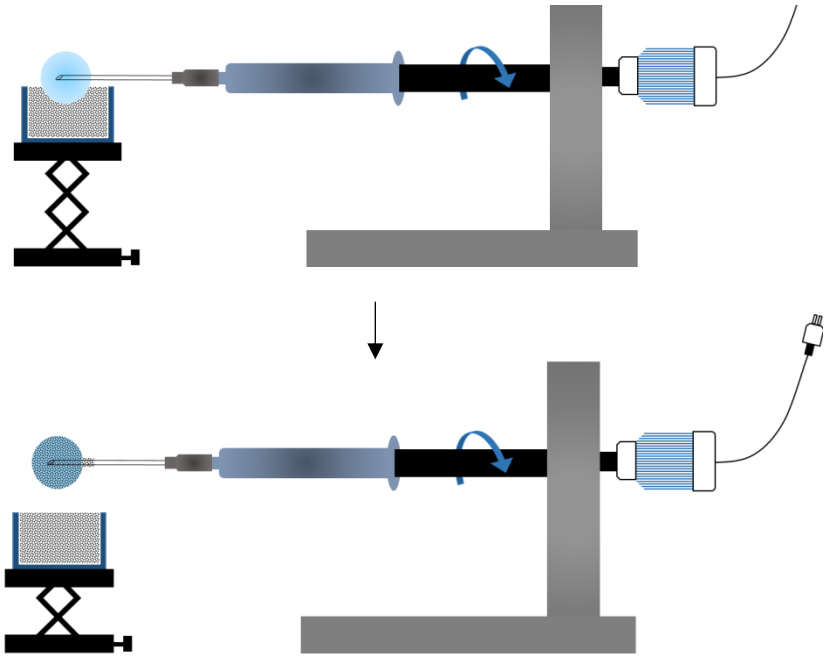

(c) Dip-coating in 12% w/v PLGA in DCM

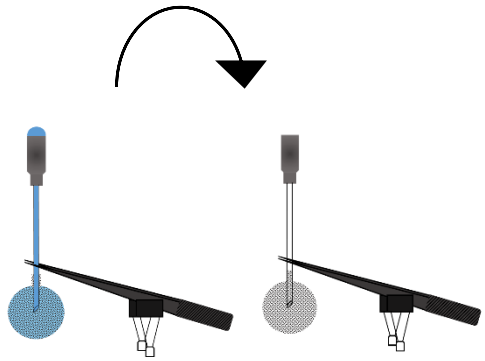

(d) Drying

Figure 3.8: Schematic representation of the PLGA capsules preparation process.

To determine the uniformity of shell thickness from top to bottom (relative to the seal) and laterally, as well its repeatability, four different capsule shells were sliced equatorially using a cryotome (Leica CM 1900, GMI, MN, USA) along four different axes, and imaged under a high-resolution stereomicroscope (Hirox 3040Z, NJ, USA) (Figure 3.9). Measurements along each axis per capsule size and thickness (2.2 mm and 1.5 mm capsule radii, 100 μm and 50 μm capsule shell thickness) were carried out in duplicate.

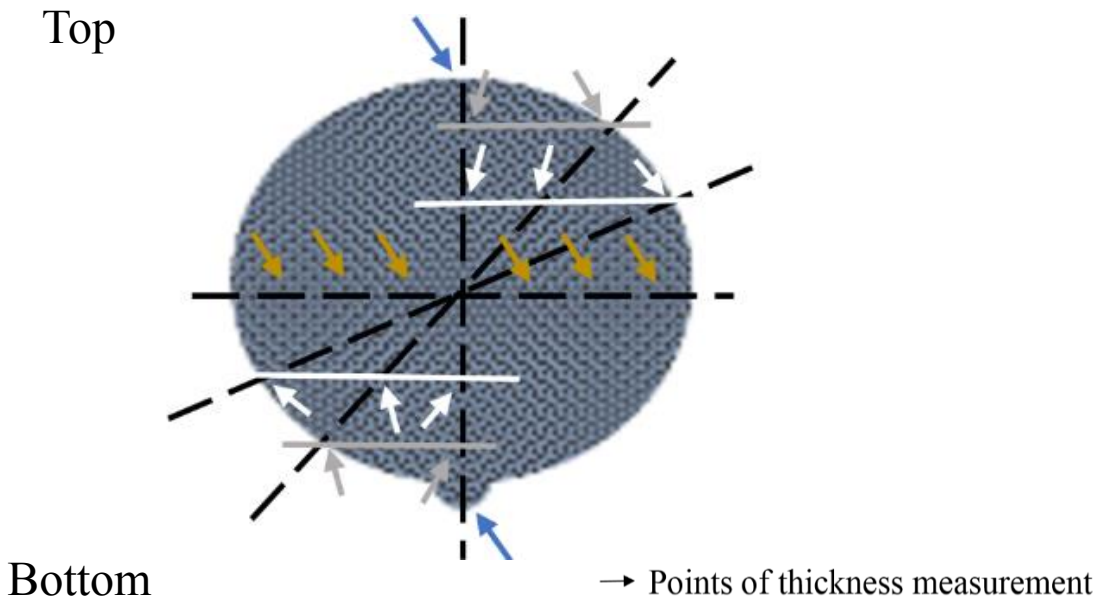

Figure 3.9: Uniformity of thickness determined at different cut angels

3.3.4 The "beach-ball" inflation technique (Hydrostatic/Burst Pressure Determination)

Burst pressure was determined under room conditions using a home-made fixture consisting of a 1-ml syringe to which the syringe needle with capsule and a digital pressure gauge were attached via a Y-connector (Figure 3.10). The water flow rate into the capsule was controlled at 20 µL/min by a syringe pump (NE-500 Programmable OEM Syringe Pump, PumpSystems Inc). The pressure developed within the capsule corresponds to the hydrostatic pressure and was recorded as a function of capsule's radial extension until capsule rupture. The test was conducted in duplicate for shells with two thickness levels (50 µm and 100 µm), two levels of radii (1.5 mm and 2.2 mm) and two levels of hydration (0.01% w/w and 0.65% w/w).

The friction due to the plunger and syringe needle as well as compliance of the system were found to be negligible as determined from a test without the capsule.

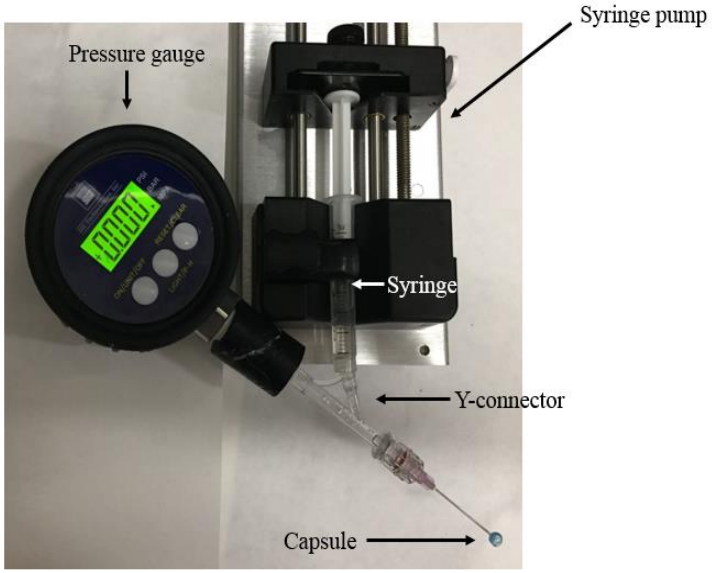

Figure 3.10: Set-up for the "beach-ball" inflation technique

3.3.5 Statistical Analysis

Statistical Analysis was performed using R Statistical Software (version 3.3.2; R Foundation for Statistical Computing, Vienna, Austria). Sample size for the uniaxial tensile test was determined to obtain a statistical power of 0.92. ANOVA was performed to determine differences in mechanical properties due to the various treatments (that is, hydration and thickness levels of films and capsule shells and radii of shells), and pairs were compared using post-hoc Tukey's multi-comparison test. Non-linear regression analysis was conducted to obtain a model for uniaxial tensile test responses as a function of film hydration and thickness levels. The results of the non-linear regression model were used as inputs for the elastoplastic model. A value of $p < 0.05$ was considered statistically significant. It should be noted here that the data analysis and conclusions from the trend lines and correlations drawn in this study may be valid only for the range of variables tested here.

3.4. Results and Discussion

3.4.1 Uniaxial Tensile Test

3.4.1.1 General mechanical behavior of PLGA

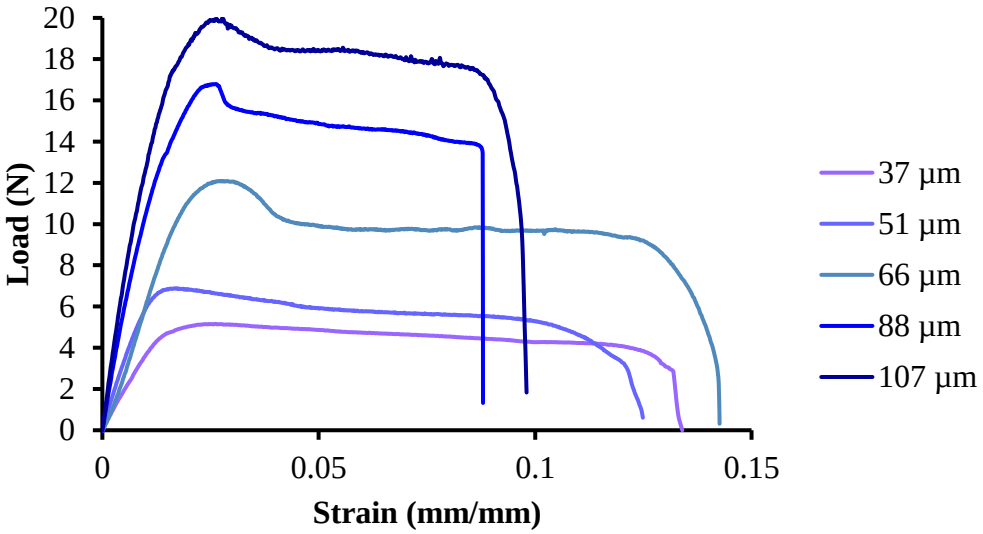

Figure 3.11: Load-vs-strain curves of variously thick specimens

The raw data recorded by the Uniaxial Tensile Tester is given as load versus strain curves for PLGA specimens of varying thicknesses (Figure 3.11). The load increases linearly with strain during elastic deformation. Beyond approximately 2% strain, PLGA yields and the load to be applied to produce higher deformations achieves more or less a constant value. The load required to strain a specimen to a critical value of approximately 10% is lower for thinner specimens. However, when the load was normalized by the area of the specimen (Eq. 3.1), true stress versus strain curves were obtained as shown in Figure 3.12.

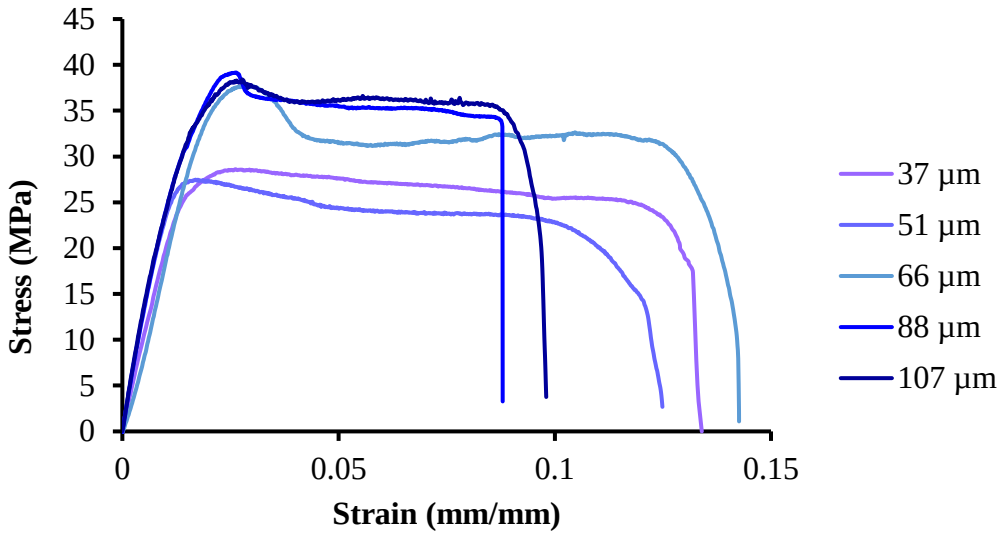

Figure 3.12: Stress vs strain curves of variously thick specimens

Polarized light microscopy was used to distinguish between the elastic and plastic regimes (Figure 3.13)

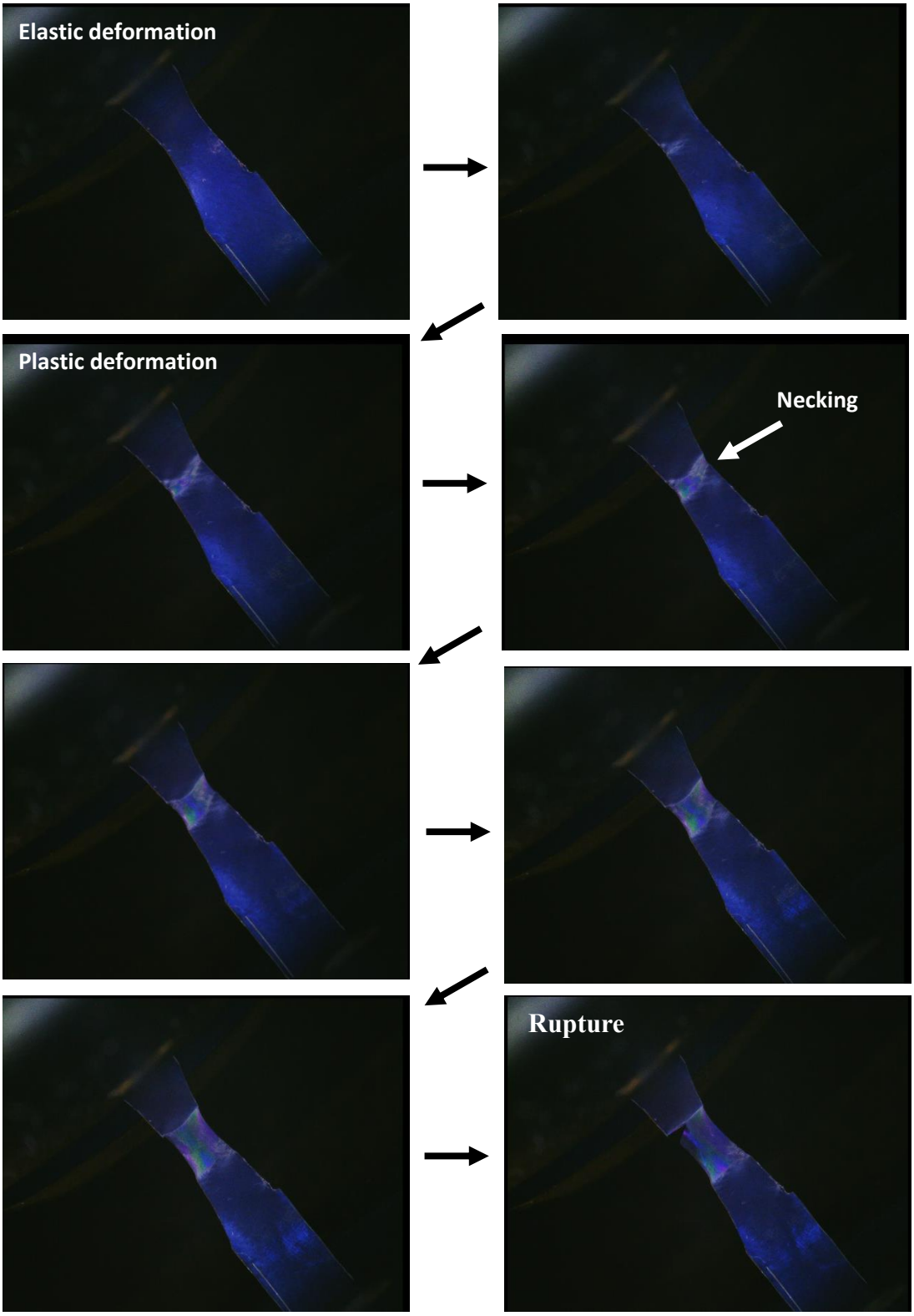

Figure 3.13: Various stages of stretch and elastoplastic deformation of specimen under uniaxial tensile test

Birefringence during plastic deformation serves as a prelude to understanding the phenomena occurring at the macroscopic level which is typical of glassy polymers. The elastoplastic extension of PLGA in response to a uniaxial load can be explained by considering the structure of PLGA.

PLGA Structure-Property Relationship

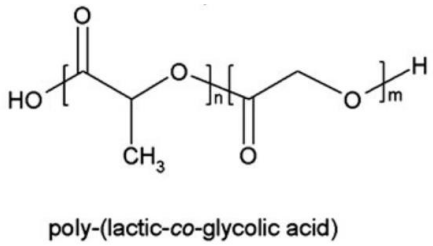

Figure 3.14: Chemical structure of PLGA.

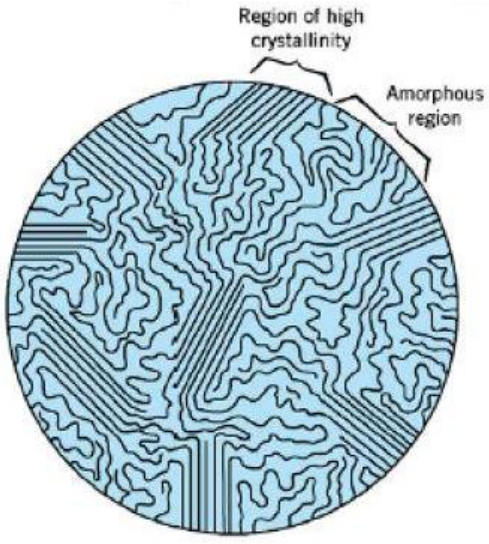

Figure 3.15: Fringed-micelle model.[37]

85/15 PLGA used in this study is a semi-crystalline polymer. Research in semi-crystalline polymers has given rise to many models of polymer structure, such as the fringed micelle fibrillar model, the folded chain model, the switch board model and the microfibrillar model, to name a few.[36-40] One of the most widely applicable and developed model, the fringed micelle concept of Hermann, Gerngross, and Abitz, is applicable to the initial, isotropic structure of solution-cast PLGA used in this study (Figure 3.15).[36] This model assumes a random arrangement of long linear macromolecules which, in regions of sufficient chain alignment, are able to form crystal lamellae 100-500 Å in thickness. In most semi-crystalline polymers, electron microscopy studies have shown that isotropic spherical aggregates of crystalline lamellae called spherulites, are present.[41-42] Since the molecular chains are tens or hundred times the length required for single passage through a lamella, these either, fold-over outside the lamella to form 'chain folds' and re-enter the same lamella at a location adjacent to the preceding passage or transverse more than one lamella to form interconnecting 'tie-chains'.[33-42] This can be visualized as the polymer molecule being regularly folded like woof on a fabric. Successive sequences in a given layer of the crystal lamella are thus, contributed by a plurality of molecules. In addition, a comparatively large domain by a PLGA molecular chain is shared with hundreds or more other molecules similarly configured in random coils. As a result of crowding, the chains can be expected to be extensively intertwined or 'entangled'.[43-46] These entanglements, tie-chains, folded chains, and hydrophilic terminal chain ends of hydroxyl and carboxylic acid groups are largely excluded from the crystalline lamellae and comprise the amorphous, disordered domain (Figure 3.15).[33] The fringe micelle model used to elucidate PLGA molecular

structure has been corroborated by Zong et al. who used wide-angle and small-angle X-ray diffraction to determine the crystal structure and morphology of PLGA.[19]

Tie chains, folded chains, entanglements and cilia link adjacent crystallites, regulate strain transmission to the crystallites and contribute, in general, to the global mechanical behavior during elastoplastic deformation of the polymer.[43] In an earlier study, it was determined quantitively in a similar semi-crystalline polymer that the initial elasto-plastic deformation was governed by the amorphous phase properties until at relatively higher strains when crystallites start to undergo shear deformations.[47]

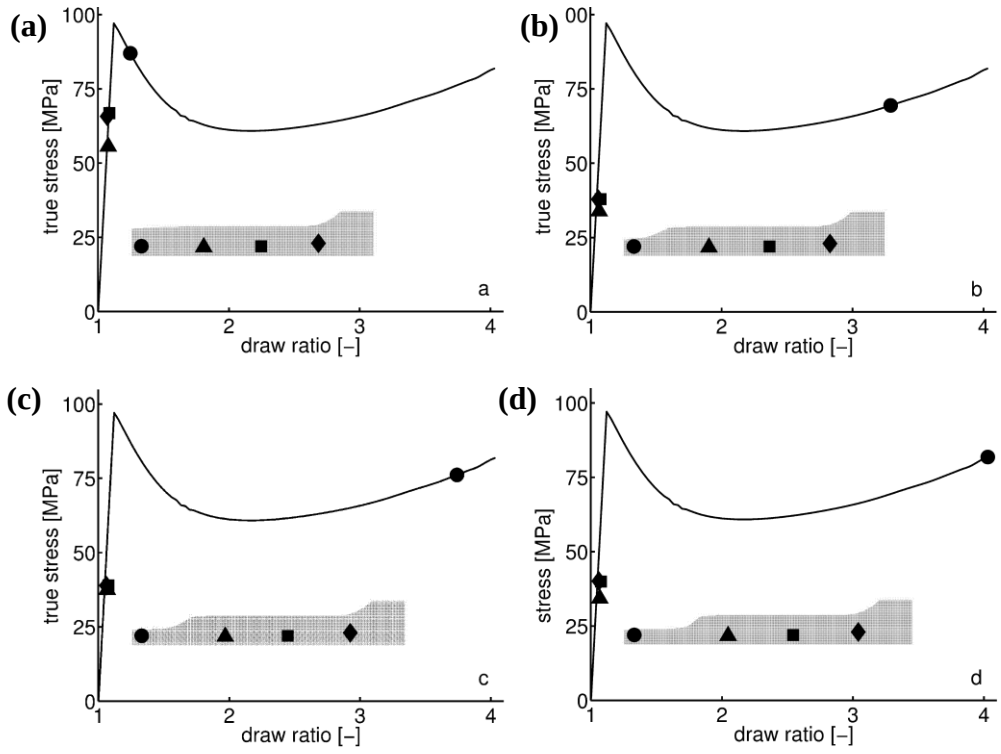

Figure 3.16: Schematic representation of elasto-plastic deformation of PLGA subjected to uniaxial stretching.[26]

Figure 3.16 shows diagrammatically the main characteristics of the stress-strain curve of a dumb-bell shaped PLGA specimen and its accompanying macroscopic deformation behavior.[48] The following is a summary of the underlying molecular mechanisms which may, speculatively, be underlying the macromolecular deformation behavior of 85/15 PLGA.[33-49]

1. **Elastic deformation**

   Macroscopic behavior[48]: When a gradually increasing load is applied, the specimen first deforms homogeneously and elastically throughout its length and regains its original dimensions if the load is removed. During the initial elastic stage, stress rises throughout the specimen. Until the yield point is reached, the stress is approximately equal in all the marked positions (Figure 3.16). The stress at which the strain ceases to be proportional to the applied stress is known as the proportionality limit. The elastic range generally extends beyond the proportionality limit, and the stress at which an appreciable permanent deformation is observed is known as the yield stress. PLGA polymer specimen used here is initially isotropic and its isotropy is preserved during elastic deformation.

   Microscopic behavior: Chain sequences in amorphous regions have their ends more-or-less fixed either by existing entanglements or by anchoring in adjacent crystallites (Figure 3.15). These chain sequences are stretched during the deformation process. The reversibility of elastic deformation or strain recovery can be attributed to the retractile forces originating from these chain sequences in the amorphous region.[47] Moreover, two types of resistances act against shear

displacement of polymeric chains during elastic deformation viz. surface friction of lamellae and resistance to chain unfolding.[38-40] These resistances may arise due to macromolecular interactions, which are implicit in a PLGA specimen that is, hydrogen bonds and other van der Waals interactions. At this stage, the crystallites are still randomly oriented.

2. **Plastic deformation: Strain Softening**

Macroscopic behavior[48]: In a uniaxial tensile test, the limit of elastic deformation is followed by localized deformation through 'necking'. Yield and subsequent plastic deformation occur underneath a defect (circle) (Figure 3.16a). The strain is localized in this zone, accompanied by a local drop in stress, a phenomenon known as strain softening. Both these events of strain localization and strain softening cause the stress to drop in the elastically deformed region and the other three markers descend along the elastic curve. In other words, the tensile test becomes unstable when the load reaches its maximum and the specimen 'necks' locally while the remainder of the specimen recovers elastically under the decreasing load. Due to strain softening, a progressively smaller increment of stress is needed to produce a given increment of strain. Thus, the stress-strain curve progressively bends, and the slope becomes increasingly negative. This marks the beginning of plastic deformation. The material is permanently deformed and fails to return to its original shape, even when the deforming force is removed. Moreover, at this point, the polymer specimen develops anisotropy.

Microscopic behavior: Intermolecular slipping sets in when the uniaxial stress applied increases to an extent that chain unfolding and frictional lamellar resistances are overcome. Slip processes comprise of a simple shear followed by a rotation of the shearing direction towards the axis of load application.[47] In the crystalline domains, the packing of lamellae becomes increasingly dense with uniaxial stretching, and the crystallites begin to orient in the direction of load. The dense packing of lamellae severely limits the possibility of deformation. Therefore, it is relatively easy to displace the lamellae axially, so that is the main mode of deformation.[39] Intra- and inter-lamellar shearing occurs, which is followed by the disintegration of lamellae. This process results in a partial loss of initial crystallinity or 'melting'.[47] On the other hand, in the amorphous domains, progressive slippage of the polymer chains at the entanglement points results in a redistribution of the internal stresses in the specimen.[47] These processes of orientation of chain folded lamellae, fragmentation of crystalline domains, and slippage of the polymer chains at the entanglement points are associated with a drop in the stress level, or strain softening, in the deformed neck.

Furthermore upon yielding, as a consequence of the 'slip' process, the crystallites rotate during straining, so that they approach some limiting orientation (not necessarily parallel to the direction of applied load, because of mutual constraints between the polymer chains).[49] By this mechanism, the initial isotropic, randomly oriented chains of PLGA become anisotropic during plastic deformation.

3. **Plastic deformation: Strain Hardening**

Macroscopic behavior[48]: With continual deformation, following strain softening, the stress in the deformed neck begins to increase again, a phenomenon known as strain hardening. In this case however, strain hardening is not as significant as strain softening. The pronounced strain softening compared to insufficient strain hardening causes further localization of the strain. As a result, the stress drops further and hardly rises again at large strains (Figures 3.16b and 3.16c). The deformation keeps on localizing until the tensile strength in the deformed region is exceeded, resulting in rupture (Figure 3.16d).

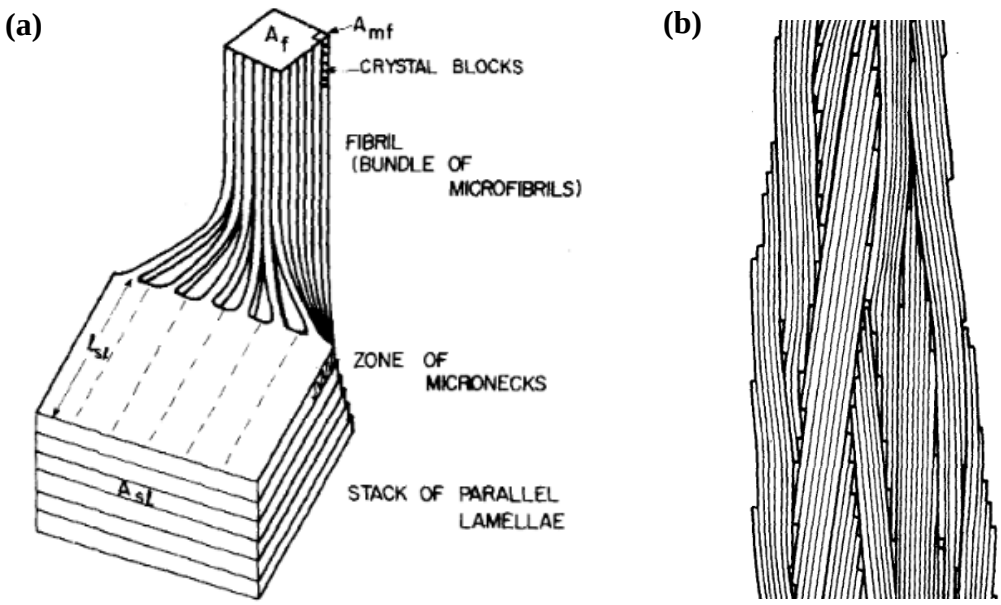

Figure 3.17: (a) Transformation of a stack of parallel lamellae in a micronecking zone into a bundle of densely packed microfibrils **(b)** Microfibrillar model of a polymer.[38-40]

Microscopic behavior: Melting of crystallites during the strain softening regime is often followed by recrystallization of a different array of sequences in a pattern compliant with the prevailing stress.[48] Polymer chains start to rearrange from spherulite lamellae into long, ellipsoidal microfibrils with lateral dimensions between 100-200 Å and a length on the order of tens of microns (Figure 3.17a).[49] Thus, the microfibrillar model proposed by A. Peterlin can be used to explain the anisotropic, plastic behavior of PLGA at higher strains.[38-40] The microfibrils consist of alternating crystalline and amorphous regions. The amorphous regions comprised of a great many taut tie chains, originating from tie chains which were originally connecting adjacent lamellae and bridge the amorphous regions to connect the crystalline blocks. On the other hand, the folded chains in stacked, randomly oriented lamellae undergo partial unfolding and orientation during strain softening into densely packed bundles of microfibrils called fibrils (Figure 3.17).[48]

With additional stretching, the fibrils may be sheared and axially displaced. The shearing of the fibrils displaces the microfibrils in the fiber direction and extends the tie molecules by chain unfolding, increasing the surface area of the fibrils, thereby increasing the resistance to further elongation.[39] However, shearing displacement in the load direction decreases the number of fibrils per cross-section; axial extension proceeds at a faster rate than the increase in the surface area of fibril.[39] Thus, increase in stress at higher strains or strain hardening must be caused by other sources of resistance. There are infact two potential sources of resistance to further deformation in typical semi-crystalline polymers:

a. Crystalline region: With stretching, the microfibril density in the deformed region increases. This in-turn, increases the surface friction of microfibrils for sliding motion, thus requiring higher stress application to cause shearing displacement.[39]

b. Amorphous region: Resistance can also be contributed by the ends of microfibrils located in the boundary between the fibrils. The more or less irregular end blocks with occasional molecular connections with adjacent fibrils may permit some chain unfolding during the sliding motion so that the chains are slowly pulled out of these blocks and are accomodated in the boundary layer. This smooths and eventually eliminates the irregularity introduced by each end of the microfibril. Beyond that, the unfolded chains act as new connectors of the blocks of adjacent fibrils over their fully extended length. As a consequence of better contact between the adjacent fibrils, the viscous resistance is gradually increased so much so that it over-compensates for the effect of reduced number of fibrils per cross-section and yields the observed increase in stretching stress with elongation (Figure 3.18).[39]

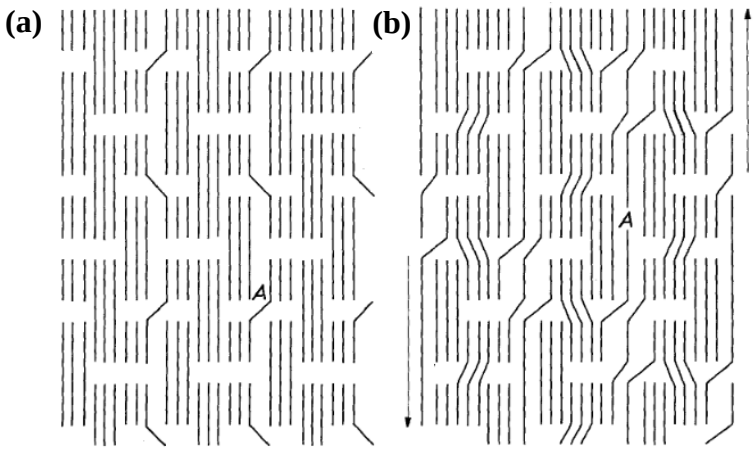

Figure 3.18: Extension of interfibrillar tie molecules by chain unfolding during shearing displacement of adjacent microfibrils. The molecule A passes one amorphous layer before and 4 after deformations. One has (a) originally ½ interfibrillar tie molecule per amorphous layer and microfibril and ends (b) after deformation with 3/2 such molecules.[39]

However, in case of the PLGA polymer, we observe a pronounced strain softening compared to insufficient strain hardening. This can be attributed to a microfibril density and/or viscous resistance that under-compensates the slip process and/or reduced number of fibrils per cross-section, respectively.

Tensile straining at 90^{o} to the fiber axis ultimately leads to fracture of the completely fibrous material by crack propagation along the boundaries of fibrils which tends to be perpendicular to the applied stress.

NOTE: Plastic deformation or rupture cannot be explained by rupture of covalent bonds as the deformation was not accompanied with a decrease in the polymer molecular weight in numerous studies conducted previously.[48]

3.4.1.2 Effect of state of hydration on PLGA mechanical properties

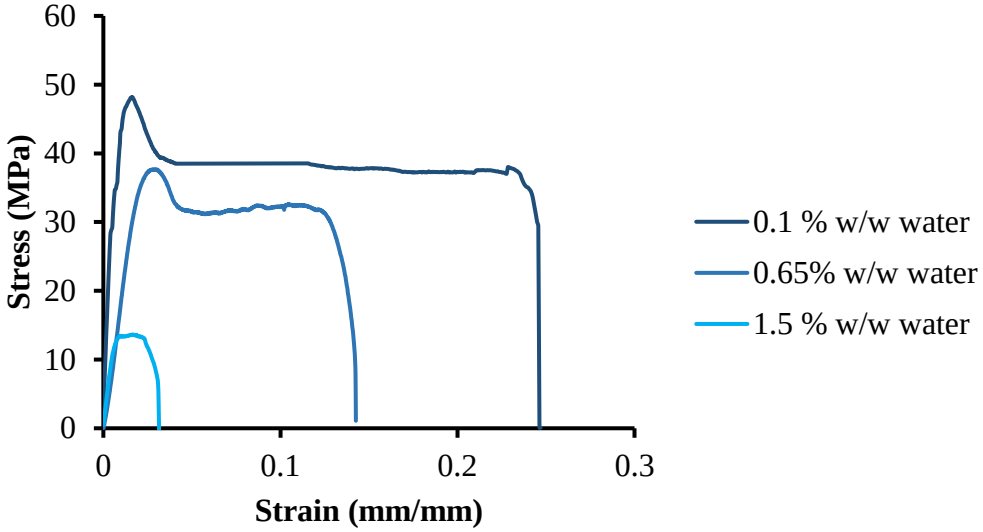

Figure 3.19: True stress vs strain curves of specimens at three levels of hydration.

Figure 3.19 depicts a trend in true stress versus strain of PLGA at three levels of hydration. There are decreases in the elongation at break, stress at yield and elastic modulus with increasing moisture content in PLGA specimens. Figure 3.20 (a-g) is a summary of how various tensile properties change as a function of hydration, but not significantly with thickness, except for peak load.

(a)

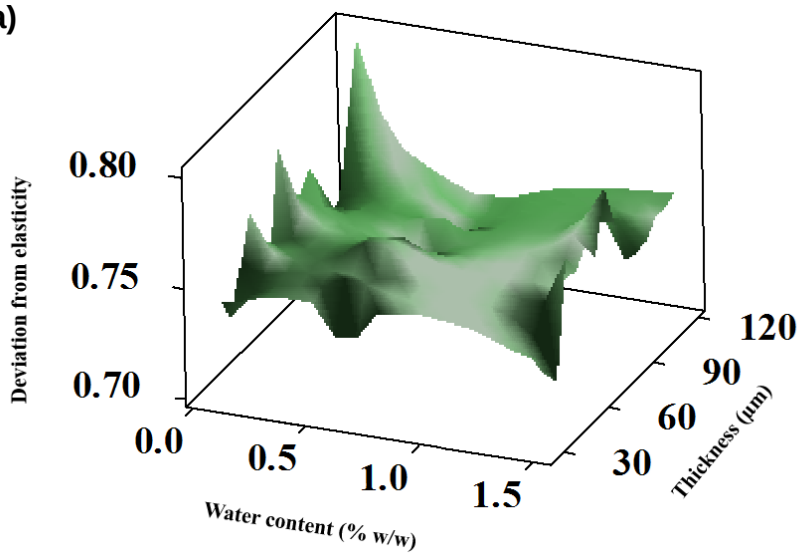
Deviation from elasticity
0.80
0.75
0.70
0.0
0.5
1.0
1.5
Water content (% w/w)
30
60
90
120
Thickness (µm)

(b)

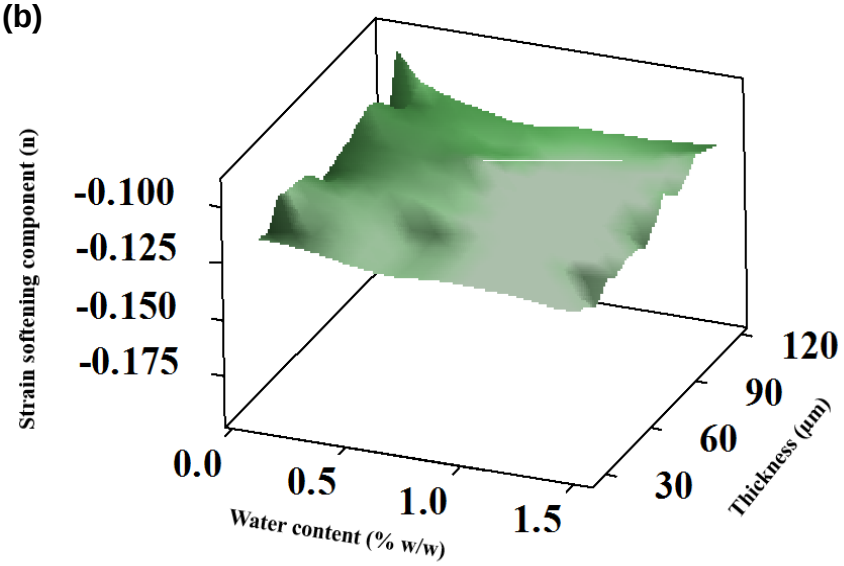
Strain softening component (n)
-0.100
-0.125
-0.150
-0.175
0.0
0.5
1.0
1.5
Water content (% w/w)
30
60
90
120
Thickness (µm)

(c)

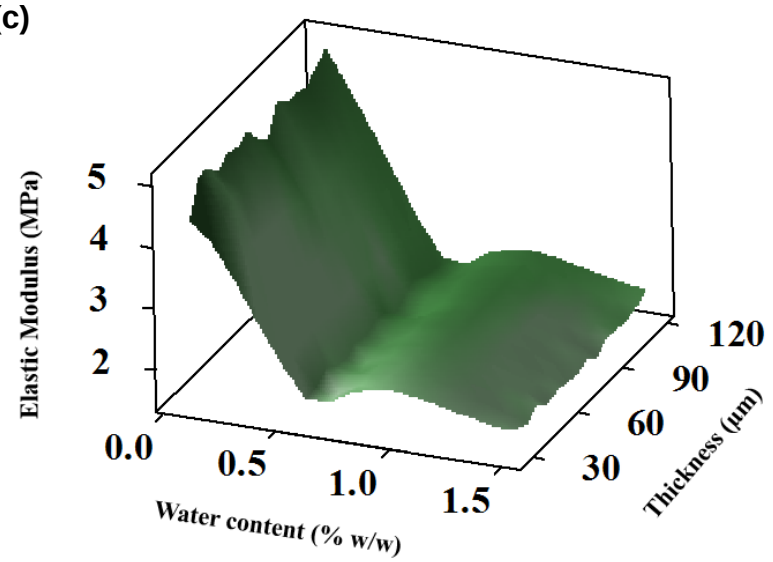
Elastic Modulus (MPa)
5
4
3
2
0.0
0.5
1.0
1.5
Water content (% w/w)
30
60
90
120
Thickness (µm)

(d)

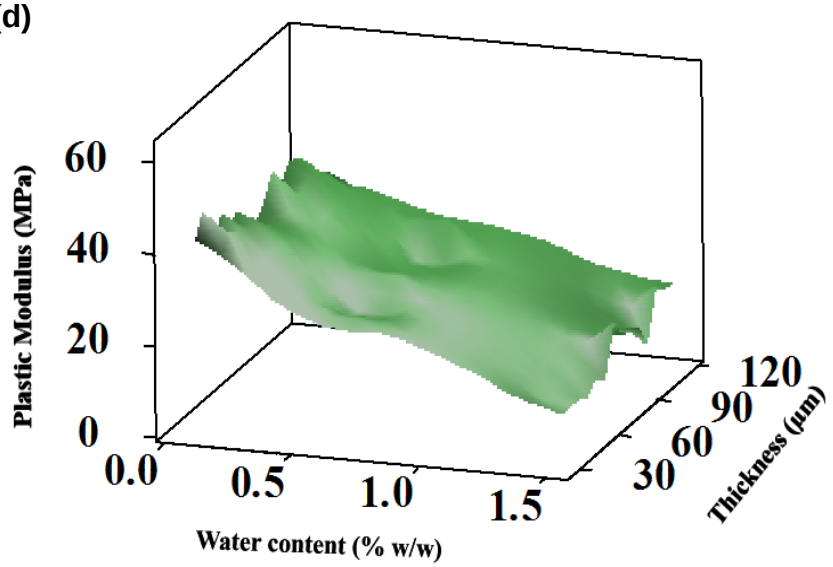
Plastic Modulus (MPa)
60
40
20
0
0.0
0.5
1.0
1.5
Water content (% w/w)
30
60
90
120
Thickness (µm)

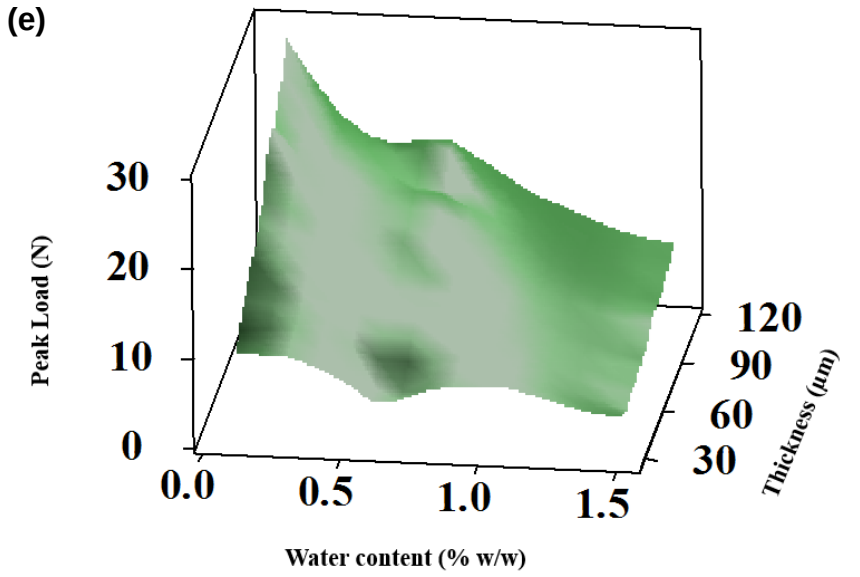
(e)
Peak Load (N)
30
20
10
0
0.0
0.5
1.0
1.5
Water content (% w/w)
120
90
60
30
Thickness (µm)

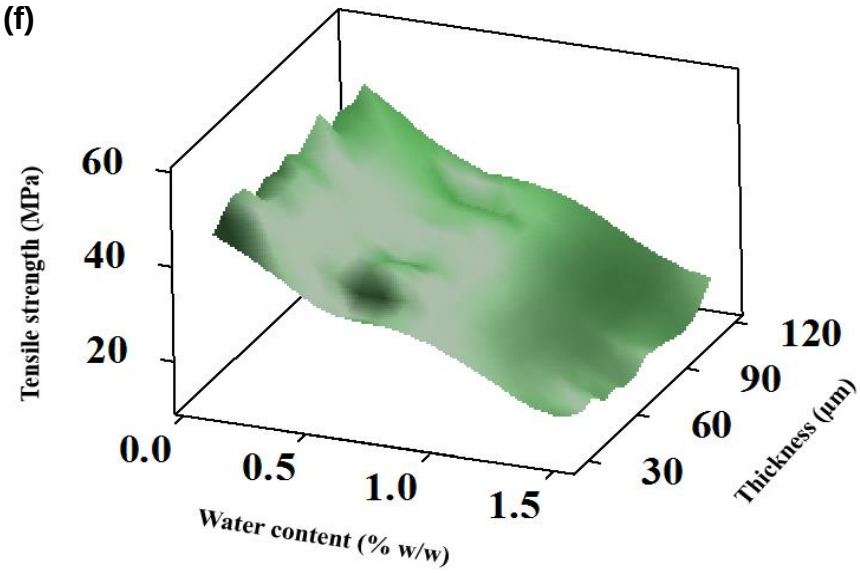
(f)
Tensile strength (MPa)
60
40
20
0.0
0.5
1.0
1.5
Water content (% w/w)
120
90
60
30
Thickness (µm)

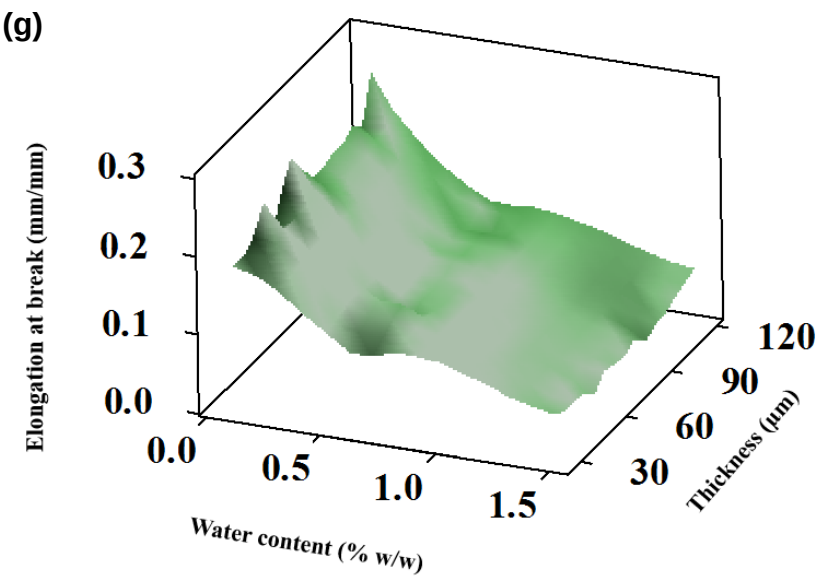

Figure 3.20: (a)-(g) Change in various mechanical properties as a function of PLGA hydration level and film thickness

The change in mechanical properties can be attributed to changes in the crystal structure with hydration and degradation.[19,26,50]

1. Hydration (0.65% w/w water)

   At this level of water uptake, as indicated in a previous pH monitoring study (*see* Section 2.3.2), polymer degradation is not significant. The change in the tensile properties of the polymer is due to hydration.

   The characteristically disordered chain sequences and the hydrophilic chain terminals in the amorphous region between the spherulites allow relatively rapid diffusion of water.[19] Water plays the role of a plasticizer and increases the mobility of the amorphous tie chains. The degree of entanglements and folds may also reduce by increased mobility and subsequent 'loosening' of the chains (Figure 3.21).[19] This loose chain packing in the glassy region was evident by lower T_g of the hydrated sample than the dry polymer (*see* Section 2.3.2).

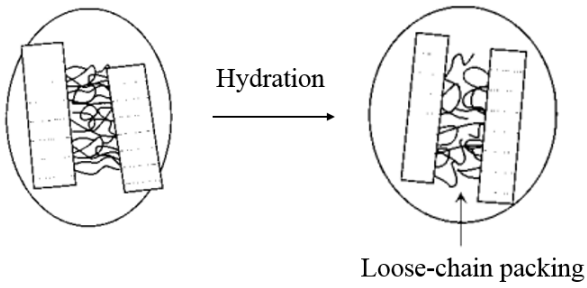

Figure 3.21: 'Loosening' of chains with hydration (*modified from* Ref. 19).

A higher fraction of taut tie chains and entanglements in the dry polymer results in a lower concentration of stress on the crystalline lamellae.[46] Thus, the stress to initiate plastic deformation in the crystalline phase, or in other words the yield

stress, is higher in case of a dry polymer while, the opposite is true for a hydrated polymer.[46] For analogous reasons, the stiffness of the polymer declines as well. Thus, the elastic and plastic moduli also decrease with decreasing number of tie chains and entanglements.

Finally, water molecules may potentially displace the hydrogen bonds existing between the chain sequences. The new hydrogen bonds formed between polymer chain sequences via water may be weaker than the displaced bonds. This may attribute to the breakage seen at low degrees of strain in case of hydrated specimens (Figure 3.22).

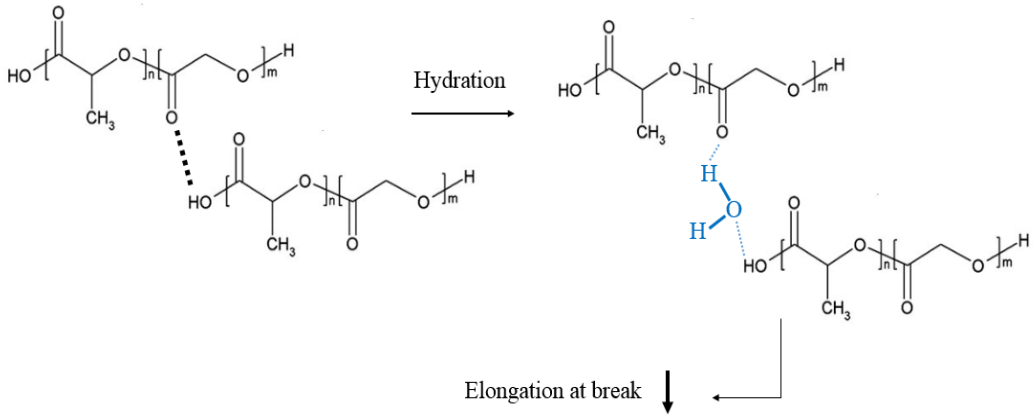

Figure 3.22: Possible decrease in the strength of hydrogen bonding interaction between chain sequences with hydration.

2. Degradation (1.5% w/w water) [19,26,50]

As mentioned above, as water preferably diffuses into the amorphous regions first, hydrolytic chain scission occurs first in the tie chains, entanglements and chain folds, reducing their density while simultaneously increasing the density of the hydrophilic terminal chain ends. This will cause more 'loose chain packing'.

Furthermore, the increased density of carboxylic acid end group accelerates the hydration and degradation processes. These processes result in a net reduction in tensile stress and elongation at break. In addition, mobility of the chains increases further, enhancing crystallization. However, higher crystallite formation may have offset a significant reduction in elastic modulus of the degraded specimen caused by the former processes.

There are, however, certain properties which remain unaltered at the given state of hydration and/or degradation.

1. Deviation from elasticity

   During the so-called elastic deformation, with deformation, PLGA polymer increasingly deviates from the perfect state of elasticity. This is apparent when the first derivative of stress with respect to strain is plotted as a function of strain (Figure 3.23).

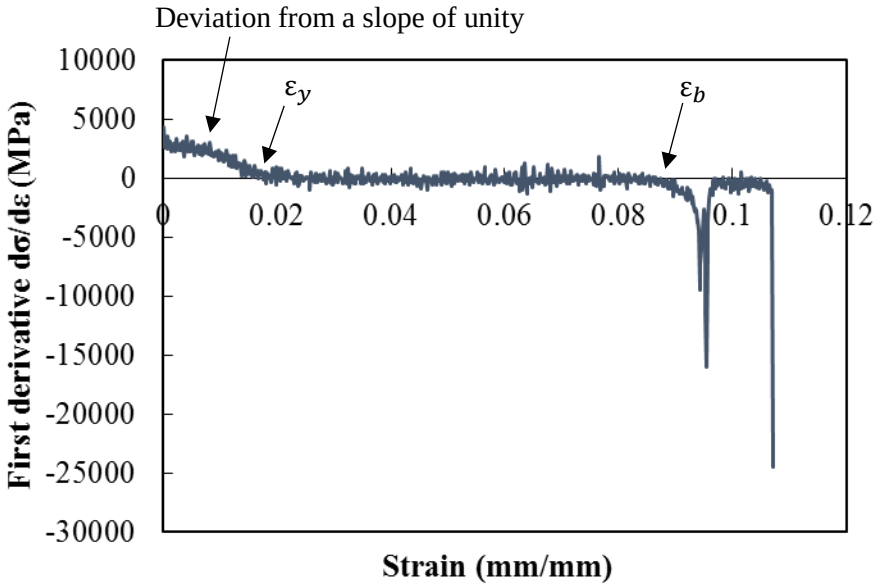

Figure 3.23: First derivative curve of stress with respect to strain versus strain

This deviation can be quantified by re-writing Hooke's law in the logarithmic scale as

$$\log \sigma = \log E + \log \varepsilon$$

Plotting $\log(\sigma)$ vs $\log(\varepsilon)$ for the elastic regime allowed quantification of deviation from elasticity from the slope (Figure 3.24).

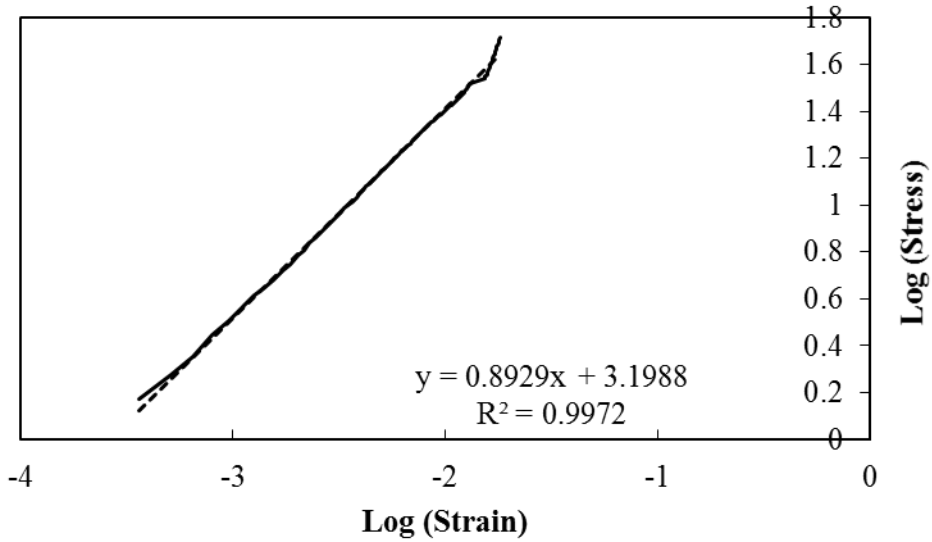

Figure 3.24: Stress-vs-strain on the logarithmic scale for elastic regime

This deviation from elasticity may be attributed to existence of certain chain folds in the amorphous region very close to their terminals which are embedded in the crystalline lamellae. These chain folds may be relatively less resistant to kinking and subsequent shear deformation. Since this feature simply arises due to a statistical distribution of various chain features, deviation from elasticity does not change with a change in hydration.

2. Strain softening component

The strain softening component was determined by re-writing Holloman's law in the logarithmic scale as,

$$\log(\sigma) = \log G + n\log(\varepsilon)$$

Plotting $\log(\sigma)$ vs $\log(\varepsilon)$ for the plastic regime allowed determination of strain softening component from the slope (Figure 3.25).

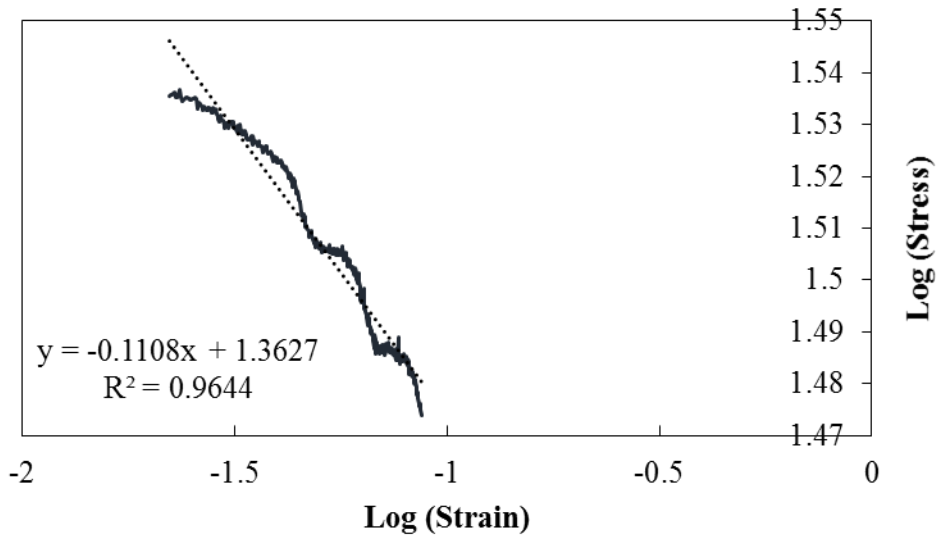

Figure 3.25 Stress-vs-strain on the logarithmic scale for plastic regime

The strain softening component was determined as an average slope of the plastic regime. The magnitude of the component did not change with hydration.

Based on the statistical analysis of the above results, the average properties of the PLGA film at two levels of hydration – 0.01% w/w and 0.65% w/w water content are tabulated below (Table 3.3).

Properties	**0.01% w/w**	**0.65% w/w**
Tensile strength (MPa)	45.542 ± 6.291	25.261 ± 5.652
Elongation at yield (mm/mm)	0.011 ± 0.0048	0.024 ± 0.0081
Elongation at break (mm/mm)	0.241 ± 0.052	0.112 ± 0.024
Elastic modulus (GPa)	4.94 ± 0.21	1.57 ± 0.09
Plastic modulus (MPa)	48.859 ± 5.665	27.381 ± 5.328
Strain softening component	-0.112 ± 0.021	-0.125 ± 0.012

Table 3.3: Summary of tensile properties at two levels of hydration to be used in the model for elastoplastic expansion of a sphere

3.4.2 Biaxial Tensile Test

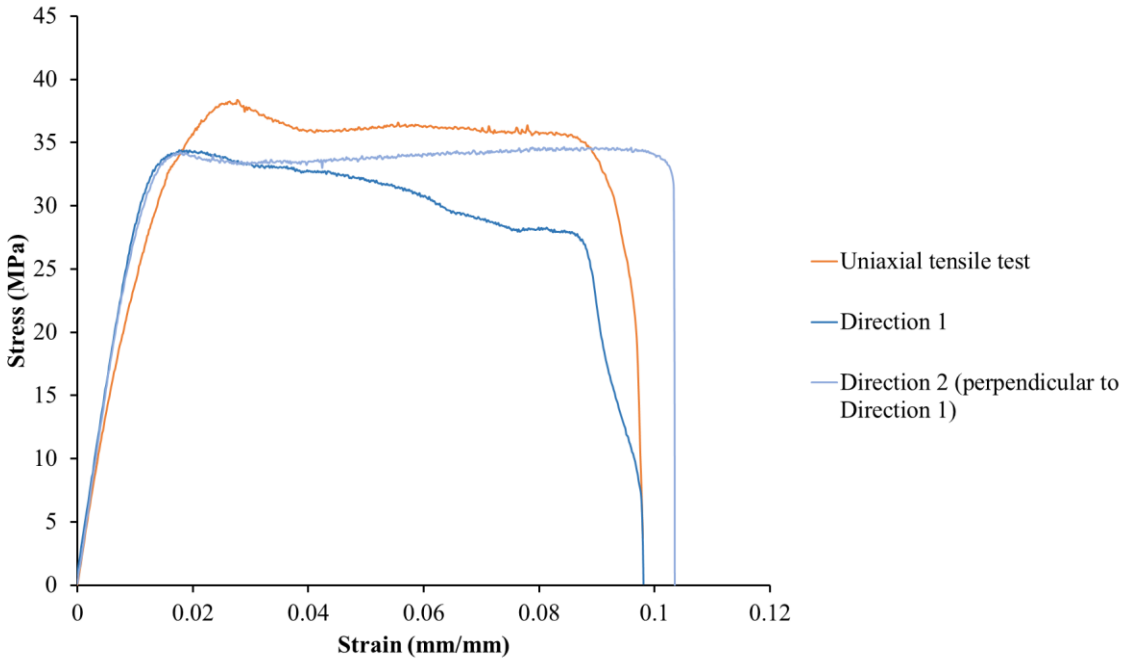

Figure 3.26: Comparison of biaxial true stress vs strain curves with the uniaxial curve

During the biaxial stretch, PLGA displays a mechanical behavior similar to the uniaxial stretch along both the axes (Figure 3.26). Film rupture occurred along the edge of two perpendicular arms of the cruciform, simultaneously. This indicates that each arm of the cruciform sample may be subject to only a uniaxial stretch rather than a true biaxial stretch.[51] The anisotropic behavior of a specimen element subjected to loads in two directions simultaneously may then remain undetermined. Moreover, when examining the expansion of a spherical capsule, each element of the membrane is in-fact subject to a triaxial load.

Thus, a triaxial “beach-ball” inflation technique serves as a promising method to determine the mechanical behavior of polymers, especially when they are anisotropic.

3.4.3 Novel “Beach Ball” Inflation Technique

3.4.3.1 Capsule characterization

Radius:

Figure 3.27 shows two capsules of two different radii – 1.5 mm and 2.2 mm.

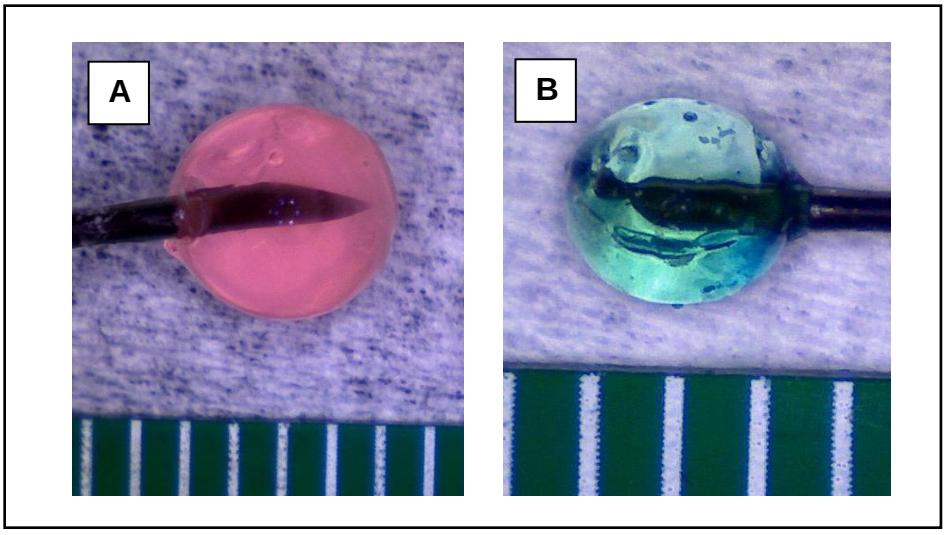

Figure 3.27: Two capsules of radii (A) 2.2 mm and (B) 1.5 mm (scale in mm)

Thickness:

The capsules were cryotomed randomly across 4 axes and imaged along the diameter (Figure 3.28). This provided a measure of thickness uniformity as well as repeatability of the coating process. Figure 3.29 shows capsules of two different thicknesses – 100 µm

and 50 µm. Thickness measurements made with an on-screen computer micrometer, revealed uniformly thick capsule shells.

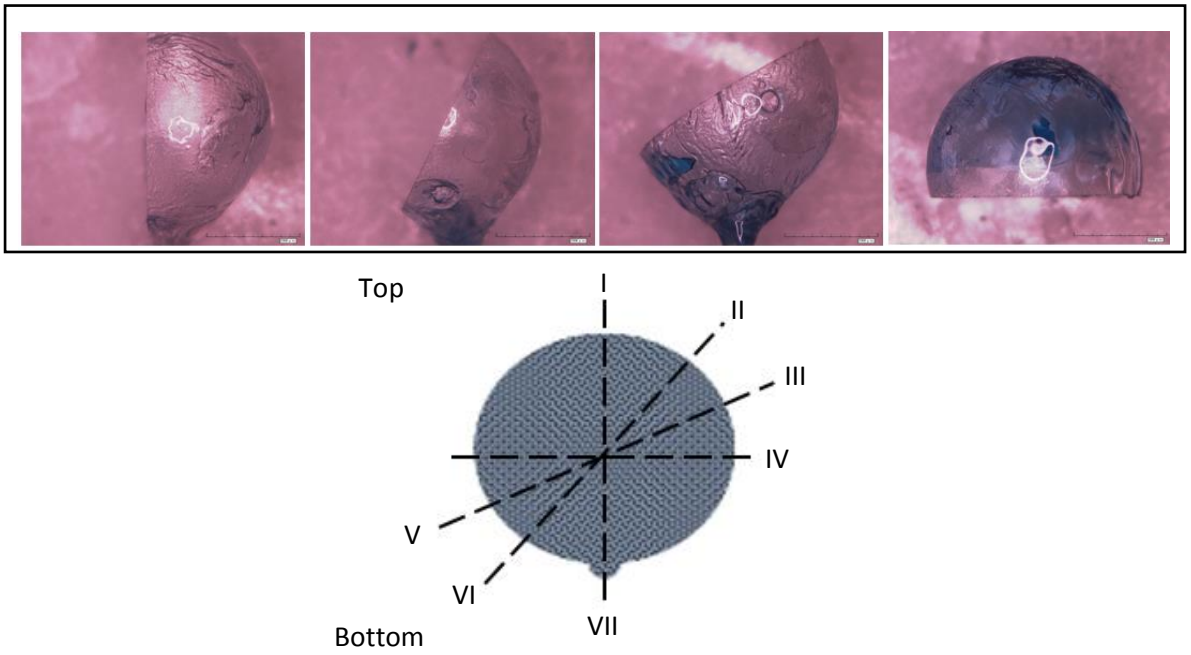

Figure 3.28: Micrographs of cryotomed shells along the four axes

(a)

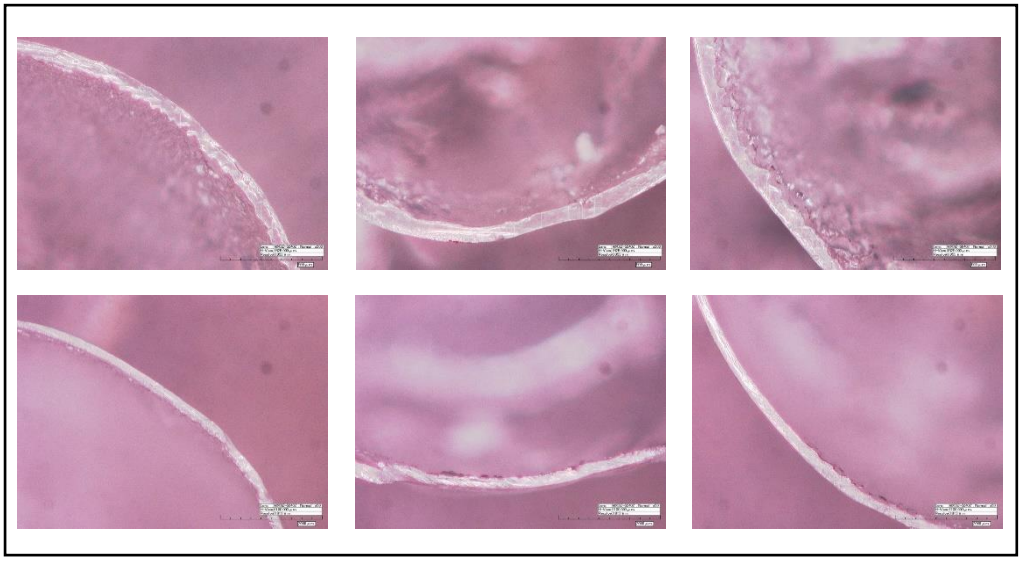

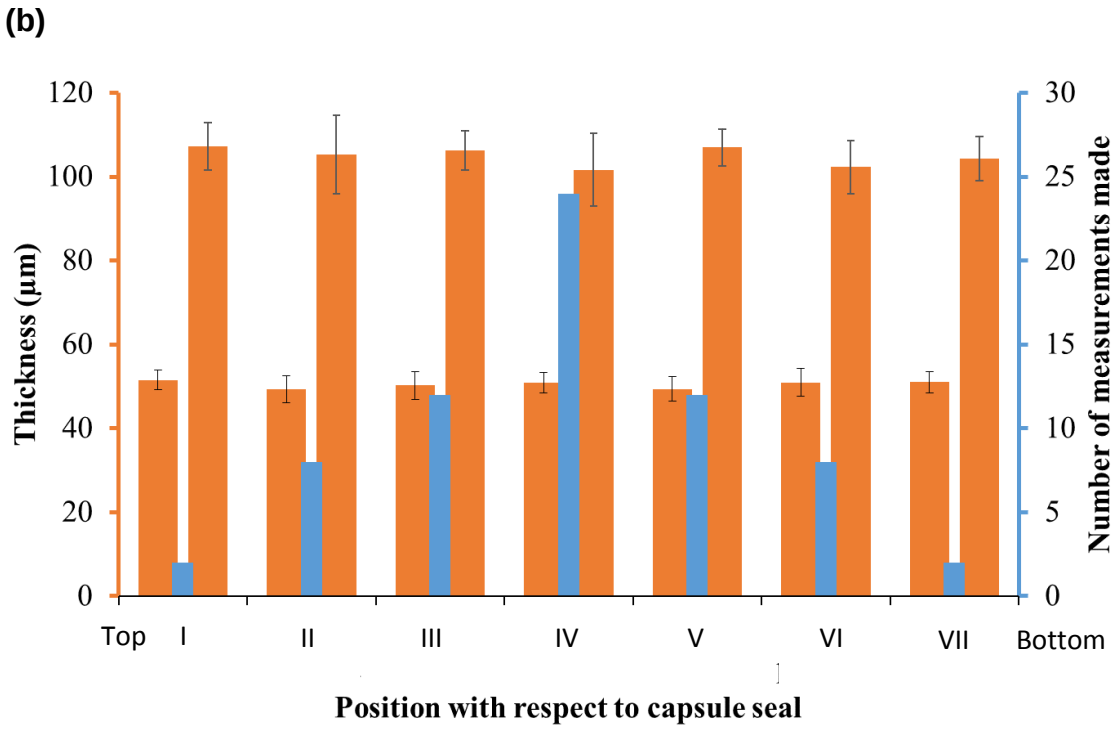

Figure 3.29: (a) Micrographs of shells of thickness 100 µm and 50 µm cryotomed at the equator (Scale: 500 µm). **(b)** Uniformity of shell thickness

3.4.3.2 Hydrostatic pressure determination

Two levels each of thickness, size and hydration levels of PLGA capsules were used to determine the developing hydrostatic pressure in the capsule. Water was pumped into the capsule at a controlled rate by a syringe pump and the hydrostatic pressure was recorded using a pressure gauge.

Figure 3.30 shows a comparison in expansion between

a) capsule with 0.65% w/w moisture content and 0.01% w/w moisture content

b) capsule of radius 1.5 mm and 2.2 mm

c) capsule of shell thickness 50 μm and 100 μm

Even by the ball inflation technique, one can observe, macroscopically, the stages of elastic and plastic deformation, including localized shear deformation or necking.

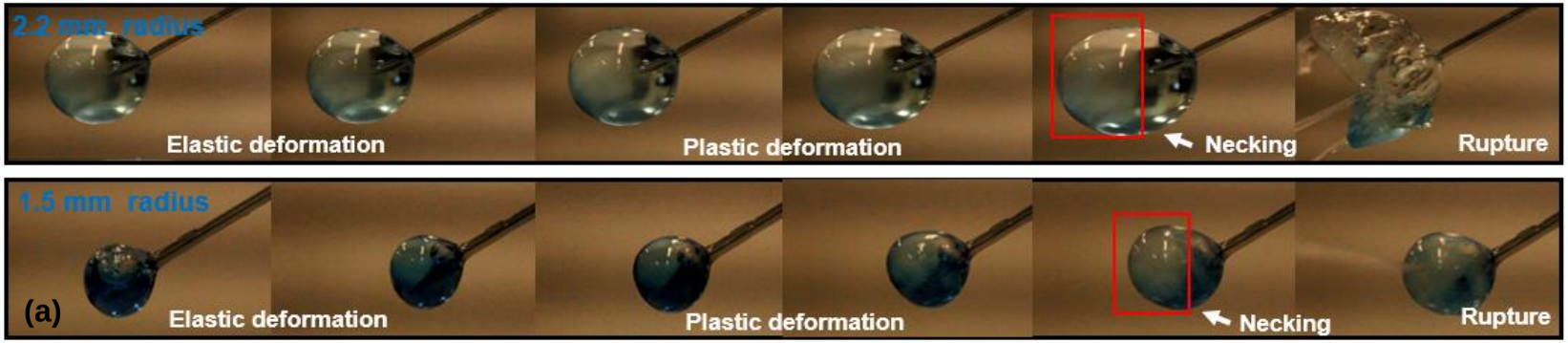

Figure 3.30: (a) Panel comparing various stages of stretch and elastoplastic deformation of capsules of two different radii by the Beach-ball inflation technique

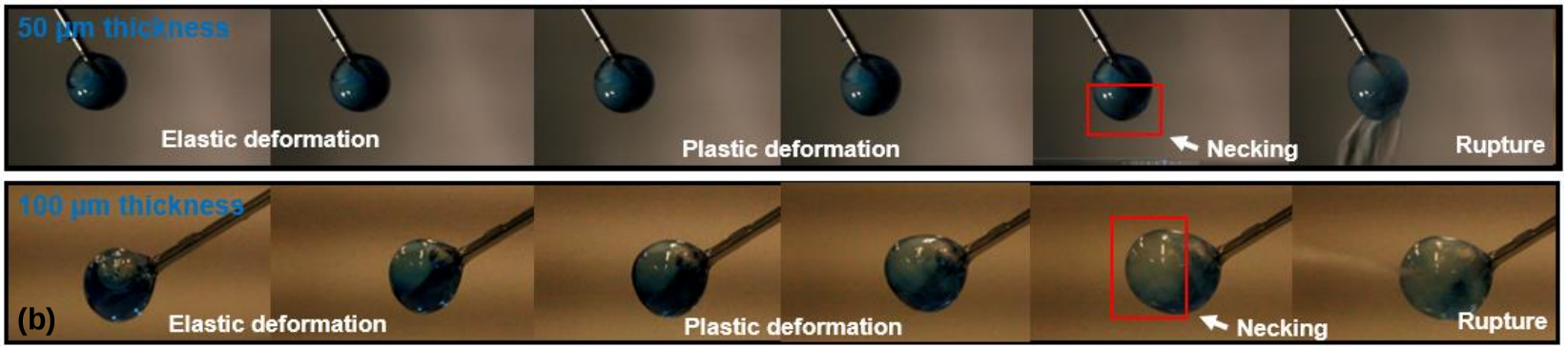

Figure 3.30: (b) Panel comparing various stages of stretch and elastoplastic deformation of capsules of two different wall thickness by the Beach-ball inflation technique

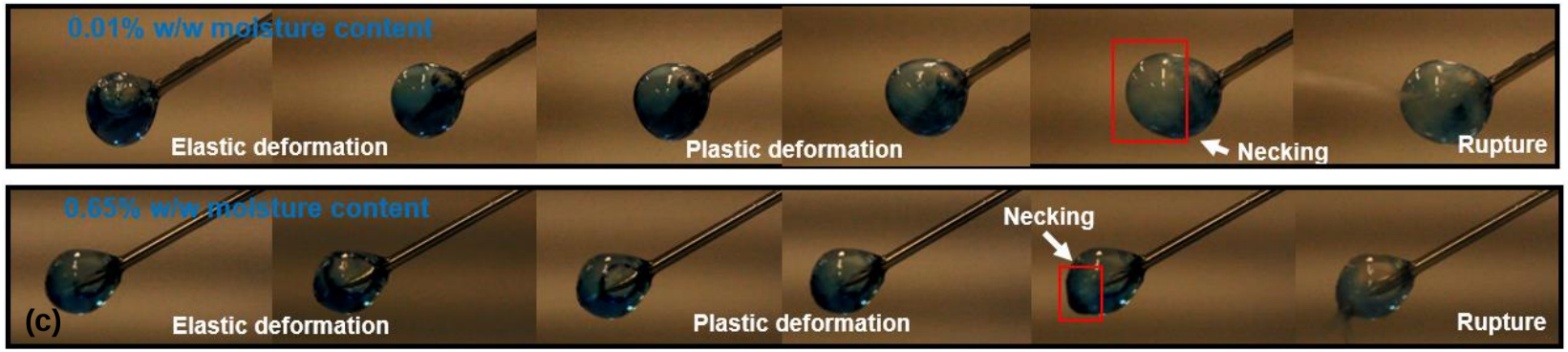

Figure 3.30: (c) Panel comparing various stages of stretch and elastoplastic deformation of capsules at two levels of hydration by the Beach-ball inflation technique

An example raw data of pressure (as recorded by the pressure gauge) vs time is given in Figure 3.31 for a capsule of radius 2.2 mm and wall thickness 50 um.

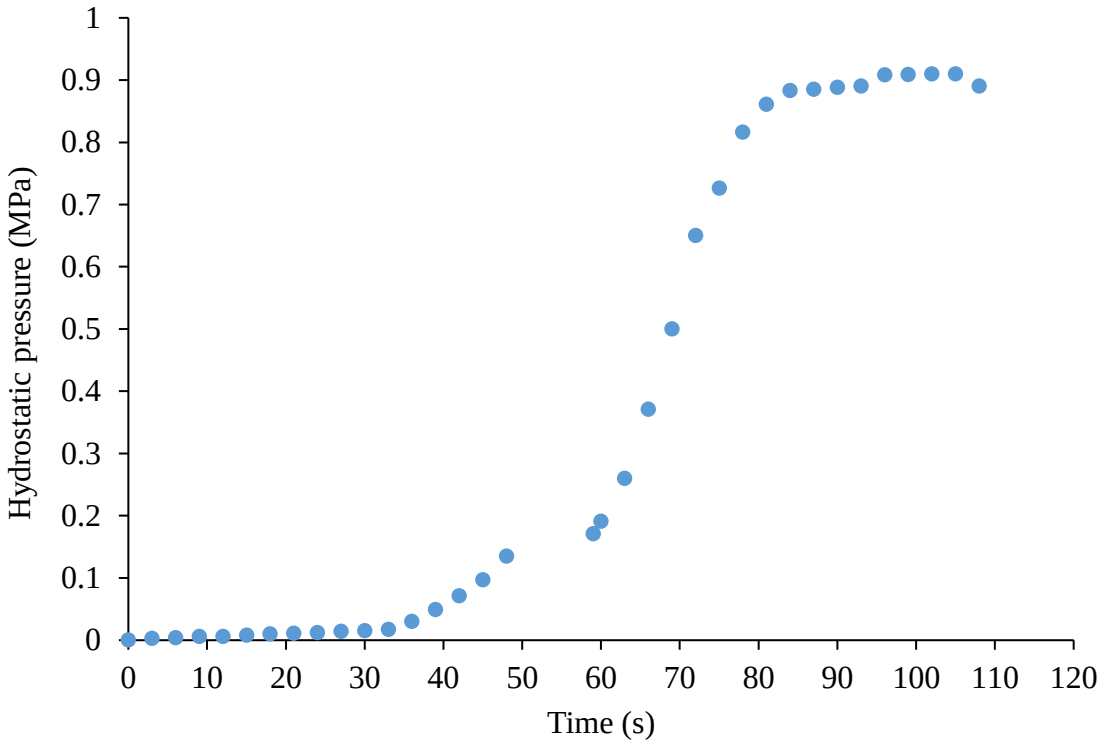

Figure 3.31: Raw data of hydrostatic pressure vs time

The initial slow increase in hydrostatic pressure is a result of entrance of water into the capsule and subsequent compression of air initially present. The contribution of this filling stage to the overall hydrostatic pressure is very small and was not considered in the analysis (Figure 3.32).

(NOTE: When the pressure increased very slowly during the initial stages, the pressure gauge would register that as inactivity and would switch off automatically. It took a few seconds to switch it on again, resulting in break in the hydrostatic pressure versus time curve)

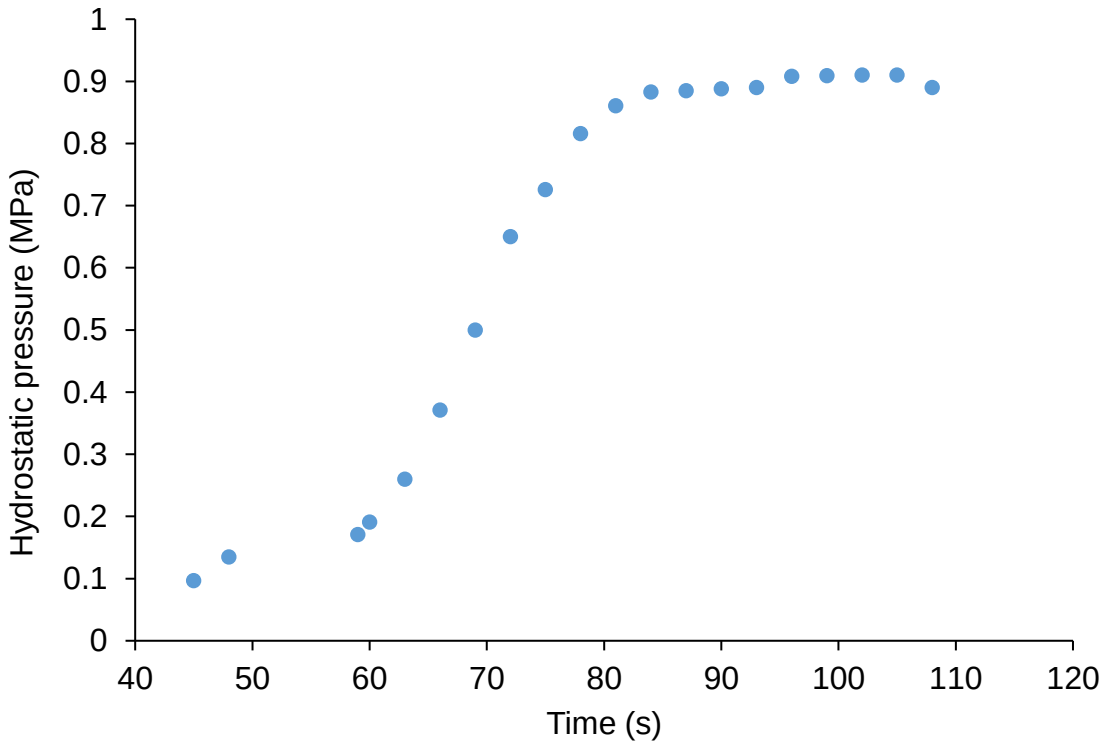

Figure 3.32: Hydrostatic pressure vs time

From the known constant rate of water influx, the volume of water pumped into the capsule at any given time was determined from which the strain was deduced. Then, hydrostatic pressure was plotted against the resultant strain for capsules with two different radii and shell thicknesses at two stages of hydration (Figure 3.33)

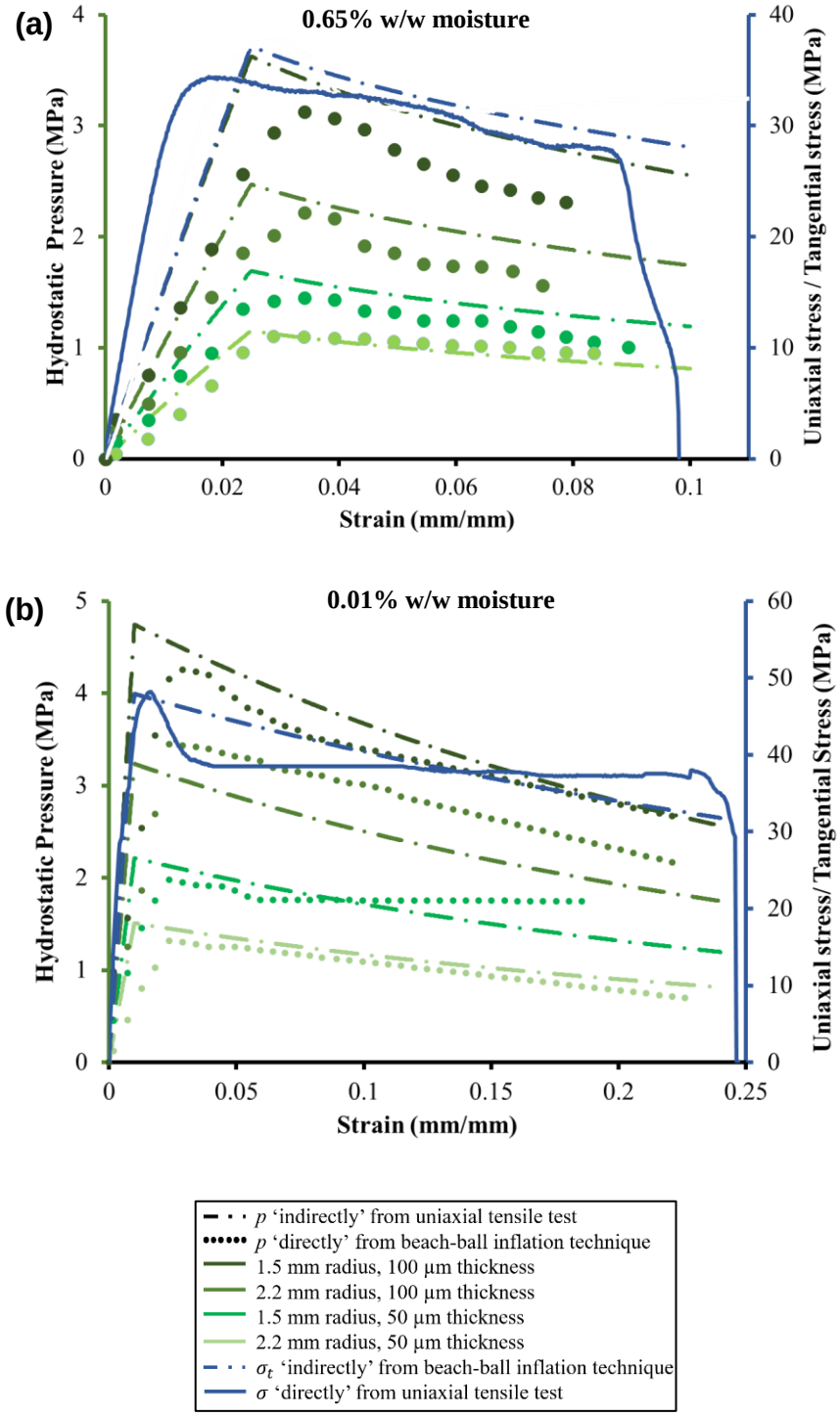

Figure 3.33: Hydrostatic pressure and Tensile stress vs strain for capsules at (a) 0.65% w/w hydration level (b) 0.01% w/w hydration level

In all cases, there is an initial rapid rise in the hydrostatic pressure with strain which corresponds to elastic extension. Once the capsule yields, its volume increases more rapidly than pressure by extension of the capsule at the zone of necking, and conversely the pressure decreases steadily until critical extension is reached. The peak hydrostatic pressure required to yield the shell is greater for a capsule with a thicker shell or a smaller radius. The hydrostatic pressure versus extension trends determined experimentally using the beach ball inflation technique (green dotted curves in Figures 3.33a and b) agree with the trends predicted by the model using the uniaxial tensile test (Eqs. 3.22 and 3.24) (green dashed curves in Figures 3.33a and b).

The tangential stress in the capsule shell was determined from the hydrostatic pressure using Eqs. 3.22 and 3.24 (blue dashed curve in Figures 3.33a and b). This tangential stress corresponds to the uniaxial tensile stress trends determined earlier (blue solid curve in Figures 3.33a and b).

Similar to the uniaxial tensile test, the state of hydration influences the hydrostatic pressure that is generated in the capsule shell as well as the capsule expansion. The capsule extends to a strain of approximately 20% with 0.01% water content whereas it extends to approximately 10% with 0.65% water content. The peak hydrostatic pressure generated is also higher with a dehydrated capsule (e.g. 4.9 MPa for a capsule which is 1.5 mm in radius and 100 μm in thickness) than a hydrated one (e.g. 3.7 MPa for a capsule which is 1.5 mm in radius and 100 μm in thickness).

3.5 Conclusions

In this chapter, elastoplastic and failure characterization of PLGA was conducted as a function of hydration under uniaxial and biaxial stretch, and by a novel "beach ball" inflation technique. The presence of small amounts of moisture in PLGA led to a decrease in the elastic modulus, tensile stress and elongation at break. By the "beach ball' inflation technique we showed, with an initially isotropic PLGA as the capsule shell material, the tangential stress developing in the capsule shell undergoing hydrostatic expansion is the same as the uniaxial tensile stress developing in a rectangular specimen, during both elastic and plastic deformation and at different levels of hydration. Henceforth, the tensile properties determined using the uniaxial tensile test listed in Table 3.3 were used for the model describing capsule rupture (Chapter 4).

4. Time to rupture Determination

4.1 Introduction

A traditional goal of pharmaceutics, namely the development of drug delivery systems with a continuous and/or constant drug release rate, does not apply in all circumstances. For drugs that develop biological tolerance when they are constantly present at the target site, drugs that require specified, timed administration, and hormones and vaccines, pulsed delivery may offer significant advantages over continuous release.[52] "Pulsed drug release" is defined as the one-time, rapid and transient release of a drug after a predetermined dormant period. In this chapter, we study biodegradable, spherical PLGA capsules containing a model dye along with an osmotically active agent (osmogent), which drives influx of water at a controlled rate until the hydrostatic pressure developed overcomes the tensile strength of the PLGA shell resulting in its rupture and instantaneous release of the payload (Figure 4.1). The time to rupture depends on geometry of capsule lumen and shell, and the osmogent concentration.

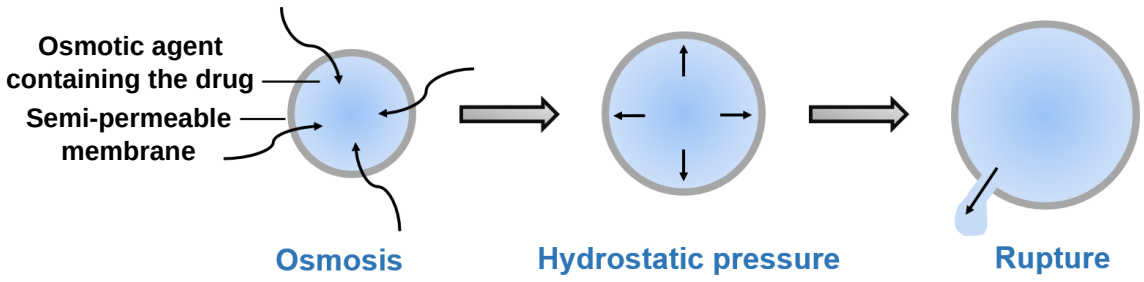

Figure 4.1: Schematic representation of an osmotic bursting device when placed in a biological fluid

In 1991, Kuethe et al. developed a mathematical model to predict the burst time of spherical capsules containing an osmogent after exposure to water.[10] The model, however, was restricted to conditions where a) core osmotic pressure is constant and, b) the membrane follows Hookean behavior. Moreover, for spherical capsules, correlation of in-vitro results to the model has not been presented so far.

Amsden et al. conducted a mechanistic study of the release of osmogents contained in spherical cavities of hydrophobic polymeric monoliths.[11] They developed a mathematical model to predict the time of rupture of a spherical cavity as a function of osmosis which agreed with the in-vitro data. However, the model is restricted to conditions where a) an infinite medium of polymer surrounds the spherical cavity and, b) the polymer is neo-hookean like rubber.

Recently, Melchels et al. demonstrated osmosis-driven delayed burst delivery of vaccines with poly(ε-caprolactone) cylindrical capsules.[12] To correlate the results to a model, however, they used a curve fitting method to correlate the hydrostatic pressure generated at burst to the radius of the capsule and thickness of the membrane. This makes the model very specific to the polymer type and does not provide a mechanistic basis to relate hydrostatic pressure generation with the capsule geometrical parameters.

Objective:

A model is developed to predict the precise time of rupture of spherical capsules as a function of shell thickness, radius of the sphere, core osmotic pressure and membrane elastoplastic tensile properties and the model's correlation with in-vitro results is demonstrated. Membrane elastoplastic properties were determined by uniaxial tensile

testing and the beach-ball inflation technique, as outlined in Chapter 3. For the in-vitro study, two levels each of capsule thickness, radius of the sphere and core osmotic pressure were used.

4.2 The Model

Consider a spherical shell of thickness *h*. Let the inner radius of the shell be *a* and outer radius be *b, so h = (b - a)*. The core contains an osmogent which exerts an osmotic pressure π to draw water from the exterior into the core through the semi-permeable membrane shell by osmosis. Starting with a saturated salt solution in the core without any excess solid osmagent, the osmotic pressure exerted will be maximum in the beginning. As water permeates into the core, the osmogent solution is diluted, resulting in decreasing levels of osmotic pressure, and subsequently, a decreasing rate of water influx. As a consequence of water permeation and stretching of the membrane however, hydrostatic pressure *p* exerted against the inner side of the shell increases, resulting in expansion (Figure 4.2).

(Here and below, we assume, without loss of generality, that the hydrostatic and osmotic pressures outside the capsule are at a reference level, taken to be zero.)

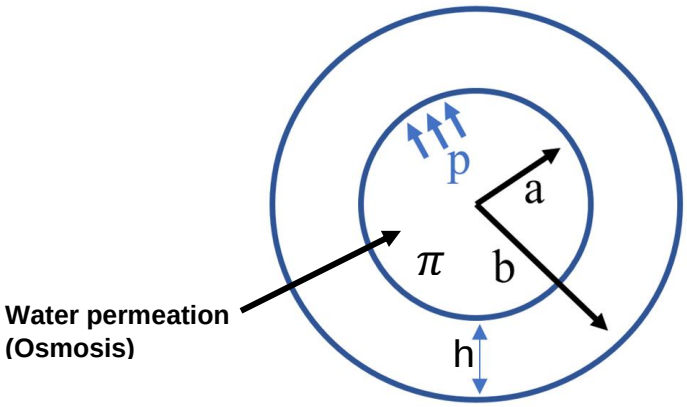

Figure 4.2: A spherical osmotic capsule

When the hydrostatic pressure generated exceeds the tensile strength of the shell, the capsule ruptures and instantaneously releases the payload. Considering that PLGA is an elastoplastic material, the time to yield and time to rupture can be determined as follows.

Water influx due to osmosis is proportional to the difference between the osmotic pressure π and hydrostatic pressure p inside the capsule, the area available for water permeation A, and the PLGA membrane's hydraulic permeability coefficient k, while it is inversely related to the membrane thickness h. Rate of water influx $\frac{dV}{dt}$ into the capsules is, thus, given by

$$\frac{dV}{dt} = \frac{kA}{h}(\pi - p) \tag{4.1}$$

It is sought to relate all the variables involved, volume, membrane thickness, area, osmotic pressure and hydrostatic pressure, to the radius. In order to directly compare the results for spherical, thin shell capsules with different radii, we define the term 'Extension', λ, as the ratio between radius r at any time to the initial radius r_o.

$$\lambda = \lambda(t) = \frac{r(t)}{r_0} = \frac{r}{r_0}$$

All of the geometrical variables are now expressed in terms of λ.

The volume of the capsule is given by

$$V = \frac{4\pi r^3}{3} = \frac{4\pi\lambda^3 r_0^3}{3} \tag{4.2}$$

We assume that the volume of the membrane remains constant upon deformation although its thickness decreases. Thus, equating the initial volume of the membrane with the volume at any given time point, we get

$$4\pi r^2 h = 4\pi r_o^2 h_o$$

where *h* is the thickness at any time and h_o is the initial thickness. Thus, the thickness *h* of the membrane at any given time point is given by

$$h = \frac{r_o^2 t_o}{r^2} = \frac{h_o}{\lambda^2} \tag{4.3}$$

The surface area of the spherical shell available for osmosis is given by

$$A = 4\pi r^2 = 4\pi\lambda^2 r_0^2 \tag{4.4}$$

Hydrostatic pressure as a function of radius and shell thickness in elastic and plastic regimes has been, determined in Section 3.2 (Eqs. 3.22 and 3.24, respectively) as

$$p_{elastic} = \frac{2hE}{r}\left(\frac{r}{r_0} - 1\right)$$

$$p_{plastic} = \frac{2hG}{r}\left(\frac{r}{r_0} - 1\right)^n \text{ H}\left(\frac{r}{r_0} - \frac{r_y}{r_0}\right)$$

where *E* is the Elastic modulus, *G* is the Plastic modulus and *n* is the strain softening component, $\mathrm{H}\left(\frac{r}{r_0}-\frac{r_y}{r_0}\right)$ is the Heaviside function, and r_y is the radius of the capsule when the shell starts to yield. It follows from $r = \lambda r_0$ that

$$p_{elastic} = \frac{2h_0 E}{\lambda^3 r_0}(\lambda - 1) \tag{4.5}$$

$$p_{plastic} = \frac{2h_0 G}{\lambda^3 r_0}(\lambda - 1)^n \mathrm{H}(\lambda - \lambda_y) \tag{4.6}$$

where, λ_y is the critical extension at yield.

According to van't Hoff's law, osmotic pressure π generated by an osmogent solution is given by –

$$\pi = \varphi RTC$$

where φ is osmotic coefficient, or the number of ions produced by dissociation of the osmogent molecule, *R* is the universal gas constant, *T* is the absolute temperature in Kelvin and *C* is the molar concentration of salt. If C_{sat} is the number of moles of the osmogent per unit volume of the saturated solution, then the number of moles of the osmogent *n* in a capsule initially containing saturated solution is given by –

$$n = C_{sat} \times \frac{4}{3}\pi r_0^3$$

$$C = \frac{n}{V} = \frac{C_{sat} \times \frac{4}{3}\pi r_0^3}{\frac{4}{3}\pi r^3} = \frac{C_{sat}}{\lambda^3}$$

Defining $\pi_0 = \varphi RTC_{sat}$, we have

$$\pi = \frac{\pi_0}{\lambda^3} \tag{4.7}$$

Thus, as the capsule expands due to osmosis-driven water influx, that is as λ increases, the osmotic pressure decreases.

We now consider two osmogents, NaCl (MW 58.44 g/mol, C_{sat}= 359 g/L = 6.14 M) and LiCl (MW 42.39 g/mol, C_{sat}= 887 g/L = 20.9 M). Both salts dissociate completely in water, so $\varphi = 2$ in both cases. At 37℃ ,

$RT = \left(8.314\ L.\frac{kPa}{mol.K}\right)(310K) = 2.478\ MPa$. Therefore, we calculate

$\pi_0(NaCl) = 31.7\ MPa$ and $\pi_0(LiCl) = 108\ MPa$

A saturated solution of lithium chloride exerts an osmotic pressure about three times higher than sodium chloride

We now combine all information from previous studies with the theoretical consideration to predict time to yield and time to failure under the elastic and plastic regimes, respectively.

Elastic deformation

Yielding or plastic deformation starts at the end of elastic deformation. Thus, time to yield can be determined by considering only the elastic regime of deformation up to its limit.

Substituting Eqs. 4.2-4.7 Eq. 4.1, we can determine the rate of water influx

$$\frac{dV}{dt} = \frac{4\pi k r_0^2 \lambda}{h_0}\left[\pi_0 - \frac{2h_0 E}{r_0}(\lambda - 1)\right] \tag{4.8}$$

and the rate of capsule extension

$$\frac{d\lambda}{dt} = \frac{k}{h_0 r_0 \lambda}\left[\pi_0 - \frac{2h_0 E}{r_0}(\lambda - 1)\right] \tag{4.9}$$

To determine time to yield t_y, we observe that, at time t = 0, extension $\lambda = 1$

Defining the critical extension to yield, λ_y, and integrate Eq. 4.9 with the result

$$t_y = \frac{h_0 r_0}{k}\int_1^{\lambda_y} \frac{\lambda d\lambda}{\left[\pi_0 - \frac{2h_0 E}{r_0}(\lambda - 1)\right]} \tag{4.10}$$

This can be integrated analytically to give the following solution to the time to yield.

$$t_y = \frac{r_0^3}{2kE^2 h_0}\left\{\ln\left|\frac{\pi_0}{\pi_0 - \frac{2h_0 E}{r_0}(\lambda_y - 1)}\right|\left(\pi_0 + \frac{2h_0 E}{r_0}\right) - \frac{2h_0 E}{r_0}(\lambda_y - 1)\right\}$$

Plastic deformation

Upon yielding, the capsule undergoes plastic deformation before rupture. Thus, time to burst can be determined by considering plastic deformation till rupture.

Substituting Eqs. 4.2-4.7 Eq. 4.1, we determine the rate of water influx

$$\frac{dV}{dt} = \frac{4\pi k r_0^2 \lambda}{h_0}\left[\pi_0 - \frac{2h_0 G}{r_0}(\lambda - 1)^n\right] \mathrm{H}(\lambda - \lambda_y) \tag{4.11}$$

and the rate of capsule extension

$$\frac{d\lambda}{dt} = \frac{k}{h_0 r_0 \lambda}\left[\pi_0 - \frac{2h_0 G}{r_0}(\lambda - 1)^n\right] \mathrm{H}(\lambda - \lambda_y) \tag{4.12}$$

To determine time to burst t_b, we observe that, at time $t = t_y$, extension $\lambda = \lambda_y$

Defining the critical extension to burst, λ_b, and integrate Eq. 4.12 with the result

$$t_b = t_y + \frac{h_0 r_0}{k} \int_{\lambda_y}^{\lambda_b} \frac{\lambda d\lambda}{\left[\pi_0 - \frac{2h_0 G}{r_0}(\lambda - 1)^n\right]} \tag{4.13}$$

In contrast to the elastic portion, there is no general closed form solution for this integral.

Wise Model

The model proposed by Kuethe et al.[2], which assumed a) Constant osmotic pressure and, b) Hookean membrane, determined the time to burst using

$$t_b = \frac{h_0 r_0}{k} \int_{1}^{\lambda_b} \frac{d\lambda}{\lambda^2 \left[\pi_0 - \frac{2h_0 E}{\lambda^3 r_0}(\lambda - 1)\right]} \tag{4.14}$$

4.3. Methods

4.3.1 Osmosis-Driven Delayed Burst Release

For the osmosis-driven delayed burst release test (in-vitro test), the capsule with its stem (as prepared in section 3.2.3) was detached from the syringe needle and placed in a bath containing saturated salt solution, which was then placed in a vacuum chamber. Application of 30 mmHg vacuum allowed degassing of the capsule and releasing the vacuum resulted in a capsule filled with the saturated salt solution. This process was repeated along with sonication until the volume occupied by any air bubble was

significantly less than the total volume of the capsule (that is, less than 5% v/v; this was visually inspected). The capsule stem was cut off and the open end was sealed with a drop of 20% w/v PLGA solution in DCM (Figure 4.3).

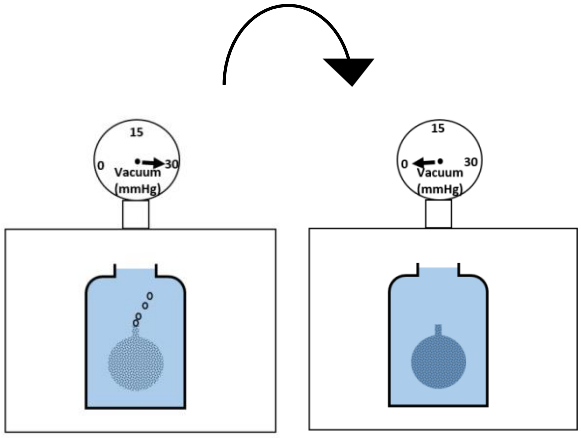

Vacuum filling

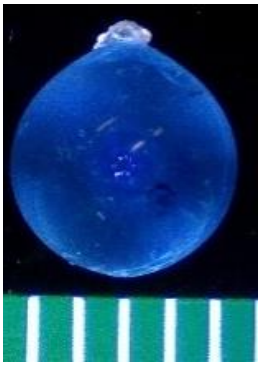

Filled and sealed, finished capsule

Figure 4.3 Capsule preparation for in-vitro release study (mm scale)

Capsules of two thickness levels - 50 µm and 100 µm, two levels of radii – 1.5 mm and 2.2 mm and two levels of core osmotic pressure – 312.51 atm (due to NaCl saturated salt solution) and 1064 atm (due to LiCl saturated salt solution) were placed in PBS at 37℃. A food dye was included with the saturated salt solutions to detect leakage. Mass gain of capsules due to osmosis was recorded at pre-determined time points until rupture (marked by a decrease in mass and discoloration of the capsules). The study was conducted in duplicate for each capsule type.

4.4 Results and Discussion

4.4.1 Model results

When PLGA shell was exposed to water during the capsule filling step, water absorption to an extent of 0.65% w/w occurred. The values of various parameters in the calculations to be presented below were obtained from Table 3.3 (*see* Section 3.4.1.2) for a PLGA film hydrated to an extent of 0.65% w/w. Specifically, we assume $\lambda_y = 1.024$ and $\lambda_b = 1.1$.

4.4.1.1 Rate of water influx

Before determining the relationship between the time to rupture and the geometric variables of the capsule, we gained some insight into the behavior of the expanding capsule by examining the graph between the rate of volume influx and extension as a function of the capsule size, shell thickness and osmotic pressure. As can be anticipated from Eq. 4.1, with increased surface area available for osmosis (that is, larger radius), reduced wall thickness, or greater osmotic pressure generated by lithium chloride solution, the rate of water influx will be higher (Figure 4.4)

(a)

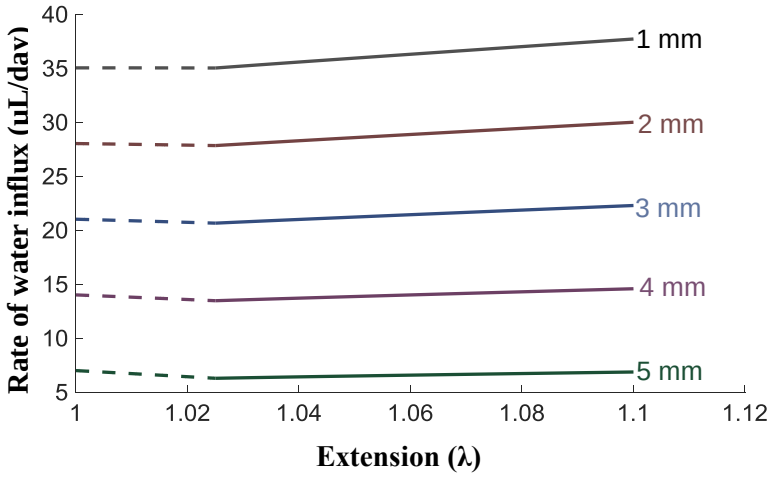

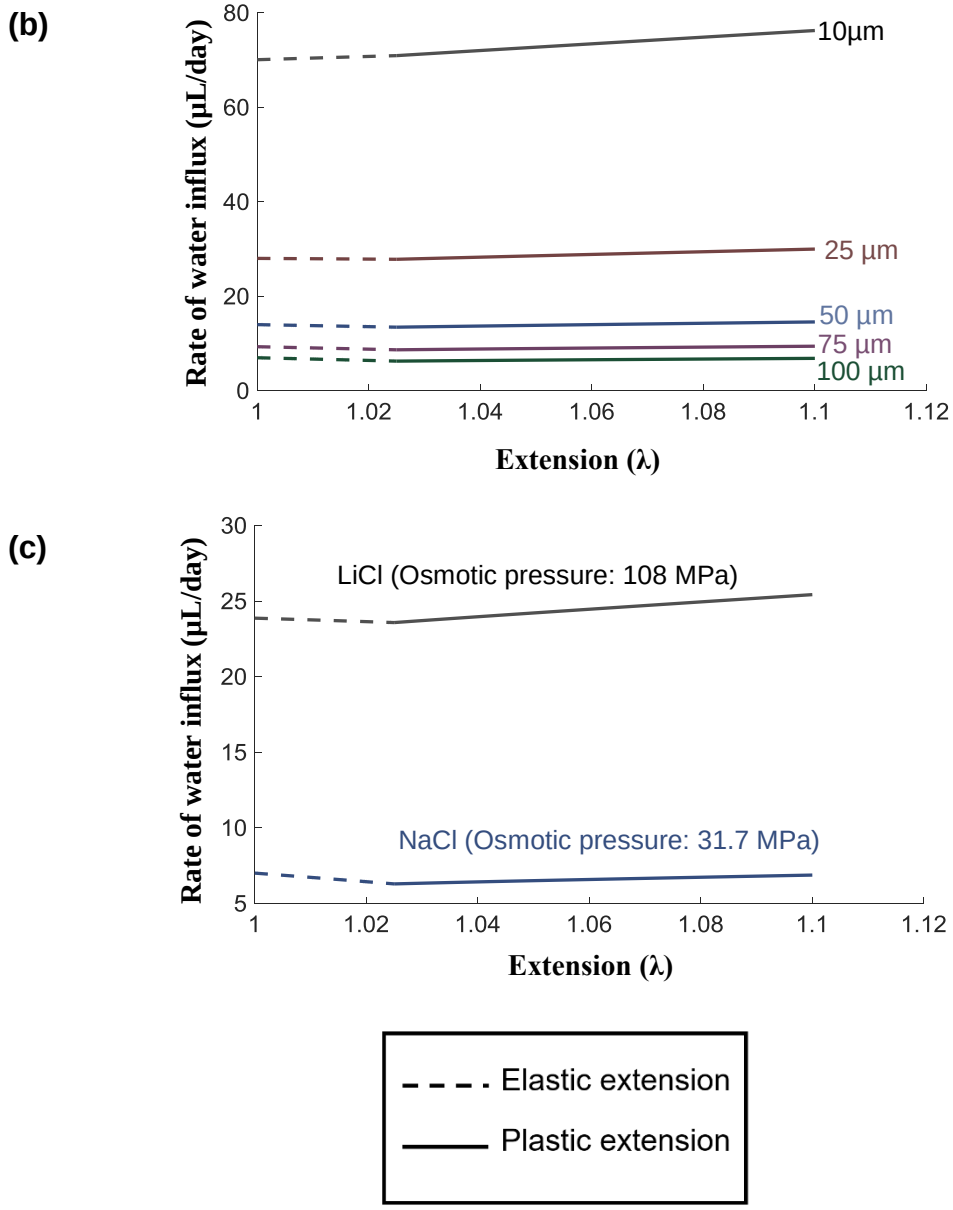

Figure 4.4: Calculated rate of volume influx during elastic and plastic expansion of a spherical capsule as a function (a) capsule radius (Shell thickness: 50 µm, Osmotic agent: NaCl, (b) shell thickness (Capsule radius: 2 mm, Osmotic agent: NaCl) and, (c) core osmotic pressure (Capsule radius: 2 mm, Shell thickness: 50 µm).

Further, with water influx, the osmotic pressure in the capsule core decreases due to dilution of the salt solution. On the other hand, the hydrostatic pressure exerted against the capsule wall simultaneously increases during elastic expansion, which decreases the overall driving force for osmosis. While this should cause a decline in the water influx rate, the surface area available for osmosis increases and the shell thickness decreases with extension which will have an opposite effect.

The hydrostatic pressure generated is directly proportional to the wall thickness and inversely proportional to the capsule radius (Eq. 4.5). Thus, a capsule with a larger radius or thinner shell will exert a smaller hydrostatic pressure against the wall than a capsule with smaller radius and thicker shell (Figure 4.5). In other words, the driving force for osmosis will be greater for the former capsule than the latter at any given extension (Figure 4.6).

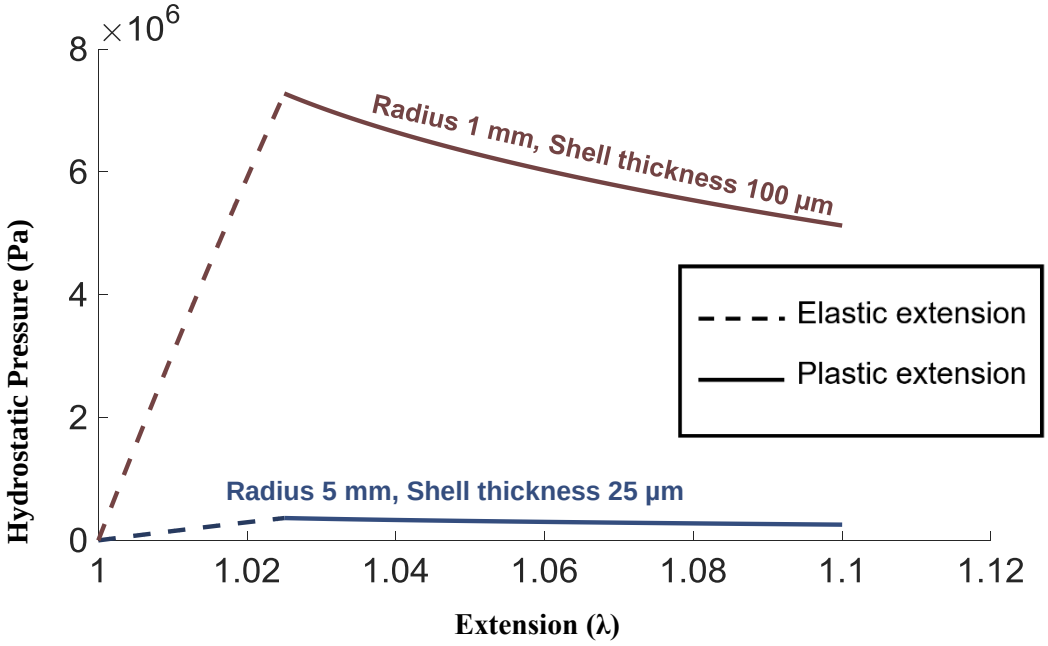

Figure 4.5: The hydrostatic pressure generated is greater for a thin-walled large capsule than a thick-walled small capsule

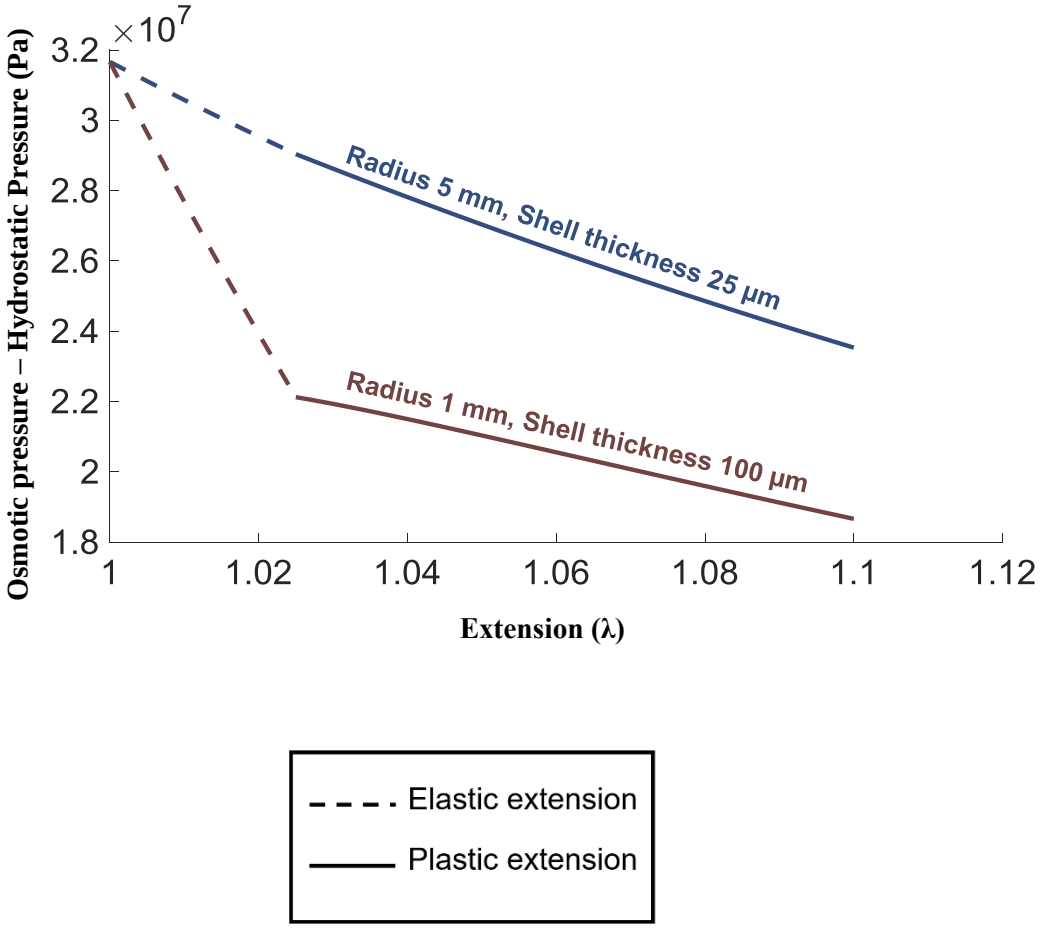

Figure 4.6: The driving force for osmosis that is, the difference between the osmotic and hydrostatic pressures is greater for a thin-walled, larger capsule than a thick-walled, smaller capsule (Osmotic agent: NaCl)

As a consequence of decreasing osmotic pressure and increasing hydrostatic pressure, the overall rate of water influx during the elastic regime decreases with an increase in extension in case of a small and thick-walled capsule, while a greater increase in the surface area and decrease in shell thickness offsets such an effect in case of a large and thin-walled capsule (Figure 4.7).

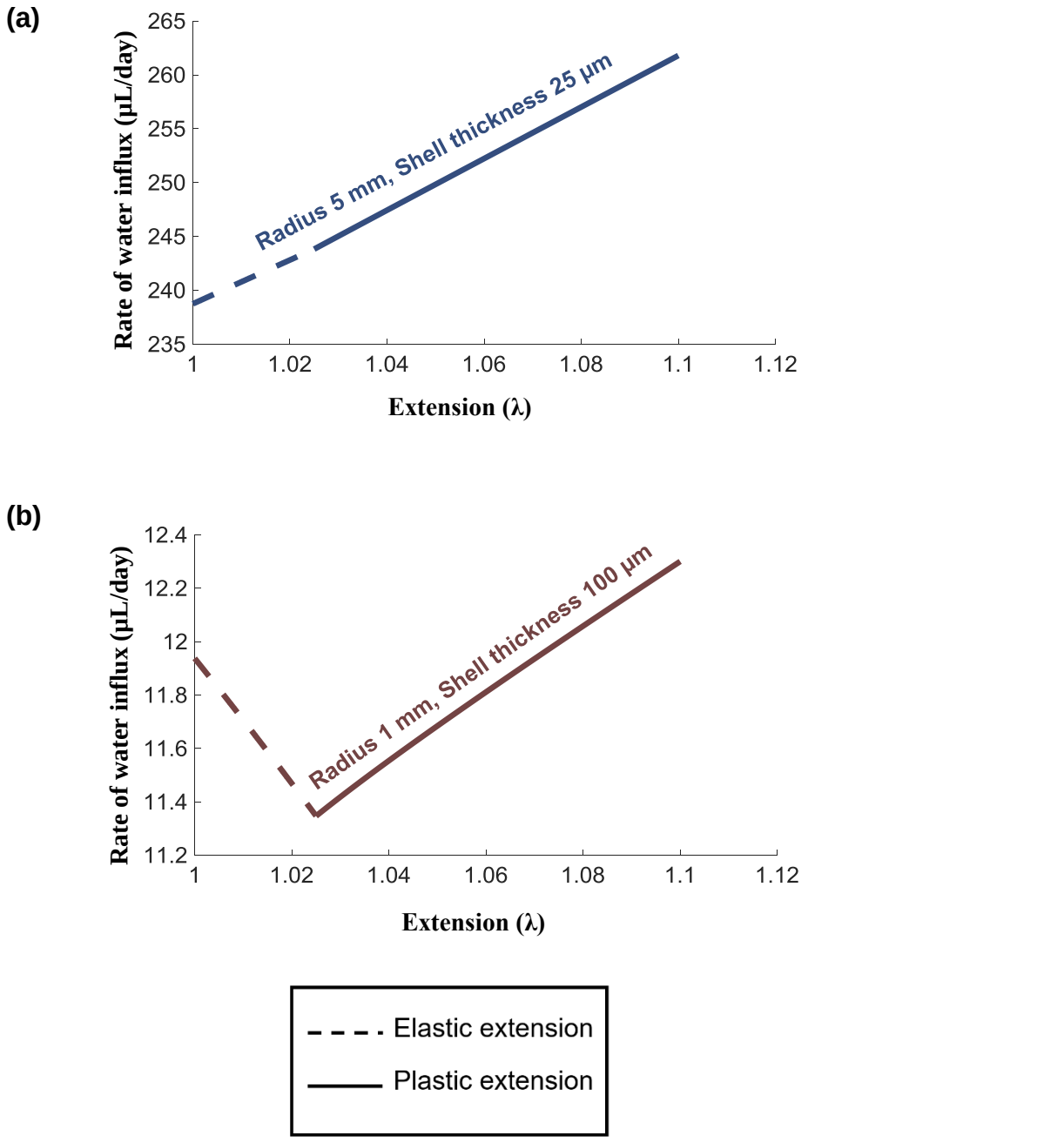

Figure 4.7: The rate of volume influx due to osmosis is greater for **(a)** a thin-walled, larger capsule than **(b)** a thick-walled smaller capsule (Osmotic agent: NaCl)

During plastic expansion, since in this specific case, the strain softening exponent is negative and very close to zero, the hydrostatic slightly declines after yielding (Figure

4.5). This declining function, when subtracted from a decreasing osmotic pressure results in a lower rate of decline in the driving force for capsule expansion during the plastic regime (relative to that during the elastic regime) (Figure 4.6). Coupled to this is the ever-increasing surface area for osmosis and decreasing shell thickness with extension, which ultimately results in an increase in the rate of water influx that rises more rapidly again in case of a larger, thin-walled capsule (Figure 4.7).

4.4.1.2 Time to rupture

Figure 4.8 shows a variation in time to capsule burst as a function of (a) capsule radius, (b) capsule shell thickness and, (c) core osmotic pressure. The time to burst increases with increasing capsule radius and shell thickness and decreasing osmotic pressure.

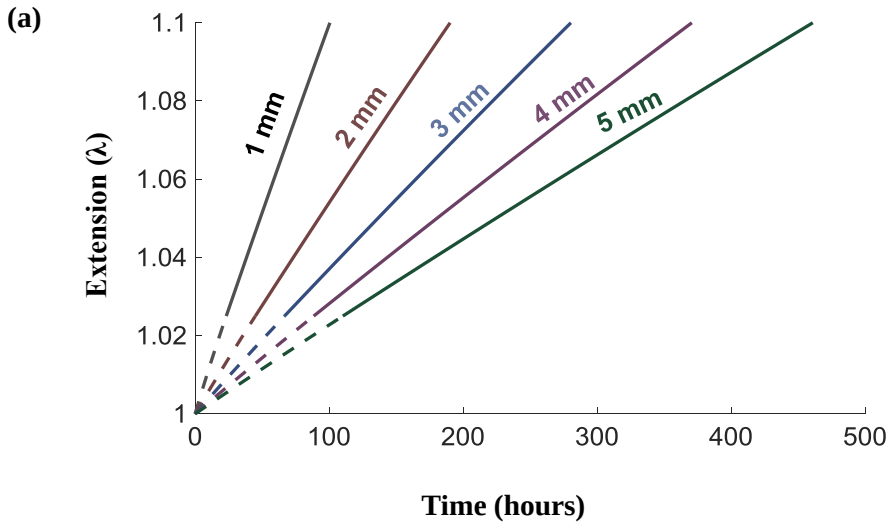

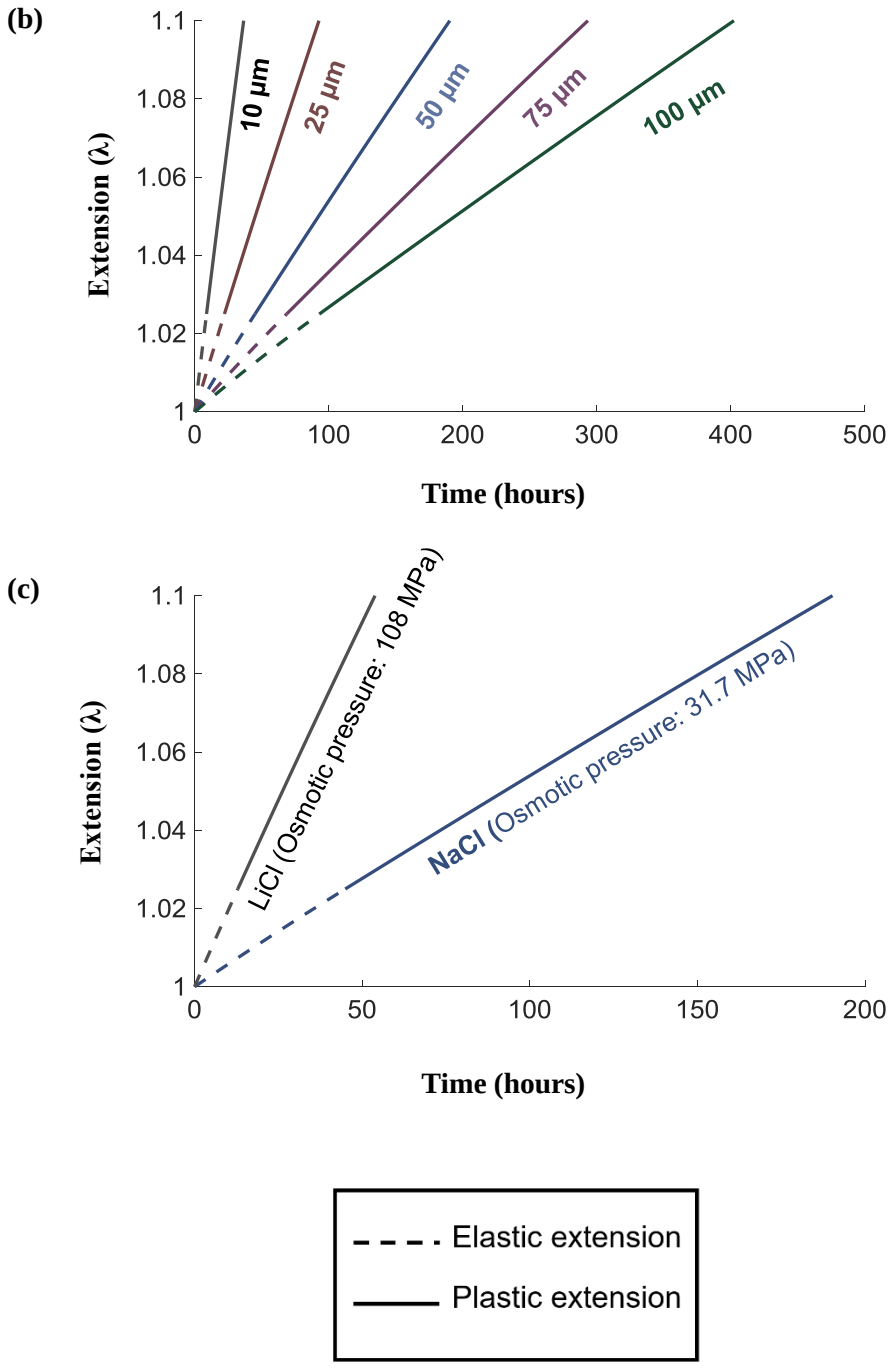

Figure 4.8: Time to burst as a function of **(a)** capsule radius (Shell thickness: 50 µm, Osmotic agent: NaCl), **(b)** shell thickness (Capsule radius: 2mm, Osmotic agent: NaCl) and, **(c)** core osmotic pressure (Capsule radius: 2 mm, Shell thickness: 50 µm)

Discussion

In section 4.4.1.1, an increasing trend in rate of water influx was seen with increasing capsule radius and decreasing shell thickness. Hence, it may seem intuitive that a larger or thin-walled capsules should rupture earlier. While this is true for thin-walled capsules, the larger capsules counter-intuitively burst much later than the smaller ones. This can be explained as follows:

a. For a larger capsule, more water is needed to expand the capsule to a critical extension. Consequently, longer is the time needed to rupture.
b. This is an extension of reason (a). Figure 4.9 shows the trend in the hydrostatic pressure exerted against the capsule wall with time. (Dotted lines indicate the trend in two capsules with same wall thickness but different radii, while the green-colored lines indicate the trend in two capsules with same radii but differing wall thickness). While it is true that the hydrostatic pressure required to cause rupture in the wall of a smaller capsule is greater than that of the larger capsule, that hydrostatic pressure is generated earlier in case of the smaller capsule owing to a smaller volume needed to generate that pressure.

   Moreover, the hydrostatic pressure required to cause rupture in the wall of a thick-walled capsule is greater than that of its thin-walled counterpart, and that hydrostatic pressure is generated earlier in case of the thin-walled capsule because of the faster rate of water influx.

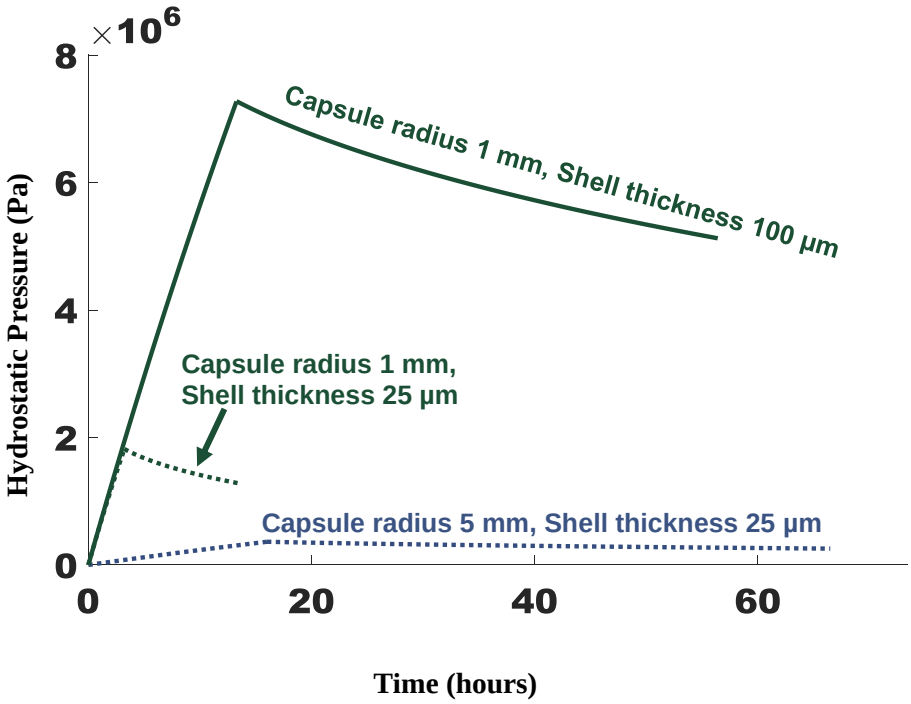

Figure 4.9: Change in hydrostatic pressure with time as a function of capsule radius and shell thickness

4.4.1.3 Comparison with models assuming constant osmotic pressure, Hookean membrane and both

Figure 4.10 shows the time of rupture of a capsule shell of thickness 100 μm and radius 3 mm as predicted by the current model as well as the models that assume constant osmotic pressure or only elastic deformation or both. The current model takes into consideration the variation in osmotic pressure with extension as well as the elastoplastic behavior of the membrane to determine the time of rupture. The model that assumes a constant osmotic pressure estimates a pre-mature time of rupture as it over-predicts the driving force for osmosis that is present at any given time (Figure 4.11b). A model which assumes the membrane to be Hookean will predict a delayed time of rupture as it predicts a larger-than-required hydrostatic pressure to be achieved for a given extension (Figure 4.11a). A model that assumes both would predict a time of rupture intermediate of the former two models with assumptions (Wise Model).[10]

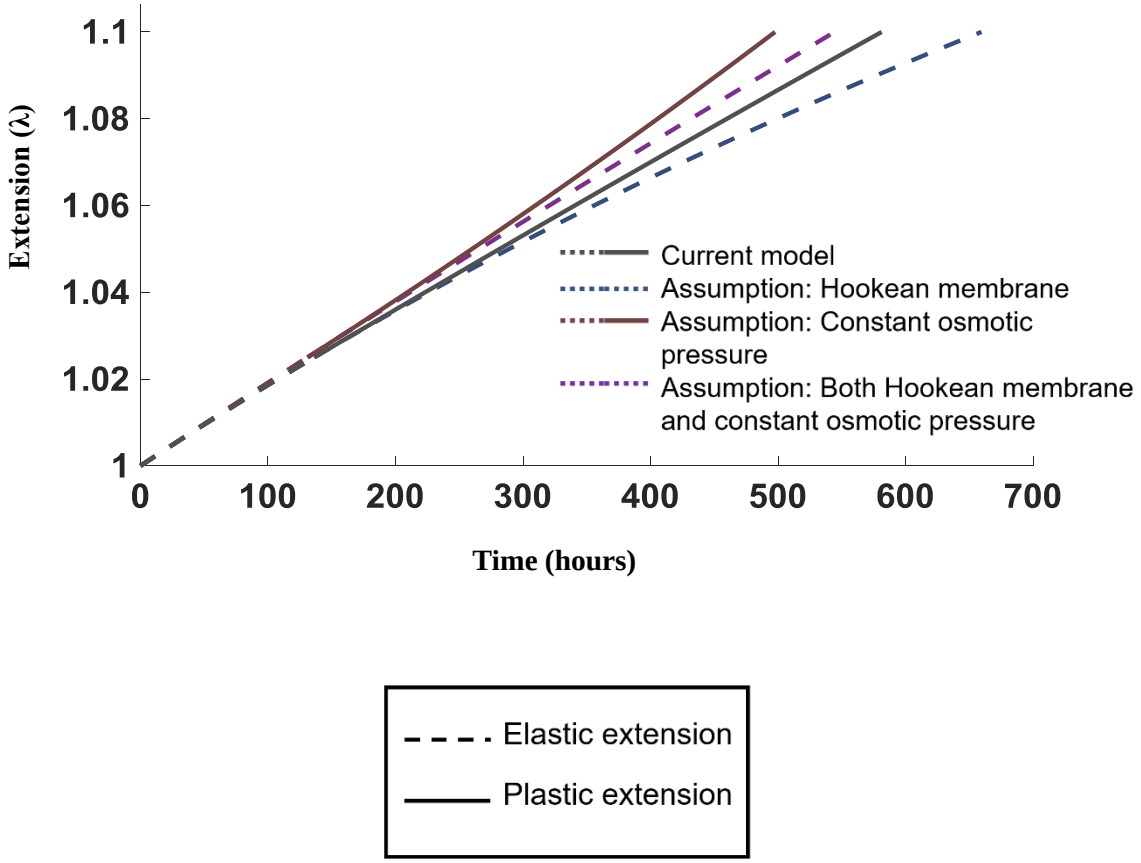

Figure 4.10: Comparison of the current model with models which assume a constant osmotic pressure, a Hookean membrane or both**.**

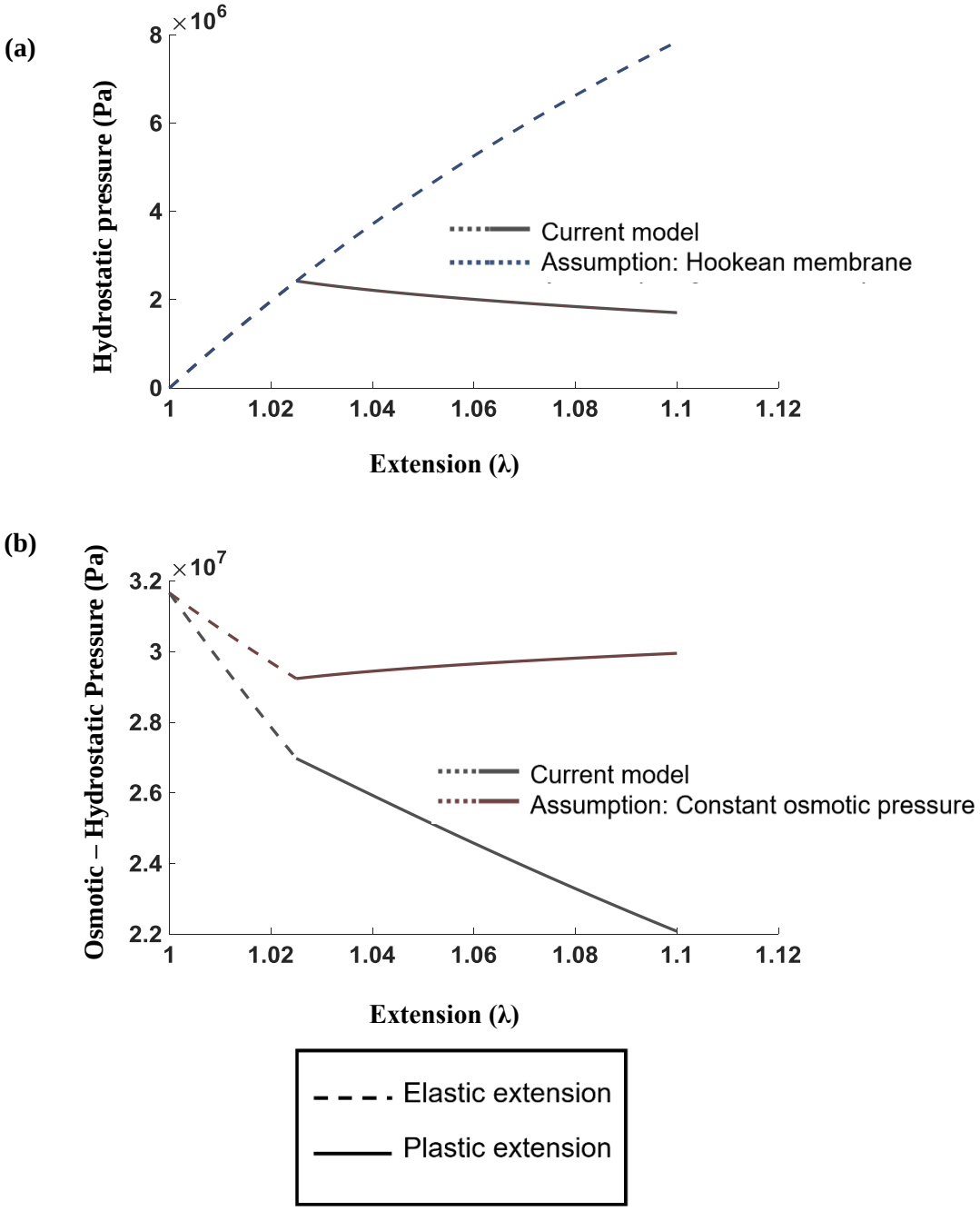

Figure 4.11: (a) Over-prediction of hydrostatic pressure need for shell rupture by a model that assumes a Hookean membrane **(b)** Over-prediction of driving force for osmosis generated within a capsule by a model that assumes constant osmotic pressure

4.4.2 In-vitro Results

Figure 4.12 compares the average extension of capsule shells versus time as determined from the known volume of water uptake (obtained from mass data; density of solution considered to be 1g/cc) during the in-vitro study (scatter-plot) with the model predictions (line plot). It compares capsules at two levels of osmotic pressure (LiCl: Green lines, NaCl: Blue lines), two levels of thicknesses (50 μm: light blue/green color), 100 μm: dark blue/green color) and two levels of radii (1.5 mm: solid line, 2.2 mm: dashed line). The terminal data points, determined experimentally, approximately correspond to the time of burst. Clear difference in the rate of extension with osmotic pressure, capsule radius and shell thickness can be observed which ultimately contributes to the differences in the time to rupture as predicted by the model. The capsule containing sodium chloride solution with a radius of 2.2 mm and shell thickness of 100 μm, however, deviates from the model prediction beyond approximately 250 hours. This may be attributed to significant degradation of PLGA shell, which will influence the permeability and mechanical properties of the PLGA membrane.

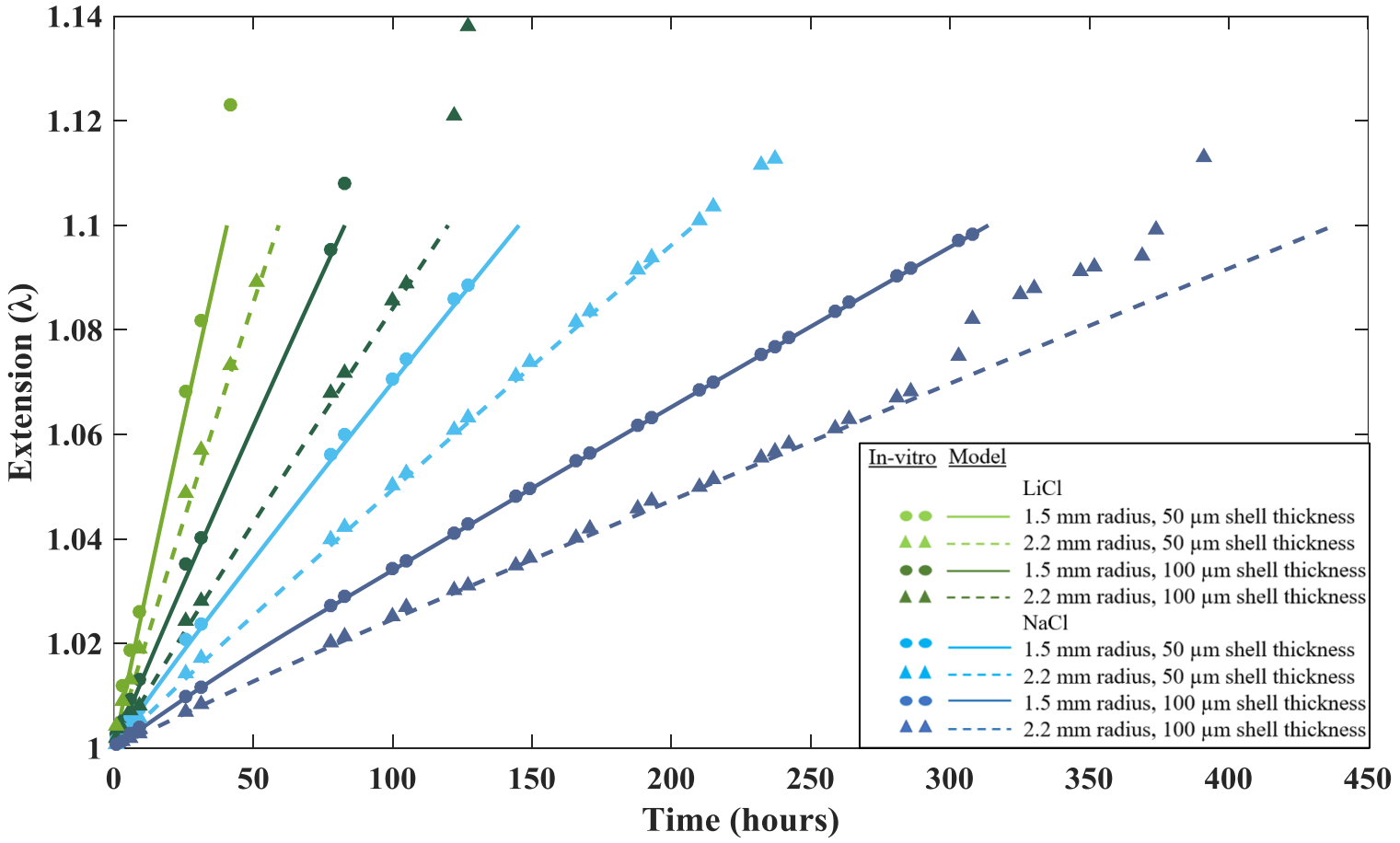

Figure 4.12: In-vitro extension of capsule shell with time compared to the model

Conclusion:

Hydrophobic capsule shells encapsulating hydrophilic liquid cores and vice-versa can be prepared using the technique outlined here. A model was developed to determine the precise time of rupture of these spherical capsules as a function of shell thickness, radius of the sphere, core osmotic pressure and membrane elastoplastic tensile properties and its correlation with in-vitro results was demonstrated. For the in-vitro study, two levels each of capsule thickness, radius of the sphere and core osmotic pressure were utilized. The model allowed determination of the precise time of rupture in-vitro.

5. Conclusions and Future Directions

5.1 Conclusion

In this thesis, we reported preparation of biodegradable poly(lactic acid-co-glycolic acid) (PLGA) capsules in a spherical geometry, which exploit the principle of osmosis as an internal program to achieve delayed-burst release of the payload, elastoplastic and failure characterization of PLGA as a function of hydration, and mathematical modelling to determine the lag time before drug release.

In Chapter 2, hydration and degradation of PLGA and resultant reduction in its glass transition temperature were monitored over time and its water permeability coefficient was determined.

In Chapter 3, elastoplastic and failure characterization of PLGA were conducted as a function of hydration under uniaxial stretch, and by a novel "beach ball" inflation technique. The presence of small amounts of moisture in PLGA led to a decrease in its elastic modulus, tensile stress and elongation at break. A structure-mechanical property relationship for semi-crystalline PLGA was proposed based on the fringed-micelle and microfibrillar models. A mathematical model was developed to predict hydrostatic stress developed in the spherical capsule from uniaxial stress with elastoplastic deformation. Determination of the hydrostatic pressure, either directly from the beach-ball inflation technique, or indirectly from the uniaxial tensile test, served as a prelude to determining the time to yield and rupture of spherical osmotic capsules.

In Chapter 4, the preparation process of hydrophobic, spherical capsule shells encapsulating hydrophilic liquid cores was outlined. A mathematical model was

developed to determine the accurate time of rupture of these spherical capsules as a function of shell thickness, radius of the sphere, core osmotic pressure and membrane elastoplastic tensile properties and its correlation with in-vitro results was demonstrated.

5.2 Future Directions

In this study we showed that, with an initially isotropic PLGA as the capsule shell material, the tangential stress developing in the spherical capsule shell undergoing hydrostatic expansion is the same as uniaxial stress in a rectangular specimen, during both elastic and plastic deformation. However, this may certainly not be the case if the starting material is anisotropic. This may arise if PLGA shells are prepared by melt extrusion and compression, which is a preferred preparation process for pharmaceutical applications to avoid the use of organic solvents (e.g. dichloromethane). In such case, elastic and plastic moduli in different directions of load with respect to the initial orientation of the polymer chains will be different. Thus, a more complicated model will be needed to correlate the tangential stress developing in the spherical shell with the uniaxial tensile test results. Alternatively, the 'beach-ball inflation' technique may be used instead of the uniaxial tensile test to determine the developing hydrostatic pressure within the capsule shell with expansion and those results can be directly inserted in the osmosis equation (Eq. 4.1) to determine the time to capsule burst.

As a proof-of-concept study, we used a simple symmetrical, spherical geometry to determine the time to capsule rupture. However, most pharmaceutical capsules are cylindrical or ellipsoidal as there are well established preparation techniques for these

geometries.[53] Thus, a greater potential will exist if this model is extended to a cylindrical geometry.

The study here was restricted to 'thin' shells (where the shell is 20 times thinner than the capsule radius). An elastoplastic model developed for a thick shell, which takes into consideration the progressive yielding of the capsule shell, starting from the inner side of the shell and moving to the exterior, will provide a more comprehensive picture of elastoplastic capsule shells.

Finally, pulsatile drug delivery can be achieved by using a multitude of these osmotic capsules consolidated in a single system, each programmed to release the drug payload after a pre-determined time lag. One of the first in-vivo studies conducted in rabbits used a similar system with a carbon dioxide generating core enclosed by 75/25 PLGA to deliver follicle stimulating hormones.[53] While this study was promising in that the dependence of capsule burst times on membrane thickness and core composition was shown, these relationships were only empirically determined and a mechanistic understanding of the process or pre-determination of burst times was not demonstrated. Thus, further study on this subject should entail determination of in-vivo release profiles of these pulsatile drug delivery systems after pre-determination of lag times for treating disease states which show symptoms' exacerbation at a certain time during the day, for delivering hormones to mimic their natural circadian expression, to deliver drugs that develop biological tolerance upon continuous administration etc.

6. Bibliography

1. Bussemer, T., Otto, I., & Bodmeier, R. (2001). Pulsatile drug-delivery systems. *Critical Reviews™ in Therapeutic Drug Carrier Systems*, *18*(5).

2. Chang, R. K., Guo, X., Burside, B. A., Couch, R. A., & Rudnic, E. M. (1999). Formulation approaches for oral pulsatile drug delivery. *Amer Pharma Rev*, *2*(1), 51-57.

3. Dethlefsen, U., & Repges, R. (1985). Ein neues therapieprinzip bei nachtlichen asthma. *Med Klin*, *80*(1), 44-47.

4. Akiti, O., Jimoh, A. G., Wise, D. L., Barabino, G. A., Trantolo, D. J., & Gresser, J. D. (1996). Multiphasic or "Pulsatile" Controlled Release System for the Delivery of Vaccines. In *Human Biomaterials Applications* (pp. 319-343). Humana Press.

5. Kim, U. R., Peterfreund, R. A., & Lovich, M. A. (2017). Drug Infusion Systems: Technologies, Performance, and Pitfalls. *Anesthesia & Analgesia*, *124*(5), 1493-1505.

6. Poli, S., Busetti, C., & Moro, L. Oral pharmaceutical compositions for specific colon delivery. 1993. *EP 0*, *572*, 942.

7. Krögel, I., & Bodmeier, R. (1999). Floating or pulsatile drug delivery systems based on coated effervescent cores. *International Journal of Pharmaceutics*, *187*(2), 175-184.

8. Huang, X., & Brazel, C. S. (2001). On the importance and mechanisms of burst release in matrix-controlled drug delivery systems. *Journal of controlled release*, *73*(2), 121-136.

9. Youan, B. B. C. (Ed.). (2009). *Chronopharmaceutics: science and technology for biological rhythm guided therapy and prevention of diseases*. John Wiley & Sons.

10. Kuethe, D. O., Augenstein, D. C., Gresser, J. D., & Wise, D. L. (1992). Design of capsules that burst at predetermined times by dialysis. *Journal of Controlled Release,18*(2), 159-164.

11. Amsden, B. G., Cheng, Y. L., & Goosen, M. F. (1994). A mechanistic study of the release of osmotic agents from polymeric monoliths. *Journal of controlled release, 30*(1), 45-56.

12. Melchels, F. P., Fehr, I., Reitz, A. S., Dunker, U., Beagley, K. W., Dargaville, T. R., & Hutmacher, D. W. (2015). Initial design and physical characterization of a polymeric device for osmosis-driven delayed burst delivery of vaccines. *Biotechnology and Bioengineering,112*(9), 1927-1935.

13. Gentile, P., Chiono, V., Carmagnola, I., & Hatton, P. (2014). An Overview of Poly(lactic-co-glycolic) Acid (PLGA)-Based Biomaterials for Bone Tissue Engineering. *International Journal of Molecular Sciences,15*(3), 3640-3659.

14. Tamber, H., Johansen, P., Merkle, H., & Gander, B. (2005). Formulation aspects of biodegradable polymeric microspheres for antigen delivery. *Advanced Drug Delivery Reviews,57*(3), 357-376.

15. Makadia, H. K., & Siegel, S. J. (2011). Poly Lactic-co-Glycolic Acid (PLGA) as Biodegradable Controlled Drug Delivery Carrier. *Polymers,3*(4), 1377-1397.

16. Blasi, P., Dsouza, S. S., Selmin, F., & Deluca, P. P. (2005). Plasticizing effect of water on poly(lactide-co-glycolide). *Journal of Controlled Release,108*(1), 1-9.

17. Dorati, R., & Deluca, P. P. (2014). Effect of Hydration on Physicochemical Properties of End-Capped PLGA. *Advances in Biomaterials,2014*, 1-9.

18. Kranz, H., Ubrich, N., Maincent, P., & Bodmeier, R. (2000). Physicomechanical properties of biodegradable poly(D,L-lactide) and poly(D,L-lactide-co-glycolide) films in the dry and wet states. *Journal of Pharmaceutical Sciences,89*(12), 1558-1566.

19. Zong, X., Wang, Z., Hsiao, B. S., Chu, B., Zhou, J. J., Jamiolkowski, D. D., Dormier, E. (1999). Structure and Morphology Changes in Absorbable Poly(glycolide) and Poly(glycolide-co-lactide) during in Vitro Degradation. *Macromolecules,32*(24), 8107-8114.

20. Gordon, M., & Taylor, J. S. (1952). Ideal copolymers and the second-order transitions of synthetic rubbers. i. non-crystalline copolymers. *Journal of Applied Chemistry,2*(9), 493-500.

21. Houchin, M. L., & Topp, E. M. (2009). Physical properties of PLGA films during polymer degradation. *Journal of Applied Polymer Science,114*(5), 2848-2854.

22. Cohen, M. H., & Turnbull, D. (1959). Molecular Transport in Liquids and Glasses. *The Journal of Chemical Physics,31*(5), 1164-1169.

23. Ayerst, G. (1965). Determination of the water activity of some hygroscopic food materials by a dew-point method. *Journal of the Science of Food and Agriculture*, *16*(2), 71-78.

24. R. C. Weast, *CRC Handbook of Chemistry and Physics* 60th Edition, CRC Press, Boca Raton, FL (1980) 154-199

25. Frisch, H. L. (1957). The time lag in diffusion. *The Journal of Physical Chemistry*, *61*(1), 93-95.

26. Tsuji, H., Mizuno, A., & Ikada, Y. (2000). Properties and morphology of poly(L-lactide). III. Effects of initial crystallinity on long-term in-vitro hydrolysis of high molecular weight poly(L-lactide) film in phosphate-buffered solution. *Journal of Applied Polymer Science,77*(7), 1452-1464.

27. Hill, R. (1971). *The Mathematical Theory of Plasticity*. Clarendon Press, Oxford.

28. Landau, L. D., Kosevich, A. M., Pitaevskii, L. P., & Lifshitz, E. M. (1986). Theory of elasticity.

29. A. J. Nolte, Ph.D. Thesis, Massachusetts Institute of Technology, 2007.

30. Thomson, R. C., Giordano, G. G., Collier, J. H., Ishaug, S. L., Mikos, A. G., Lahiri-Munir, D., & Garcia, C. A. (1997). Manufacture and Characterization of Poly(Alpa-Hydroxy Ester) Thin Films as Temporary Substrates for Retinal Pigment Epithelium Cells. *Retina,17*(5), 471.

31. Barrett, C., & Cameron, R. (2014). Nanoindentation analysis of αtricalcium phosphate-poly(lactide-co-glycolide) nanocomposite degradation. *Materials Science and Engineering: C,42*, 587-594.

32. ASTM D882-02, Standard Test Method for Tensile Properties of Thin Plastic Sheeting, ASTM International, West Conshohocken, PA, 2002

33. Seguela, R. (2005). Critical review of the molecular topology of semicrystalline polymers: The origin and assessment of intercrystalline tie molecules and chain entanglements. *Journal of Polymer Science Part B: Polymer Physics*, *43*(14), 1729-1748.

34. Humbert, S., Lame, O., & Vigier, G. (2009). Polyethylene yielding behaviour: What is behind the correlation between yield stress and crystallinity?. *Polymer*, *50*(15), 3755-3761.

35. Oleinik, E. F., Rudnev, S. N., & Salamatina, O. B. (2007). Evolution in concepts concerning the mechanism of plasticity in solid polymers after the 1950s. *Polymer Science Series A*, *49*(12), 1302-1327.

36. Herrmann, K., Gerngross, O., Abitz, C. (1930). The elasticity of rubber. *Kolloid-Z.* 60, 276

37. Flory, P. J. (1978). Molecular morphology in semicrystalline polymers. *Nature*, *272*, 226-229.

38. Peterlin, A. (1980). Chain folding in lamellar crystals. *Macromolecules*, *13*(4), 777-782.

39. Peterlin, A. (1965, January). Crystalline character in polymers. In *Journal of Polymer Science: Polymer Symposia* (Vol. 9, No. 1, pp. 61-89). Wiley Subscription Services, Inc., A Wiley Company.

40. Peterlin, A. (1975). Plastic deformation of polymers with fibrous structure. *Colloid & Polymer Science*, *253*(10), 809-823.

41. Keith, H. D., & Fadden, F. J. (1959). Deformation mechanisms in crystalline polymers. *Journal of polymer science*, *41*(138), 525-528.

42. Thomas, C., Seguela, R., Detrez, F., Miri, V., & Vanmansart, C. (2009). Plastic deformation of spherulitic semi-crystalline polymers: An in situ AFM study of polybutene under tensile drawing. *Polymer*, *50*(15), 3714-3723.

43. Hoy, R. S., & Robbins, M. O. (2006). Strain hardening of polymer glasses: effect of entanglement density, temperature, and rate. *Journal of Polymer Science Part B: Polymer Physics*, *44*(24), 3487-3500.

44. Hoy, R. S., & Robbins, M. O. (2008). Strain hardening of polymer glasses: Entanglements, energetics, and plasticity. *Physical Review E*, *77*(3), 031801.

45. Men, Y., Rieger, J., & Strobl, G. (2003). Role of the entangled amorphous network in tensile deformation of semicrystalline polymers. *Physical review letters*, *91*(9), 095502.

46. Makke, A., Lame, O., Perez, M., & Barrat, J. L. (2012). Influence of Tie and loop molecules on the mechanical properties of lamellar block copolymers. *Macromolecules*, *45*(20), 8445-8452.

47. Hiss, R., et al. "Network stretching, slip processes, and fragmentation of crystallites during uniaxial drawing of polyethylene and related copolymers. A comparative study." *Macromolecules* 32.13 (1999): 4390-4403.

48. Van Melick, H. G. H., Govaert, L. E., & Meijer, H. E. H. (2003). Localisation phenomena in glassy polymers: influence of thermal and mechanical history. *Polymer*, *44*(12), 3579-3591.

49. Arruda, E. M., & Boyce, M. C. (1993). Evolution of plastic anisotropy in amorphous polymers during finite straining. *International Journal of Plasticity*, *9*(6), 697-720.

50. Chu, C. C. (1981). Hydrolytic degradation of polyglycolic acid: tensile strength and crystallinity study. *Journal of Applied Polymer Science*, *26*(5), 1727-1734.

51. Galliot, C., & Luchsinger, R. H. (2011). Uniaxial and biaxial mechanical properties of ETFE foils. *Polymer testing*, *30*(4), 356-365.

52. Pandit, V., Kumar, A., Ashawat, M., Verma, C., & Kumar, P. (2016). Recent Advancement and Technological Aspects of Pulsatile Drug Delivery System - A Laconic Review. *Current Drug Targets,17*(999), 1-1.

53. Jimoh, A. G., Wise, D. L., Gresser, J. D., & Trantolo, D. J. (1995). Pulsed FSH release from an implantable capsule system. *Journal of controlled release*, *34*(2), 87-95.